

THE UNIVERSITY OF CHICAGO

CHARACTERIZING THE ROLE OF FORMYL PEPTIDE RECEPTORS DURING  
PLAGUE INFECTION

A DISSERTATION SUBMITTED TO  
THE FACULTY OF THE DIVISION OF THE BIOLOGICAL SCIENCES  
AND THE PRITZKER SCHOOL OF MEDICINE  
IN CANDIDACY FOR THE DEGREE OF  
DOCTOR OF PHILOSOPHY

COMMITTEE ON MICROBIOLOGY

BY

BLAKE SANDERS

CHICAGO, ILLINOIS

DECEMBER 2022

## TABLE OF CONTENTS

LIST OF FIGURES.....	iv
LIST OF TABLES.....	vi
ACKNOWLEDGEMENTS.....	vii
ABSTRACT.....	viii
INTRODUCTION.....	1
MATERIALS AND METHODS.....	14
CHAPTER 1: Generating FPR Knockout Mice.....	33
Abstract.....	33
Introduction.....	33
Results.....	34
Discussion.....	38
CHAPTER 2: <i>In vivo</i> bacterial pathogenesis studies.....	41
Abstract.....	41
Introduction.....	41
Results.....	43
Discussion.....	50
CHAPTER 3: Characterizing FPR activation by <i>Yersinia pestis</i> .....	59
Abstract.....	59
Introduction.....	59
Results.....	60
Discussion.....	65
CONCLUSIONS.....	70

<b>REFERENCES.....</b>	<b>71</b>
<b>TABLES.....</b>	<b>83</b>
<b>FIGURES.....</b>	<b>86</b>

## LIST OF FIGURES

Figure 1.1: FPR knockout embryo mutagenesis and breeding scheme.....	86
Figure 1.2: FPR knockout mouse genotyping.....	88
Figure 1.3: Fpr2 <sup>-/-</sup> sequencing alignment for Fpr2 <sup>-/-</sup> mouse line derived from founder 323.....	89
Figure 1.4: Fpr3 <sup>-/-</sup> sequencing alignment for Fpr3 <sup>-/-</sup> mouse line derived from founder 327.....	91
Figure 1.5: Fpr3 <sup>-/-</sup> sequencing alignment for Fpr3 <sup>-/-</sup> mouse line derived from founder 328.....	92
Figure 1.6: Fpr2 <sup>-/-</sup> sequencing alignment for Fpr1/23 <sup>-/-</sup> mouse line derived from founder 327.....	93
Figure 1.7: Fpr3 <sup>-/-</sup> sequencing alignment for Fpr1/2/3 <sup>-/-</sup> mouse line derived from founder 327.....	94
Figure 1.8: PCR genotyping for the Fpr2 <sup>-/-</sup> mouse line derived from founder 329.....	95
Figure 1.9: PCR genotyping for the Fpr1/3 <sup>-/-</sup> mouse line derived from founder 324.....	96
Figure 1.10: Sequencing alignment for the Fpr3 gene in Fpr1 <sup>-/-</sup> mice.....	97
Figure 1.11: Immune cell counts at homeostasis.....	99
Figure 1.12: Mouse weight comparison.....	100
Figure 2.1: Loss of FPRs alters survival kinetics during <i>Y. pestis</i> infection.....	101
Figure 2.2: Loss of FPRs alters bubonic plague dissemination rate.....	102

<b>Figure 2.3: FPR KO mice retain robust neutrophil migratory capabilities</b>	
<i>in vivo</i> .....	103
<b>Figure 2.4: <i>In vitro</i>, <i>ex vivo</i>, and <i>in vivo</i> T3SS injection of host cells.....</b>	<b>104</b>
<b>Figure 2.5: FPRs respond to <i>S. aureus</i> but do not impact organ infiltration.....</b>	<b>105</b>
<b>Figure 2.6: <i>S. aureus</i> WU1 stably colonizes Fpr1/2/3<sup>-/-</sup> mice.....</b>	<b>106</b>
<b>Figure 3.1: <i>Y. pestis</i> supernatant activates Fpr1 in FPR reporter assays.....</b>	<b>107</b>
<b>Figure 3.2: <i>S. aureus</i> supernatant activates hFPR1 and hFPR2.....</b>	<b>108</b>
<b>Figure 3.3: <i>Y. pestis</i> supernatant activates FPR1 in neutrophils.....</b>	<b>109</b>
<b>Figure 3.4: LcrV does not impact HL-60 chemotaxis.....</b>	<b>111</b>
<b>Figure 3.5: FPR1 agonists in <i>Y. pestis</i> supernatant are N-terminally</b>	
<b>formylated.....</b>	<b>112</b>
<b>Figure 3.6: Deformylation of <i>Y. pestis</i> supernatant reduces neutrophil</b>	
<b>chemotaxis.....</b>	<b>113</b>
<b>Figure 3.7: Bacterial growth conditions and transposon insertions in</b>	
<b>specialized secretion systems do not impact secretion of the</b>	
<b>Fpr1 agonists in <i>Y. pestis</i> supernatant.....</b>	<b>114</b>
<b>Figure 3.8: Multiple HPLC C18 fractions have Fpr1 agonist activity.....</b>	<b>115</b>

## LIST OF TABLES

Table 1.1: Top 25 FPR1 allele variants from the gnomAD v2.1.1 database.....	83
Table 1.2: Primers used in this thesis.....	84
Table 1.3: CRISPR gRNAs used in this thesis.....	85

## **ACKNOWLEDGEMENTS**

There are so many amazing individuals who have helped me through my time at the University of Chicago. To begin, my fantastic wife, Megan Barnett, has been a bedrock of support since we met during our time at UC Berkeley. Her support through late nights at the lab, long stretches of negative data, and the many forms of stress and conflict that arise through the course of a Ph.D. has made my work possible. Beyond my home support system, I also had the great luck of studying with an incredible group of graduate students in the Committee on Microbiology. Their support, mentorship, and advice always seemed to come at the exact right time to support my research and keep me moving forward. Finally, I want to acknowledge my late advisor Olaf Schneewind. While I only had a few short months to learn from him, I can truly say that he was the sharpest scientist I have ever known. His ability to excite researchers about their projects and tap into their passion for science was unmatched. Working with Olaf was a privilege and a joy that set me up for success in my thesis research. I will always miss him and remember his mentorship.

## ABSTRACT

Pathogenic bacteria undergo a multitude of interactions with host immune cells to establish an infection and cause disease. One of these interaction axes involves the formyl peptide receptors (FPRs) used by innate immune cells to detect and kill invading bacteria. Despite the importance of these receptors in driving early immune responses to pathogens, few resources exist to study these receptors *in vivo*. Here, we generate Fpr2<sup>-/-</sup>, Fpr3<sup>-/-</sup>, Fpr1/3<sup>-/-</sup>, and Fpr1/2/3<sup>-/-</sup> mice to aid in the study of combinational effects of FPRs during bacterial infection. Using these new tools, we find that Fpr1<sup>-/-</sup>, Fpr2<sup>-/-</sup>, and Fpr3<sup>-/-</sup> mice have a delayed time-to-death during lethal challenge with *Yersinia pestis*. These survival phenotypes could not be solely attributed to altered chemotaxis or bacterial effector translocation by the type III secretion system. Additionally, we find that Fpr1, but not Fpr2 or Fpr3, is activated by N-terminally-formylated peptides secreted by *Y. pestis*. Together, these experiments reveal a convoluted interaction between formyl peptide receptors and plague-causing *Yersinia*.

## INTRODUCTION

### Background

*Yersinia pestis* is one of the deadliest human pathogens, having accounted for at least three major pandemics, including the Black Death of the 14<sup>th</sup> century that killed an estimated 15 - 23.5 million Europeans.<sup>1</sup> The pathogen is transmitted from rodent reservoir species to humans via fleas, which can inoculate the bacterium intradermally upon biting a suitable host. Such infections cause bubonic plague disease and are characterized by massive swelling of draining lymph nodes, termed buboes. Bubonic plague carries a high mortality rate (30 - 60%) when left untreated due to the innocuous nature of the infection route and the swiftness of pathogen dissemination in infected host.<sup>2</sup> Large pandemics are further exacerbated upon replication of the bacterium in lung tissues which results in pneumonic plague disease<sup>3</sup> and transmission between humans via contaminated aerosols. This form of the disease carries a 100% mortality rate when left untreated.<sup>2</sup> Pneumonic plague is believed to be the most relevant plague manifestation for modern day pandemics and represents a weapon for bioterrorism. In Africa, plague outbreaks continue to re-emerge.<sup>4</sup> While plague infections can be treated with antibiotics, there is currently no FDA-approved vaccine to protect against plague in the United States. As such, there remains a need to better characterize the interactions between *Y. pestis* and the human immune system in the hopes of revealing novel vaccine targets and intervention strategies.

## **Inflammation and Dissemination During *Y. pestis* Infection**

Infection with *Y. pestis* is characterized by robust recruitment of innate immune cells to sites of inoculation.<sup>5,6</sup> During a bubonic plague infection of the dermal layer, *Y. pestis* is inoculated into the skin of a host via flea bite.<sup>7</sup> Innate immune cells, in particular neutrophils, are then recruited to the bacterial inoculation site.<sup>8</sup> This recruitment can be due to either direct sensing of bacterial pathogen-associated molecular patterns (PAMPs), sensing of damage-associated molecular patterns (DAMPs) released by damaged epithelial cells during the flea bite itself, or amplified recruitment chemokines secreted by epithelial cells.<sup>9</sup> Intriguingly, upregulation of inflammatory cytokines and chemokines is typically not observed during bubonic plague infection<sup>10,11</sup> or pneumonic plague infection,<sup>12</sup> suggesting that direct sensing of PAMPs or DAMPs are the major contributors to neutrophil influx at inoculation sites. Regardless, *Y. pestis* eventually disseminates away from the site of inoculation to the local draining lymph node, where a replication niche is formed.<sup>13</sup> Massive amounts of bacterial replication and immune cell recruitment at these lymph nodes cause large amounts of swelling in the host, which forms the characteristic bubo of bubonic plague.<sup>14</sup> After replicating in the lymph node, the bacteria undergo a second dissemination event where they reach the bloodstream and many critical organs, including the liver and spleen.<sup>3</sup> Without intervention, the host will typically die as a result of organ failure. In mice and humans, the entire infection from inoculation to death only takes approximately 7 days.<sup>3</sup>

The infection process for pneumonic plague is similar to that of bubonic plague.<sup>12</sup> Bacteria are inoculated into the lungs and disperse into alveolae, the air exchange sacs within the lungs that house resident alveolar macrophages. The initial infection is also

characterized by a lack of inflammatory cytokine and chemokine release, and massive inflammation begins approximately 48 hours post-infection. This inflammation becomes so aggressive that it causes severe tissue damage of the lungs, which kills the host.<sup>12</sup> In this way, pneumonic plague is a more rapid form of disease and does not require any dissemination steps to cause mortality.

There are several steps of the bubonic plague infection process that remain poorly understood. The first is the mechanism of bacterial dissemination from the site of inoculation to the draining lymph node. A historical view has been that *Y. pestis* is likely being brought to the lymph nodes within macrophages and dendritic cells.<sup>15</sup> This hypothesis is attractive because *Y. pestis* is capable of forming a replicative compartment within macrophages and neutrophils, termed the *Yersinia* Containing Vacuole (YCV).<sup>16,17</sup> Additionally, *Y. pestis* also expresses an important virulence antigen only when the bacteria are in acidic conditions and mammalian body temperature (pH6 antigen).<sup>18</sup> Such virulence gene expression implies that bacterial passage through macrophages is important to enable enhanced bacterial virulence. An important caveat, however, is that macrophages are traditionally not thought to home to lymph nodes for antigen display, but recent evidence suggests that some subpopulations of macrophages and neutrophils can migrate from sites of inflammation to draining lymph nodes.<sup>19</sup> Regardless, antigen presentation in the lymph node is typically performed by dendritic cells, yet it is not clear if dendritic cells can be exploited by *Y. pestis* to the same degree as macrophages. A more recent study suggests the possibility of passive dissemination. In this study, the authors observed that *Y. pestis* can reach the draining lymph node within minutes of injection despite the lack of flagella with a rate similar to a diffusible dye; such a rate is

much faster than the hours required for immune cells to home to the draining lymph node.<sup>20</sup> This alternative dissemination mechanism suggests that the bacteria undergo extracellular diffusion to the draining lymph node. Although it remains unclear which dissemination model is most accurate, it is clear that interactions between *Y. pestis* and innate immune cells, either to avoid antibacterial immune cell activities or exploit their lymph node homing activities, are critical for the progression of plague disease.

### **Type III Secretion**

The major virulence factor causing the high lethality of *Y. pestis* is its type III secretion system (T3SS) located on the virulence plasmid pCD1. T3SS is a virulence mechanism conserved across many human pathogens, some of which are listed by the World Health Organization as priority targets for antibiotic development.<sup>21</sup> T3SS are evolutionarily related to the flagellum and comprise: a double membrane-spanning basal body, a hollow needle extending extracellularly from the bacterium, and a needle tip complex headed by a needle tip protein (*i.e.* LcrV in *Yersinia* species). Pore forming proteins (YopB and YopD in *Yersinia*) are inserted into the target host cell and coupled to the T3SS to form a continuous channel between the bacterium and target cell.<sup>22</sup> This allows for direct translocation of effector proteins from bacterial to host cytosol. These effectors then antagonize host cell processes like phagocytosis, focal adhesion maintenance, and gene transcription.<sup>23</sup> In the case of plague, these effectors also cause the destruction of innate immune cells to subvert the host immune response.<sup>24</sup>

T3SS effector translocation has long been known to be a targeted process. Marketon et al. described the target cell selection for *Y. pestis* using a beta-lactamase

reporter approach with a bubonic plague mouse infection model, where they observed that neutrophils, macrophages, and dendritic cells were preferentially injected with T3SS effector proteins over other cell types.<sup>24</sup> This same target cell selection was also observed using the same reporter system in a pneumonic plague mouse infection model, although dendritic cells were targeted at a much lower frequency.<sup>6</sup> These investigations suggest that target cell selection is conserved across infection routes for *Y. pestis*. Such cell specificity appears rational given that *Y. pestis* must escape from robust innate immune cell recruitment early during the infection process and so targeted destruction of these cell types may better enable the bacterium to avoid killing and disseminate to distal tissues.

Target cell specificity might occur at a few distinct steps during T3SS formation, one of which is insertion of pore forming proteins into target cells. Insertion of the *Y. pestis* T3SS pore forming proteins YopB and YopD into host cells is not fully understood, but it has been observed that these proteins can form pores in red blood cells,<sup>25</sup> therefore suggesting that the insertion process is not necessarily targeted and therefore may not represent the specificity determining step in target cell selection. LcrV oligomerizes and presumably acts as a scaffolding platform to allow for interaction with a cognate receptor on a target cell; presumably, contact between LcrV and host cell receptor triggers the insertion of pore forming proteins (also encoded by the T3SS) into the target cell membrane, thus completing the assembly of the T3SS.<sup>26</sup>

Recently, our laboratory reported that *Y. pestis* LcrV interacts with Formyl Peptide Receptor 1 (FPR1) on the human macrophage-like U937 cell line.<sup>27</sup> This interaction was reported to be required for T3SS-mediated injection of cells by *Y. pestis*.<sup>27</sup> Using an *in*

*vivo* bubonic plague infection model, mice lacking the mouse ortholog of human FPR1 (termed Fpr1 in mice) exhibited a delayed time-to-death and an approximate 20 - 30% survival rate following plague infection.<sup>27</sup> While this result indicates that the presence of Fpr1 in mice enhances plague-induced morbidity, the survival rate does not reach that seen in wildtype mice infected with *Y. pestis* lacking *lcrV* (100% survival rate during *Y. pestis*  $\Delta$ LcrV infection).<sup>28</sup> This suggests that there may exist multiple redundant surface proteins in mice that are exploited by *Y. pestis* to target cells for T3SS intoxication. Alternatively, the lack of Fpr1 may impact immune cell responses during *Y. pestis* infection, such as reducing the chemotactic ability of innate immune cells and therefore reducing immune cell influx to the site of inoculation. Data thus far argues against this possibility,<sup>27</sup> but more detailed studies will be required to identify alternative roles for Fpr1 during plague infection. Further studies are warranted because deletion of Fpr genes typically renders mouse lines significantly more susceptible to bacterial infections as observed with *Escherichia coli*, *Listeria monocytogenes*, and *Streptococcus pneumoniae*.<sup>29-31</sup> This enhanced susceptibility is generally interpreted as a lack of immune cell recruitment to infection sites and not due to changes in antagonistic activities by bacteria. Thus, the enhanced resistance of Fpr1 knockout mice to *Y. pestis* infection is unusual.

### **Formyl Peptide Receptors**

Formyl Peptide Receptors (FPRs) are a class of G Protein Coupled Receptor (GPCR) expressed on innate immune cells for the purpose of detecting and responding primarily to formylated peptides produced by invading bacteria and mitochondria.

Activation of FPRs can simultaneously induce several pathways, including superoxide production, cell chemotaxis, and transcriptional upregulation of cytokines and chemokines.<sup>32</sup> FPR ligands include a very diverse range of peptides, lipids, and small molecules.<sup>33</sup> This diversity makes it difficult to predict FPR agonists and antagonists. Even FPR agonists of the same type, like formylated peptides, lack a consensus sequence motif. For example, the FPR agonists fMLF (N-formylmethionyl-leucyl-phenylalanine), fMMYALF, and fMGIIAGIIKFIKGLIEKFTGK are all capable of activating FPR1, yet these peptides range in length and amino acid composition.<sup>33</sup>

Recent reports have found that pathway activation is dependent on ligand concentration. Specifically, FPR1 was found to have two distinct binding pockets for the prototypical agonist fMLF.<sup>34</sup> The high-affinity binding site is occupied by fMLF at sub-nanomolar concentration and biases signaling towards cell chemotaxis. The low-affinity binding site becomes occupied at high nanomolar concentration and above and preferentially induces bactericidal activities like phagocytosis. These signaling biases are possible due to differential FPR1 structure changes induced by the binding of fMLF at these separate sites. In this way, the innate immune system takes advantage of signaling bias to allow the same bacterial agonists to induce chemotaxis when the bacteria are distant and agonists are at low concentration while also allowing the system to switch to bactericidal functions when bacteria are near and agonists are at high local concentrations.

The human genome contains three FPR genes: FPR1, FPR2, and FPR3. These genes are most robustly expressed in innate immune cells (i.e. neutrophils and macrophages).<sup>32</sup> The mouse genome contains seven FPRs named *Fpr* or *Fpr-rs*: Fpr1

and *Fpr2* (*Fpr-rs2*) are expressed only in immune cells, *Fpr3* (*Fpr-rs1*), *Fpr-rs3*, *Fpr-rs4*, and *Fpr-rs6* are expressed in the vomeronasal organ (VNO) as repurposed pheromone receptors, and *Fpr3* (*Fpr-rs1*) is expressed in both immune cells and the VNO.<sup>35</sup> This expression pattern is the result of two splice variants that promote *Fpr3* gene transcription either from the *Fpr2* promoter or the *Fpr3* promoter, resulting in gene expression in innate immune cells and in the VNO, respectively.<sup>35</sup> In this way, the mouse FPR repertoire has expanded greatly since the evolutionary divergence of mice and humans, yet mice and humans retain a set of three FPRs that are expressed in innate immune cells, presumably for the purpose of pathogen detection.

Sequence comparison and phylogeny analysis suggest that the mouse and human FPRs are orthologs. However, mouse *Fpr2* and *Fpr3* are more closely related to each other than to either human FPR2 or FPR3.<sup>36</sup> FPR orthologs can also be determined using functional assays, such as calcium mobilization or cell chemotaxis in response to known FPR agonists. Such approaches demonstrate that human FPR1 and mouse *Fpr1* as well as human FPR2 and mouse *Fpr2* are functional orthologs, as they respond to very similar sets of agonists.<sup>37</sup> Mouse *Fpr3* is less well characterized and does not functionally behave like any of the human FPRs. In fact, a bacterial-derived formylated peptide capable of activating *Fpr3* was only recently described.<sup>38</sup> The divergence of these genes makes mice an insufficient model for extrapolating *in vivo* FPR-bacteria interactions to human health, yet mouse models remain crucial for placing FPR contributions to bacterial pathogenesis and host immune responses in the context of the whole body. In this way, FPRs must be studied using a combination of *in vivo* and *in vitro* experimental approaches to fully grasp their activation states and relevance to infections.

A study recently discovered that there are two naturally occurring Fpr3 variants found within in-bred mouse genomes.<sup>39</sup> Wildtype Fpr3 is found in C57BL/6J, I/LnJ, NOD/ShiLtJ, and many other common mouse lines. The second Fpr3 variant contains a 4 amino acid in-frame deletion within one of the transmembrane helices of the protein and is also found in many common mouse lines, including BALB/cJ, 129S1/SvImJ, and DBA/2J. This deletion leads to the destruction of Fpr3 before it can be transported to the cell surface, presumably by making the translated product unstable.<sup>39</sup> This deletion therefore makes mouse strains containing this gene variant natural Fpr3 knockout animals, which may have yet unappreciated impacts on bacterial infection models. For the purposes of this dissertation, the unstable Fpr3 allele variant will be referred to as “Fpr3  $\Delta$ 4” in reference to its loss of 4 amino acids.

To date, most studies involving FPR knockout mice have utilized mice developed by Dr. Philip Murphy’s laboratory at the National Institute of Health (NIH).<sup>31,40–44</sup> This is of particular relevance because the Murphy laboratory utilized *ex vivo* embryo mutagenesis to generate their FPR knockout mouse lines. While this was effective in generating knockout mice of Fpr1 and Fpr2, these knockout mice were generated using embryos derived from 129/Sv mice.<sup>40</sup> These mice notably contain the Fpr3  $\Delta$ 4 gene variant. While the mice generated as a result of these embryo mutagenesis experiments were thoroughly backcrossed to C57Bl/6 mice, the FPR genes are known to reside in a locus on Chromosome 17 that is approximately 150 kb in total length. This distance is well within the length limits for nearly guaranteeing gene linkage. Briefly, gene linkage is used to refer to genes that segregate together during breeding experiments. The traditional quantification of genetic linkage is centi-Morgan (cM). 1cM is defined as a gene

recombination rate of 1%, and it has been found that 1cM is approximately equivalent to 2,000 kb distance between two genes.<sup>45</sup> This means that for the 150 kb FPR locus, recombination will occur in approximately 0.05% of all meiotic events and therefore that combinational FPR knockout mice cannot be feasibly generated through breeding. So, while wildtype C57Bl/6 mice contain a functional Fpr3 allele, the C57Bl/6 “isogenic” FPR knockout mice currently used in the field contain a null Fpr3 allele. This problem poses an urgent need to generate FPR knockout mice with the functional Fpr3 allele to understand the role that Fpr3 is playing in bacterial infection models.

There is experimental evidence in the literature suggesting that Fpr3 may play important roles in *Y. pestis* pathogenesis *in vivo*. BALB/cJ and 129S1/SvImJ mice, which carry the Fpr3  $\Delta 4$  allele, are known to be more resistant to systemic plague infection than C57BL/6J mice. One study explained this difference based on the MHC locus on Chromosome 17 for BALB/cJ mice and Chromosome 1 for 129S1/SvImJ mice.<sup>46,47,48</sup> While most of the resistance observed with 129S1/SvImJ mice may be independent of Fpr3, it is notable that the BALB/cJ resistance gene could be mapped to Chromosome 17, the same location as the FPR locus. It is also important to note that the mapping of the BALB/cJ resistance gene was done using quantitative trait locus (QTL) analysis, but the mapping did not produce highly resolved LOD score peaks and therefore cannot rule out the presence of other resistance genes on Chromosome 17. Lastly, in the above-mentioned studies, animals were infected with an attenuated plague variant lacking the 102 kb pigmentation locus, so it is not clear if the same resistance phenotypes would be observed during infection with fully virulent bacteria such as *Y. pestis* CO92. Regardless, the possibility that Fpr3 impacts *Y. pestis* infection outcomes deserves further

investigation to better understand how mouse line selection might impact data interpretation.

Expanding upon this point, the Gram-positive pathogen *Staphylococcus aureus* is known to produce multiple proteins that can act as antagonists or agonists for FPR1 and FPR2.<sup>49–52</sup> While several of these interactions occur with FPR orthologs across species (i.e. human FPR1 antagonist FLIPr-like also antagonizes mouse immune cell migration, presumably through Fpr1<sup>53</sup>), not all interactions behave the same when comparing binding to human vs. mouse FPRs (i.e. CHIPS interacts strongly with human FPR1 but very weakly with mouse Fpr1<sup>51,54</sup>). These interaction discrepancies could be resolved by developing better *in vivo* FPR models. In *S. aureus*, FPR-interacting proteins are encoded as clusters on mobile genetic elements named Immune Evasion Cluster 1 and 2 (IEC1 and IEC2). IEC1 and IEC2 can jump between bacterial strains presumably to enhance virulence or adapt to host.<sup>55</sup> In general, infection of mouse lines containing wildtype Fpr3 correlates with increased resistance to systemic *S. aureus* infections.<sup>56,57</sup> This is in agreement with our current understanding of the role of FPRs during bacterial infections; Fpr3 surface expression may be important for resistance to *S. aureus*. Thus, mouse FPRs could play a fundamentally different role during *Y. pestis* infections compared to other bacterial infections.

Although Fpr3 functionality correlates with differences in bacterial susceptibility and resistance, it remains unclear how active of a role Fpr3 plays during *in vivo* bacterial infections. A recent study uncovered the first direct interaction between bacteria and Fpr3, as it described a conserved peptide motif that acts as an agonist for mouse Fpr3.<sup>38</sup> This motif is found at the N-termini of the MgrB and EsaA proteins, which are present in many

relevant pathogenic bacterial genera, including *Escherichia*, *Salmonella*, *Bacillus*, *Shigella*, and *Enterococcus*. The presence of the *mgrB* gene also correlates with higher biocontainment levels (and therefore more severe disease outcomes), as most bacterial strains containing the *mgrB* gene fall in the Risk Group 2 and Risk Group 3 biosafety categories.<sup>38</sup> Of course, these biosafety designations are designed based on human pathogenicity and this study defined the N-terminus of MgrB as a mouse Fpr3 agonist, so it remains unclear if the FPR agonist properties of MgrB translate to humans. Nonetheless, it appears that several distinct bacterial species that cause severe human disease may interact with the divergent mouse Fpr3 protein. A physiological relevance to human disease remains to be determined and may be further elucidated by combining mouse infection models with sophisticated *in vitro* technologies like PRESTO-Tango.<sup>58</sup>

Activation of FPRs has also been shown to alter secondary responses during bacterial infections. One research group has found that activation of FPRs with traditional formylated ligands can alter the production of inflammatory cytokines and chemokines induced by subsequent activation of TLRs.<sup>59</sup> Additionally, Fpr2 has been implicated as a significant contributor to neutrophil swarming.<sup>60</sup> During neutrophil chemotaxis to sites of damage or infection, a phenomenon called neutrophil swarming occurs, where neutrophils that directly detect PAMPs or DAMPs produce secondary signaling molecules that amplify the chemotactic response of more distant neutrophils.<sup>61</sup> The dominant mediator for this response is leukotriene B<sub>4</sub>, as loss of the leukotriene B<sub>4</sub> receptor abrogates the majority of neutrophil swarming phenotypes.<sup>60</sup> Loss of Fpr2, however, was also shown to have a significant, if less robust, impairment for neutrophil swarming.<sup>60</sup>

In addition to their roles in responding to bacterial infections, FPRs play distinct functions in host development and cancer. One such developmental role is in the migration of mesenchymal stem cells to wound sites, where they can participate in wound healing activities.<sup>62</sup> Activation of FPR1 on mesenchymal stem cells has also been shown to promote differentiation of these stem cells into osteoblasts, giving FPR1 a direct role in bone growth.<sup>63</sup> This differentiation effect also holds true for neural stem cells, as FPR1 activation induces neural stem cells to differentiate into neurons while inhibiting differentiation into astrocytes.<sup>64</sup> Such activity may prove important in healing brain and spine injuries. Finally, FPR1 is a highly polymorphic gene product (Table 1). This is partially due to the natural variation that comes from a gene product in an active evolutionary battle with microbes.<sup>65</sup> However, this variation may also be linked to cancer, as FPR1 expression levels are differentially regulated in several forms of cancer.<sup>66-68</sup> Future studies will be needed to understand how the common FPR1 allele variants (Table 1.1) impact cancer progression and tissue development.

### **Concluding Thoughts**

Putting together these background topics, we see that FPRs play a complex role in host physiology. Not only do the FPRs aid in responding to bacterial infections but they also play key roles in host development and wound healing. Given this complexity, the research community needs a broad array of tools, both *in vivo* and *in vitro*, to pinpoint the precise roles for each FPR during different processes.

## **MATERIALS AND METHODS**

### Primers Used in this Study

See Table 1.2 for primer sequences and descriptions.

### Bacterial Growth Conditions

*Escherichia coli* strains were grown on LB Agar (Difco) or LB broth (Difco) at 37 °C. *Yersinia pestis* KIM D27 strains were grown on Heart Infusion Agar (HIA; Difco) or Heart Infusion Broth (Difco) at 26 °C or room temperature. *Yersinia pestis* CO92 strains were grown on HIA supplemented with Congo Red Dye (Millipore Sigma) or HIB at 26 °C. *Staphylococcus aureus* strains were grown on Tryptic Soy Agar (TSA; Difco) or Tryptic Soy Broth (Difco) at 30 °C or 37 °C. All cultures were supplemented with ampicillin, chloramphenicol or rifampicin (Millipore Sigma) as needed.

### PCR Reaction Conditions and Agarose Gel Electrophoresis

All polymerase chain reactions (PCR) in these studies were performed under identical conditions and used Z-Taq (TaKaRa), NEB Taq (NEB) or Phusion (Thermo Fisher) as the polymerase source. All polymerases were used with their corresponding buffers per the specific instructions from each manufacturer. The following thermocycling conditions were used for each reaction: Initial denaturation: 1 cycle at 95 °C for 10 min; Product Amplification: 35 cycles at primer-specific annealing temperature (Average  $T_m$  according to IDT calculation) for 30 sec, 72 °C for amplicon length-specific time (1 min per 1 kb), 95 °C for 30 sec; Final Extension: 1 cycle 72 °C for 10 min. PCR reactions were confirmed for accuracy by agarose gel electrophoresis. SeaKem LE

Agarose (Lonza Bioscience) was added to TAE buffer to a final concentration of 1% w/v. Agarose mixtures were then heated in a microwave until all agarose was dissolved in solution. Agarose solutions were set into trays with well combs and transferred to electrophoresis tanks. PCR samples were mixed with Gel Loading Dye, Purple (6X) (NEB) and 10 – 15  $\mu$ l of each sample were loaded into wells of the agarose gel. 1kb plus DNA ladder (Invitrogen) was included as a size control. Agarose gels were subjected to electrophoresis at a constant voltage of 150V for 30 – 45 min. Gels were then post-stained by incubation with GelRed (Biotium) for 45 – 60 min. Gel images were captured with a Fotodyne FOTO/Analyst FX instrument with PC Image software.

#### SDS-PAGE Gel Preparation

15% SDS-Polyacrylamide gels were cast in batches of 12 gels. Glass covers, plastic spacers, and metal backs were assembled into the gel casting reservoir. Separating gel solution (26.25 ml 1M Tris [pH 8.75]; 0.7 ml 3M NaCl; 0.7 ml 0.2M EDTA; 26.25 ml 40% Acrylamide; 15.75 ml deionized water; 0.7 ml 10% APS; 0.028 ml TEMED) was mixed in a glass Erlenmeyer flask and poured into the gel casting reservoir. Solution was added with sufficient room to accommodate well combs. 70% Isopropanol was poured on top of the gels to ensure a flat stacking gel surface. Gels were left to polymerize for 45 min. The isopropanol was poured off the gels and stacking gel solution (4.67ml 1M Tris [pH 6.8]; 0.35 ml 3M NaCl; 0.35 ml 0.2 ml EDTA; 4.9 ml 40% Acrylamide; 25 ml deionized water; 0.35 ml 10% APS; 0.035 ml TEMED) was poured on top of the gel casts. Well combs were quickly added to each gel cast. Gels

were left to set for 45 min. Gels were removed from the casting reservoir, covered with a moist paper towel and plastic wrap, and stored at 4 °C.

### SDS-PAGE Coomassie staining

15% SDS-PAGE gels were placed in an electrophoresis chamber. Running Buffer (30.2 g Tris, 144 g Glycine, 10 g SDS, fill to 10 L final volume with dH<sub>2</sub>O) was added to the top chamber and bottom chamber to expose both gel surfaces to buffer. 10 – 15 µl of sample was added to wells as needed. 1 µl PageRuler Plus Prestained Protein Ladder (Thermo Scientific; 10 to 250 kDa) was used as a molecular weight marker. Gels were run at a constant 150 V until the dye front reached the bottom of the gels (approximately 1 h 45 min). Gels were carefully transferred to square dishes, and Coomassie Staining Reagent (0.5g Coomassie R-250, 150 ml methanol, 325 ml dH<sub>2</sub>O, 25 ml acetic acid) was added until it completely covered the gel. Gels were placed in a microwave for 15 – 30 sec to briefly heat the reagent. Dishes were transferred to a shaker and left to incubate at room temperature until the gel became completely stained with dye. Coomassie Staining Reagent was poured off into a waste container, and Coomassie Destaining Reagent (200 ml acetic acid, 800 ml methanol, 1 L dH<sub>2</sub>O) was added to the dish along with 1-2 Kim wipes to collect residual R-250 dye. The Coomassie Destaining Reagent was replaced with fresh reagent 2-3 times with long incubation periods in between. Gels were removed from the Coomassie Destaining Reagent when the background gel staining was nearly absent (*i.e.*, when the gel became clear but while protein bands were clearly visible).

## Embryo mutagenesis and breeding strategy

To generate mice lacking Fpr1, Fpr2, and Fpr3, we utilized a CRISPR Cas9 targeted deletion approach on an Fpr1<sup>-/-</sup> mouse background generated by Dr. Philip Murphy<sup>40</sup>. In this approach, we designed CRISPR crRNAs targeting the splice site and coding region of the Fpr2 gene and the coding region of the Fpr3 gene. crRNAs (IDT) and tracrRNA (IDT) were diluted in TE buffer to 1 µg/µl final concentration. 5 µg of each crRNA was mixed individually with 10 µg of tracrRNA to generate full gRNA complexes. These mixtures were incubated for 5 min at 95 °C and then cooled down to 25 °C at a rate of 5 °C per min in a thermocycler. The gRNA complexes were diluted to 75 ng/µl final concentration in nuclease-free water and Cas9 was added to a final concentration of 300 ng/µl. These mixtures were incubated for 10-15 min at room temperature to allow RNP complex formation. The mixtures were centrifuged for 10 min at 20 x g, 4 °C and the top 65 µl of the supernatant was taken on ice to the Transgenic Mouse and Embryonic Stem Cell Facility at the University of Chicago. Staff at this facility injected embryos isolated from a WT C57Bl/6 female / Fpr1<sup>-/-</sup> male breeding cross with the gRNA/Cas9 RNPs and implanted these injected embryos into Swiss Webster mice. The resulting pups were genotyped using primers specific for the parent Fpr1 deletion gene, Fpr2 CRISPR-targeted region, and Fpr3 CRISPR-targeted region. Mice with deletions in Fpr2 and/or Fpr3 were confirmed by DNA sequencing and bred to homozygosity. With this approach, we isolated the following mouse lines: FPR1<sup>+/+</sup> FPR2<sup>-/-</sup> FPR3<sup>+/+</sup>, FPR1<sup>+/+</sup> FPR2<sup>+/+</sup> FPR3<sup>-/-</sup>, FPR1<sup>-/-</sup> FPR2<sup>+/+</sup> FPR3<sup>-/-</sup>, and FPR1<sup>-/-</sup> FPR2<sup>-/-</sup> FPR3<sup>-/-</sup>.

### Tissue digestion for genotyping

Mice at weaning age or older were hand-restrained and ear clipped with sharp scissors. Ear clips were transferred to 1.5 ml tubes. 50  $\mu$ l Alkaline Lysis Reagent (25 mM NaOH, 0.2 mM EDTA) was added, and samples were incubated for 30 min at 95 °C. 50  $\mu$ l Neutralization Reagent (40 mM Tris-HCl) was added to each tube. Samples were stored at 4 °C. 1  $\mu$ l of each sample was used for PCR genotyping reactions.

### PDF expression and purification

PDF-pET15b was transformed into *E. coli* BL21 (DE3). PDF-pET15b BL21 colonies were inoculated in LB supplemented with 100  $\mu$ g/ml ampicillin and grown overnight at 37 °C with 200 rpm shaking. Two 5 ml-overnight cultures were diluted into 250 ml LB supplemented with ampicillin and 1.6 mM FeCl<sub>3</sub> and grown at 37 °C with shaking for 2.5 h to an optical density at 600 nm (OD<sub>600</sub>) of 0.5 - 0.6. 1 ml of 100 mM IPTG added to each culture to induce PDF expression, and cultures were grown for 5 h at 37 °C with shaking. Bacterial pellets were collected by centrifugation at 5000 x g, 4 °C for 10 min and were stored at -80 °C. Bacterial pellets were thawed and resuspended in 20 ml column buffer (50 mM Tris-base, 150 mM NaCl, 10 mM imidazole, 10  $\mu$ g/ml catalase, pH 7.5). Samples were sonicated on ice at 70% amplitude for 10 cycles of alternating 30 sec on with 30 sec off. Lysed samples were centrifuged for 20 min at 12000 x g, 4 °C. The chromatography column was washed with 70% isopropanol followed by water, then 2 ml 50% Ni-NTA beads were added to the column. The beads were washed with 40 ml column buffer and the column was moved to 4 °C. Cleared lysate was added to the column and the flow-through was re-run on the column twice. The beads were

washed with 40 ml column buffer and the sample was eluted with 2 ml of column buffer supplemented with imidazole to the following final concentrations: 30 mM, 50 mM, 100 mM, 200 mM, 300 mM, 400 mM, and 500 mM. Fraction purity was assessed by running fractions via 15% SDS-PAGE and staining with Coomassie Blue dye. Pure fractions with high protein yield were pooled, mixed 1:1 with 40% glycerol, and stored at -80 °C. The final PDF concentration was 120.5 µg/ml, as determined by BCA (Thermo Fisher).

#### BS1 isolation from mouse passaging

*Y. pestis* CO92 was grown on HIA supplemented with 0.2% galactose and 0.01% Congo Red dye. Colonies were inoculated in 5 ml HIB and grown overnight at 26 °C with shaking. Overnight cultures were diluted to 10000 CFU/ml in PBS using reference OD600 readings. Mice were injected subcutaneously in the left inguinal fold with 100 µl bacteria. Mice exhibiting signs of disease were euthanized at 72 hpi. Spleens from these mice were harvested and transferred to sterile Whirl-Pak bags containing 1 ml PBS. Spleens were homogenized by hand mashing using a 50 ml conical tube. Samples were plated on HIA supplemented with Congo Red dye and grown at 26 °C for 48 – 72 h to isolate *Y. pestis*. One Congo Red-positive colony was chosen and used for infection in the same procedure as above. Infected mice were again euthanized at 72 hpi and spleens were homogenized and plated for *Y. pestis* isolation. A Congo Red-positive colony was chosen and restreaked to ensure bacterial homogeneity. Colonies were grown overnight in HIB, mixed 1:1 with 40% glycerol, and stored at -80 °C.

### Bubonic Plague Mouse Survival Infection

*Y. pestis* CO92 was streaked from -80 °C freezer stocks onto HIA supplemented with 0.2% galactose and 0.01% Congo Red dye and grown for 48 – 72 h at 26 °C. A single Congo Red-positive colony was used to inoculate 5 ml HIB and grown overnight at 26 °C with shaking. The overnight culture was diluted in PBS to the final CFU/ml concentration by using OD600 measurements. 100 µl of the final bacterial preparation was used to infect mice subcutaneously in the left inguinal fold. Mice were monitored for up to 14 days and euthanized according to IACUC-approved experimental endpoints.

### Bubonic Plague Dissemination Infection

Mice were infected with *Y. pestis* CO92 using the same method as described above. Mice were euthanized 48 hpi or 72 hpi by forced CO<sub>2</sub> inhalation followed by cervical dislocation. Mice were pinned back-down to a Styrofoam board and the skin and peritoneal wall were carefully dissected away using isopropanol-sterilized forceps and scissors. The spleen from each mouse was removed and transferred to a Whirl-pak bag. 1 ml PBS was added and the spleen was homogenized by mashing with a 50 ml conical tube. The spleen homogenate was transferred to a 96-well plate. 10-fold dilutions were made by transferring 10 µl of homogenate to 90 µl PBS. This was performed 7 times. 10 µl of each dilution (neat sample through 10<sup>-7</sup>) was drawn into a multichannel pipette and gently dispensed at the top of a square HIA plate. The plate was tilted to allow samples to run down the agar surface. Plates were incubated for 48 – 72 h at 26 °C and colonies were counted to determine CFU.

### Intraperitoneal (IP) lavage assay – *Yersinia pestis*

*Y. pestis* KIM D27 was inoculated from an agar culture into 5 ml HIB and grown overnight at 26 °C. The overnight culture was centrifuged for 5 min at 7500 rpm and resuspended in 20 ml PBS. The culture was centrifuged again for 5 min at 7500 rpm and the resulting bacterial pellet was resuspended in 5 - 10 ml PBS. OD600 measurements were used to dilute the culture to a concentration of approximately  $1 \times 10^9$  CFU/ml. Mice were hand restrained and injected intraperitoneally with 100  $\mu$ l of bacterial culture (approximately  $1 \times 10^8$  CFU). 3 hours post-infection, mice were euthanized and dissected to reveal the left peritoneal wall. A syringe coupled to a 21g needle and loaded with 5 ml ice-cold PBS + 1% BSA was inserted into the IP cavity of the mouse by traveling through the left hind quad muscle to stabilize the needle and prevent peritoneal wall tearing. The 5 ml PBS + 1% BSA was slowly injected into the IP cavity. The IP cavity was vigorously shaken with forceps for 2 min and approximately 3 ml IP exudate was recovered with a separate syringe. Samples were immediately stored on ice and were separated into aliquots for use in CFU enumeration, flow cytometry, or PRESO-Tango assays.

### Intravenous (IV) *S. aureus* infection

*S. aureus* USA300 was grown overnight at 37 °C on a TSA plate. The next afternoon, one bacterial colony was inoculated into 25 ml TSB in a 125 ml Erlenmeyer flask and grown overnight at 37 °C with shaking at 200 rpm. The next morning, 250  $\mu$ l overnight culture was transferred to 25 ml TSB in a 125 ml Erlenmeyer flask and grown at 37 °C for 2 h or until the culture reached an OD600 reading of 0.4 – 0.6. The bacterial culture was transferred to a 50 ml conical tube and centrifuged at 8000 x g for 10 min at

4 °C. The supernatant was decanted and the bacterial pellet was resuspended in 25 ml PBS by vortexing. The culture was centrifuged at 8000 x g for 10 min at 4 °C and the pellet was resuspended in 2 ml PBS by vortexing. The culture was diluted to an OD600 corresponding to 10<sup>8</sup> CFU/ml. 1 ml bacterial culture was mixed with 1 ml PBS in a 2 ml cryotube to yield a final bacterial suspension of 5 x 10<sup>8</sup> CFU/ml. Actual bacterial concentrations were determined by plating serial dilutions of the final culture suspension on TSA plates and counting colonies. Mice were injected IP with 200 µl anesthesia solution (11 ml 0.9% NaCl; 0.65 ml 100 mg/ml ketamine; 0.25 ml 20 mg/ml xylazine). Mice were confirmed to be unconscious by footpad pinch and injected intravenously (IV) into the right retroorbital sinus with 100 µl bacteria. Mice were monitored until full recovery from anesthesia and then health monitored according to IACUC-approved ACUP methods until the end of the experiment. Mice were euthanized by forced CO<sub>2</sub> inhalation followed by cervical dislocation. Both kidneys from each mouse were dissected and transferred to 15 ml conical tubes containing 1 ml PBS + 1% TritonX-100. Kidneys were homogenized with an Omni Tissue Homogenizer (Omni Inc), serially diluted in PBS, and plated on TSA plates. Plates were incubated overnight at 37 °C, and CFU were enumerated.

#### Intranasal (IN) *S. aureus* colonization

*S. aureus* WU1 carrying a chromosomal rifampicin resistance gene (Rif<sup>R</sup>) was inoculated from freezer stocks onto TSA plates supplemented with rifampicin (50 µg/ml) and grown overnight at 37 °C. The next afternoon, a single colony of *S. aureus* WU1 Rif<sup>R</sup> was inoculated into TSB supplemented with 50 µg/ml rifampicin and grown overnight at

37 °C with shaking at 200 rpm. The next morning, 250 µl overnight culture was transferred to 25 ml TSB in a 125 ml Erlenmeyer flask and grown at 37 °C for 2 h or until the culture reached an OD600 reading of 0.4 – 0.6. The bacterial culture was transferred to a 50 ml conical tube and centrifuged at 8000 x g for 10 min at 4 °C. The supernatant was decanted and the bacterial pellet was resuspended in 25 ml PBS by vortexing. The culture was centrifuged at 8000 x g for 10 min at 4 °C and the pellet was resuspended in 500 µl PBS by vortexing. The culture was diluted to an OD600 corresponding with a concentration of 10<sup>10</sup> CFU/ml. Mice were injected IP with 200 µl anesthesia solution (11 ml 0.9% NaCl; 0.65 ml 100 mg/ml ketamine; 0.25 ml 20 mg/ml xylazine). Mice were confirmed to be unconscious by footpad pinch and slowly injected intranasally (IN) into the left nostril with 10 µl bacteria. Mice were monitored until full recovery from anesthesia. Mice were monitored for colonization by *S. aureus* WU1 every 7 days. Nasopharyngeal samples were taken by swabbing the throat of hand-restrained mice for approximately 10 sec using sterile cotton swabs. Swabs were immediately spread across TSA plates supplemented with rifampicin. Fecal samples were collected from mice and transferred to 2 ml Eppendorf tubes containing 500 µl PBS. Tubes were weighed before and after feces collection for weight quantification. Fecal samples were homogenized using an Omni Tissue Homogenizer, serially diluted in PBS, and plated on TSA plates supplemented with rifampicin. Plates were grown overnight at 37 °C and CFU were enumerated the following morning.

### IP lavage assay – *S. aureus*

*S. aureus* USA300 was inoculated from agar cultures into 25 ml TSB in a 125 ml Erlenmeyer flask and grown overnight at 37 °C with 200 rpm shaking. The next morning, 250 µl bacterial culture was diluted in 25 ml TSB in a 125 ml Erlenmeyer flask. The bacterial culture was grown at 37 °C with 200 rpm shaking for 2 h or until the OD600 reached 0.4 – 0.6. The bacterial culture was transferred to a 50 ml conical tube and centrifuged at 8000 x g for 10 min at 4 °C. The supernatant was decanted and the bacterial pellet was resuspended in 25 ml PBS by vortexing. The culture was centrifuged at 8000 x g for 10 min at 4 °C and the pellet was resuspended in 2 ml PBS by vortexing. The culture was diluted to an OD600 corresponding to 10<sup>9</sup> CFU/ml. Mice were injected IP with 100 µl bacterial culture. 3 hours post-infection, mice were euthanized and dissected to reveal the left peritoneal wall. A syringe coupled to a 21g needle and loaded with 5 ml ice-cold PBS + 1% BSA was inserted into the IP cavity of the mouse by traveling through the left hind quad muscle to stabilize the needle and prevent peritoneal wall tearing. The 5 ml PBS + 1% BSA was slowly injected into the IP cavity. The IP cavity was vigorously shaken with forceps for 2 min and approximately 3 ml IP exudate was recovered with a separate syringe. Samples were immediately placed on ice and aliquoted for flow cytometry or CFU enumeration experiments.

### Percoll purification of elicited peritoneal granulocytes

Mice were hand restrained and injected IP with 1 ml Thioglycollate Medium Brewer Modified (Fisher Scientific). 3 hours post-injection, mice were euthanized and the IP cavity was washed with 5 ml PBS + 0.02% EDTA using the same method as the above IP

Lavage Assay. Peritoneal lavage samples from 2 mice were combined and centrifuged for 10 min at 200 x g. Cell pellets were washed 3 times with 10 ml PBS. The final cell pellet was resuspended in 1 ml PBS and mixed with 9 ml Percoll (Santa Cruz Biotechnology) gradient solution (1 volume 10x PBS pH 7.2, 9 volumes Percoll). Samples were ultracentrifuged for 20 min at 60,650 x g, 4 °C in a swinging bucket rotor. The granulocyte layer was collected and washed with 10 ml PBS. The final cell pellet was resuspended to  $5 \times 10^5$  cells/ml or  $2 \times 10^6$  cell/ml in an appropriate medium for downstream experiments.

#### Flow cytometry of IP lavage

IP exudate samples were separated into 400  $\mu$ l aliquots. Aliquots were centrifuged for 5 min at 500 x g and cell pellets were resuspended in 100  $\mu$ l PBS + 1% BSA. 1  $\mu$ g Mouse SeroBlock FcR (Biorad) was added to each tube, and samples were incubated for 10 min at room temperature. 0.5  $\mu$ g Ly-6G APC-conjugated antibody (1A8-Ly6g; Thermo Fisher) or isotype control antibody (eBR2a; Thermo Fisher) was added to samples as appropriate. Samples were incubated for 30 min on ice. Cells were centrifuged for 5 min at 500 x g and the cell pellet was resuspended in 1 ml PBS + 1% BSA. This step was repeated once. Final cell pellets were resuspended in 300  $\mu$ l PBS + 1% BSA. 0.125  $\mu$ g propidium iodide (PI) and 50  $\mu$ l CountBright Absolute Counting Beads (Thermo Fisher) were added to samples. Cells were counted by flow cytometry (BD Biosciences FACS Canto) with the following gating strategy: single cells selected by FSC-A/FSC-H; granulocytes selected by FSC-A/SSC-A; dead cells were excluded with a PI gate. The stopping gate was set to count 5000 CountBright beads.

### Flow cytometry of blood and spleen samples

Mice were euthanized by forced CO<sub>2</sub> inhalation followed by cervical dislocation. 1 ml syringes coupled with 25g needles were coated with heparin by drawing up 1 ml heparin (1000 U/ml) into the syringe and discarding the solution. Blood was collected by cardiac puncture and transferred to 1.5 ml tubes. Spleens were removed and transferred to Whirl-pak bags. 1 ml PBS supplemented with 1% BSA (PBS/BSA) was added to Whirl-pak bags and spleens were homogenized by crushing with a 50 ml conical tube. Homogenated samples were run through a 40 µm cell strainer into 50 ml conical tubes. 250 µl strained spleen samples and 100 µl blood samples were transferred to 1.5 ml tubes. Samples were centrifuged for 5 min at 200 x g. Cell pellets were resuspended in 1 ml RBC Lysis Buffer (155 mM NH<sub>4</sub>Cl, 12 mM NaHCO<sub>3</sub>, 0.1 mM EDTA) and incubated at room temperature for 15 min. Samples were centrifuged for 5 min at 200 x g, and cell pellets were resuspended in 1 ml PBS/BSA. Samples were centrifuged for 5 min at 200 x g and resuspended in 100 µl PBS/BSA. 1 µl Mouse SeroBlock was added to samples, and samples were incubated at room temperature for 10 min. 0.5 µg of the following rat anti-mouse antibodies were added to each sample: Ly-6G/Ly-6C PerCP-Cy5.5; CD4 FITC; CD8a V450; CD45 BV510; CD11b BB515 (BD Biosciences) Samples were incubated for 30 min at room temperature. 50 µl CountBright Absolute Counting Beads was added to each sample. Samples were quantified using a BD FACSMelody.

### *Y. pestis in vitro* T3SS Injection Assay

*Y. pestis* KIM D27 stably transformed with plasmid pMM83 (previously used in Marketon et al. 2005<sup>24</sup>) was used to measure T3SS injection of U937 cells. Plasmid

pMM83 constitutively expresses the T3SS effector protein YopM fused to the beta lactamase enzyme. This fusion protein is translocated into target cells upon successful T3SS interactions and can be used with the Forster resonance energy transfer (FRET) dye CCF2-AM (Thermo Fisher). CCF2-AM is a cell-permeable small molecule that becomes trapped in mammalian cells upon reaction with host cell esterases that give the molecule an overall negative charge. CCF2-AM is composed of fluorescent molecules that are coumarin and fluorescein derivatives, and these molecules are connected through a beta lactam linkage. In the absence of beta lactamase (*i.e.*, no T3SS effector translocation), FRET activity is maintained and a green emission wavelength will be observed. In the presence of beta lactamase (*i.e.*, productive T3SS effector translocation), FRET activity is lost due to cleavage of the beta lactam ring, and a blue emission wavelength can be observed.

*Y. pestis* KIM D27 pMM83 was grown overnight in HIB supplemented with chloramphenicol. The next morning, the bacterial culture was diluted 1:20 in HIB supplemented with chloramphenicol to a final volume of 20 ml. The culture was grown for 1.5 h at 26 °C with shaking and then shifted to 37 °C for 1.5 h with shaking. During the bacterial growth incubation, U937 cells were centrifuged for 5 min at 200 x g. The cell pellet was resuspended in 20 ml HBSS and the cells were centrifuged again for 5 min at 200 x g. The cell pellet was resuspended to a final cell concentration of  $2 \times 10^6$  cells/ml in RPMI containing 2% BSA. 500  $\mu$ l cell suspension was dispensed into the required number of wells in a 12 well cell culture plate. At the end of the growth period, the bacterial culture was centrifuged for 5 min at 7500 rpm. The cell pellet was resuspended in 20 ml HBSS, and the culture was centrifuged again for 5 min at 7500 rpm. The cell pellet was

resuspended in RPMI containing 2% BSA to a final concentration of  $10^8$  CFU/ml. 100  $\mu$ l bacterial culture was added to U937 cells as required for a final multiplicity of infection (MOI) of 10. Plates were incubated for 3 h at 37 °C, 5% CO<sub>2</sub>. Cells were transferred to 1.5 ml Eppendorf tubes and centrifuged for 3 min at 1500 x g. Cell pellets were resuspended in 100  $\mu$ l RPMI containing 2% BSA and 50  $\mu$ g/ml kanamycin. 6x CCF2-AM was prepared according to the manufacturer's instructions. 20  $\mu$ l 6x CCF2-AM was added to the cells, and tubes were incubated for 1 h at room temperature in the dark. Cells were centrifuged for 3 min at 1500 x g, and cell pellets were resuspended in 500  $\mu$ l HBSS. Cells were centrifuged again for 3 min at 1500 x g, and cell pellets were resuspended in 500  $\mu$ l HBSS. Cells were transferred to round bottom tubes and propidium iodide was added to a final concentration of 0.5  $\mu$ g/ml. Cell fluorescence was quantified using a FACSCanto. Single cells were gated based on forward scatter and side scatter. Live cells were gated based on lack of propidium iodide staining. 10,000 cells were acquired per sample.

#### *Y. pestis in vivo* T3SS Injection Assay

*Y. pestis* KIM D27 pMM83 was inoculated from an agar culture into 5 ml HIB supplemented with chloramphenicol and grown overnight at 26 °C. The overnight culture was centrifuged for 5 min at 7500 rpm and resuspended in 20 ml PBS. The culture was centrifuged again for 5 min at 7500 rpm and the resulting bacterial pellet was resuspended in 5 - 10 ml PBS. OD600 measurements were used to dilute the culture to a concentration of approximately  $1 \times 10^9$  CFU/ml. Mice were hand restrained and injected intraperitoneally with 100  $\mu$ l of bacterial culture (approximately  $1 \times 10^8$  CFU). 3 hpi, mice were euthanized

and IP lavage were collected as described above (see IP lavage assay – *Y. pestis*). 400  $\mu$ l IP lavage samples were aliquoted into 1.5 ml Eppendorf tubes and centrifuged for 5 min at 200 x g. Cell pellets were resuspended in 100  $\mu$ l PBS 1% BSA. 1  $\mu$ l Mouse SeroBlock was added to samples, and tubes were incubated at room temperature for 10 min. 0.5  $\mu$ g anti-Ly-6G antibody and 20  $\mu$ l 6x CCF2-AM was added to tubes, and tubes were incubated for 1 h at room temperature in the dark. Samples were centrifuged for 5 min at 200 x g. Cell pellets were resuspended in 1 ml PBS 1% BSA and centrifuged for 5 min at 200 x g. Cell pellets were again resuspended in 1 ml PBS 1% BSA and centrifuged for 5 min at 200 x g. Cell pellets were resuspended in 300  $\mu$ l PBS 1% BSA and transferred to round bottom tubes. Cell fluorescence was quantified using a FACSMelody with Chorus software. Single cells were gated based on forward scatter and side scatter. Neutrophils were gated based on presence of Ly-6G fluorescence. 10,000 Ly-6G<sup>+</sup> cells were acquired per sample.

#### *Y. pestis* supernatant preparation

*Y. pestis* KIM D27 or BS1 were inoculated from agar plates into 5 ml TMH (see recipe) and grown overnight at 26 °C with constant shaking. The next morning, bacterial cultures were diluted to OD600 0.2 in a final volume of 5 ml TMH. Cultures were grown for 1.5 h at 26 °C with constant shaking and then transferred to 37 °C for 3 h with constant shaking. Cultures were centrifuged for 5 min at 7500 rpm and culture supernatants were passed through 0.22  $\mu$ m syringe filters. Filtered supernatants were aliquoted and stored at -80 °C.

### Transwell chemotaxis assay

HL-60 cells were maintained at a cell concentration of less than  $1 \times 10^6$  cells/ml in IMDM supplemented with 20% HI-FBS. Cultures that exceeded a concentration of  $1 \times 10^6$  cells/ml were discarded. HL-60 cells were differentiated into neutrophil-like cells by resuspending cells to a concentration of  $2 \times 10^5$  cells/ml in IMDM supplemented with 20% FBS and 1.25% DMSO. Cultures were incubated for 6 days at 37 °C, 5% CO<sub>2</sub>. No medium changes were performed during the differentiation process. Cell differentiation was monitored by phase contrast microscopy, where differentiated cells were distinguished based on their smaller size and more polarized cell membrane when compared to standard HL-60 cells. Differentiated HL-60 cells were washed with 10 ml HBSS + 1% BSA and resuspended to a final cell concentration of  $2 \times 10^6$  cells/ml in HBSS + 1% BSA. 600 µl chemoattractant or medium control was added to the bottom chamber of a transwell plate with 5 µm insert membranes (Milipore Sigma). 100 µl differentiated HL-60 cells were added to the top chamber and incubated for 1h at 37 °C, 5% CO<sub>2</sub>. Transwell inserts were gently lifted and medium from the bottom chamber was used to rinse the bottom of the insert membrane. Transwell inserts were then discarded, and medium from the bottom well was transferred to round-bottom tubes for enumeration by flow cytometry.

### PRESTO-Tango assay

HTLA cells (kind gift from Dr. Gilad Barnea) were maintained in DMEM supplemented with 10% HI-FBS. For experimental assays, culture flasks were washed once with 15 ml PBS and cells were incubated for approximately 1 min with 5 ml Trypsin. Detached cells were mixed with 10 ml DMEM supplemented with 10% HI-FBS and

centrifuged for 5 min at 200 x g. Cell pellets were resuspended in culture medium and diluted to a concentration of  $2 \times 10^5$  cells/ml. 200  $\mu$ l of cells were added per well in a 96 well clear bottom, black wall tissue culture plate. The next day, 200 ng GPCR-tango plasmid per well was diluted to 20  $\mu$ l final volume in DMEM and mixed with 400 ng polyethylenimine (Polysciences) in 20  $\mu$ l DMEM (final volumes per well: 200 ng plasmid, 400 ng polyethylenimine, 40  $\mu$ l total volume). Plasmid/polyethylenimine mixtures were incubated for 20 min at room temperature. 40  $\mu$ l mixture was added to HTLA cells. After 16 - 24 h, the medium was replaced with 180  $\mu$ l DMEM + 10 mM HEPES, and 20  $\mu$ l GPCR stimulant or control was added to each well. After 24 h, 2.5  $\mu$ l Bright-Glo solution (Promega) was mixed with 47.5  $\mu$ l PBS + 20 mM HEPES per well, and 50  $\mu$ l Bright-Glo/PBS mixture was added to each well. Luminescence was quantified using a plate reader with a 10 sec pre-shake, 10 sec integration time, 0 sec settle time, and automatic attenuation.

#### Fluorescamine assay

85 ng PDF was added to 100  $\mu$ l of 1  $\mu$ M fMLF (Milipore Sigma) and brought to a final volume of 1 ml using PBS. PDF only, fMLF only, DMSO controls, and heat-inactivated PDF controls were all included. Samples were incubated for 1 h in a 37  $^{\circ}$ C water bath and transferred to a 70  $^{\circ}$ C heat block for 15 min. Once cooled to room temperature, transferred 100  $\mu$ l sample per well to a 96-well plate and added 50  $\mu$ l fluorescamine (3 mg/ml in DMSO; Milipore Sigma) per well. The plate was incubated for 15 min at room temperature and fluorescence measurements were made on a plate reader with an excitation wavelength of 390 nm and an emission wavelength of 485 nm.

## HPLC

HPLC was performed using a Shimadzu instrument with LCsolution software. Buffer A (HPLC-grade dH<sub>2</sub>O 1% TFA) and Buffer B (HPLC-grade acetonitrile 1% TFA) were connected to the corresponding pumps. 105 µl of each sample was transferred to HPLC-compatible glass vials and placed in the sample injection tray. Immediately after instrument startup, 10 µl dH<sub>2</sub>O was injected onto a ODS HYPERSIL C18 column (Thermo Scientific; Dim [mm] 250 x 4.6, particle size [µ] 3, part number 30103-254630). dH<sub>2</sub>O injections were repeated until absorbance spectra showed no significant peaks eluting from the column.

## Chapter 1: Generating FPR Knockout Mice

### Abstract

Knockout mice are an invaluable tool for unraveling the importance of host genes in responding to bacterial infections. Formyl peptide receptors (FPRs) are known to play an important role in innate immune responses to several bacterial infection models, yet few combinational FPR knockout mouse lines have been described in the literature. Here, we generate  $Fpr2^{-/-}$ ,  $Fpr3^{-/-}$ ,  $Fpr1/3^{-/-}$ , and  $Fpr1/2/3^{-/-}$  mice using a CRISPR-Cas9 embryo mutagenesis approach. These mice are indistinguishable from WT mice in breeding ability, average weight, and immune cell counts in the blood and spleen at homeostasis conditions.

### Introduction

*In vivo* bacterial infection studies focusing on the FPRs have been limited by the availability of transgenic mice with combinational FPR deletions. This is primarily due to the difficulty in creating gene deletions within a locus of linked genes, as  $Fpr1$ ,  $Fpr2$  and  $Fpr3$  reside in a genetic locus that is 150 kb in total length. This genetic distance is short enough to make it highly improbable to incur a recombination event within this locus and therefore makes it unfeasible to generate combinatorial FPR knockout mouse lines through breeding approaches. FPR knockout mouse lines generated by other research laboratories have relied on laborious and time-consuming *in vitro* mutagenesis techniques to generate novel mouse lines. The most common technique notably relies on embryonic stem cells derived from 129/sv mice, which carry the non-functional  $Fpr3$   $\Delta 4$  allele that differs from the functional  $Fpr3$  variant found in C57Bl/6 mice through the

loss of 4 amino acids in a transmembrane domain.<sup>39</sup> With the rise of efficient and affordable CRISPR-Cas9 mutagenesis techniques, novel mouse lines can now be generated more rapidly and in any mouse background of choice.

Previous research in our laboratory found that Fpr1<sup>-/-</sup> mice have enhanced resistance to *Y. pestis* infection.<sup>27</sup> To better understand the role of Fpr1, Fpr2, and Fpr3 in *Y. pestis* infection, we sought to generate mice lacking expression of Fpr1, Fpr2, or Fpr3 in various combinations. A key combination, Fpr1/2/3<sup>-/-</sup> mice that lack expression of all innate immune-expressed FPRs, to the best of our knowledge, have not been described in the literature. Fpr1/2/3<sup>-/-</sup> mice will be highly valuable to the research community to enable robust interrogation of the physiological relevance of FPR interactions during bacterial infections or other damage responses.

In this chapter, we describe a range of novel mouse lines, including Fpr2<sup>-/-</sup>, Fpr3<sup>-/-</sup>, Fpr1/3<sup>-/-</sup>, and Fpr1/2/3<sup>-/-</sup> mice. We confirm the genotype of these mouse lines using PCR and DNA sequencing. We also characterize the mice for their expression of key immune cell markers to ensure proper differentiation and maturation of critical cell types for infection response.

## Results

### CRISPR knockout approach generated 4 unique FPR knockout combinations

We utilized CRISPR-Cas9 for our targeted FPR knockout approach. To generate multiple FPR knockout combinations with a single embryo injection experiment, we injected fertilized embryos that were heterozygous at the Fpr1 allele with one allele derived from an Fpr1<sup>-/-</sup> male generated by Dr. Philip Murphy and one allele derived from

a WT C57Bl/6J female. These fertilized embryos were injected with complexed Cas9/gRNA, where two gRNAs targeted the Fpr2 promoter region and coding region, and two gRNAs targeted the Fpr3 coding region. With this approach, we sought to generate deletions in the Fpr2 translation start codon and RNA splice site to prevent transcript maturation and deletions in the Fpr3 coding sequence to generate a nonfunctional gene product. In this experiment, 9 embryos were injected and implanted into Swiss Webster females from which 7 founder pups were born. These founder pups were bred with WT or Fpr1<sup>-/-</sup> mice to produce the F1 generation (Figure 1.1). Mice born from the same founder parent were then bred again to produce the F2 generation (Figure 1.1). Mice of this generation were all genotyped by PCR to identify mice with homozygous deletions in Fpr2 and/or Fpr3 (Figure 1.2). Through this breeding scheme, we expected 25% of the F2 generation to be homozygous for the FPR loci inherited from the founder mice as dictated by classic Mendelian inheritance.

We generated 2 independent Fpr2<sup>-/-</sup> mouse lines, 2 independent Fpr3<sup>-/-</sup> mouse lines, 1 Fpr1/3<sup>-/-</sup> mouse line, and 1 Fpr1/2/3<sup>-/-</sup> mouse line. Genotypes were confirmed by amplifying deletion regions and sequencing these amplified products (Figure 1.2 – 1.7).

The Fpr2<sup>-/-</sup> mouse line derived from founder #323 contained a deletion from position 18,112,904 – 18,113,874 on Chromosome 17, which spans the translation start codon (Figure 1.3). This deleted region was replaced with a 138 bp insertion with no homology to the Fpr2 coding sequence. The new gene region does not contain any open reading frames with significant length and homology to retain Fpr2 function.

The Fpr3<sup>-/-</sup> mouse line derived from founder #327 contained a 649 bp deletion from position 18,190,871 – 18,191,520 on Chromosome 17 (Figure 1.4). This is an in-

frame deletion, but the resulting gene product lacks transmembrane domains 2 - 5 and has disruptions in transmembrane domains 1 and 6. This ensures loss of GPCR function.

The *Fpr3*<sup>-/-</sup> mouse line derived from founder #328 contains a 639 bp deletion from position 18,190,865 – 18,191,504 on Chromosome 17 (Figure 1.5). This deletion also disrupts transmembrane domains 1 – 6.

The *Fpr1/2/3*<sup>-/-</sup> mouse line derived from founder #327 contains a 181 bp deletion across the translation start codon for the *Fpr2* gene product from position 18,112,904 – 18,113,085 on Chromosome 17 (Figure 1.6) as well as a 573 bp deletion in the *Fpr3* coding region from position 18,190,936 – 18,191,509 on Chromosome 17 that disrupts transmembrane domains 1 – 6 (Figure 1.7).

The second *Fpr2*<sup>-/-</sup> mouse line and the *Fpr1/3*<sup>-/-</sup> mouse line, derived from founders #329 and #324, respectively, were analyzed for gene disruptions only by PCR. These disruptions were of similar PCR amplification size as the *Fpr2*<sup>-/-</sup> allele from founder #323 (Figure 1.8) and the *Fpr3*<sup>-/-</sup> alleles from founders #327 and #328 (Figure 1.9). We therefore conclude that these lines contain equivalent gene disruptions as the sequenced counterparts.

Having derived deletions in *Fpr2* and *Fpr3* from independent founder mice, we can broadly assess the CRISPR-Cas9 targeting efficiency of the 4 sgRNAs used in this study. For all *Fpr2*<sup>-/-</sup> alleles, we only observed deletions in the region immediately surrounding guide A. No deletions were observed in the region surrounding guide B, suggesting that guide B did not efficiently cleave at its target site. For all *Fpr3*<sup>-/-</sup> alleles, we observed highly efficient cutting by both guide C and guide D, as large deletions

were observed across all of these independently derived alleles spanning the genomic region between these guides.

#### The most widely used Fpr1<sup>-/-</sup> mouse line carries a non-functional Fpr3 allele variant

The most commonly used FPR knockout mouse lines come from the laboratory of Dr. Phillip Murphy. These knockout mouse lines were generated in 129/Sv embryos, which are known to carry the non-functional Fpr3  $\Delta 4$  allele.<sup>39</sup> Despite extensive backcrossing to mice of the C57Bl/6 background, the FPR locus is genetically linked and is therefore highly likely to remain linked through this backcrossing procedure. We PCR amplified and sequenced the Fpr3 alleles from this Fpr1<sup>-/-</sup> mouse line, and we confirmed that this mouse line is homozygous for the non-functional Fpr3  $\Delta 4$  allele (Figure 1.10). So despite being referred to as C57Bl/6 derivatives, these Fpr1<sup>-/-</sup> mice carry remnants of the 129/Sv background that may have important implications for studies of the immune system.

#### Basal immune cell counts and mouse weight averages are not impacted by loss of FPRs

Formyl Peptide Receptors have been previously implicated in cell maturation phenotypes.<sup>62,63,69</sup> To understand how FPR knockout combinations impact basal immune cell abundance at homeostasis, we collected blood and spleen samples from healthy mice of each genotype generated. We observed no significant changes in immune cell abundance across our mouse lines with only one exception, as detected by Ly-6G/Ly-6C (neutrophils), CD45 (B cells), CD8a (killer T cells), and CD4/CD11b

(helper T cells and dendritic cells) (Figure 1.11). Blood counts in the  $Fpr2^{-/-}$  mouse line were reduced to the point of reaching statistical significance. Despite this difference, the  $Fpr2^{-/-}$  mouse line had indistinguishable spleen cell counts when compared to other mouse lines.

As a final broad measure of mouse development, we weighed purchased C57Bl/6J mice, isogenic WT mice, and  $Fpr1/2/3^{-/-}$  mice to compare the average weights of male and female mice. We found no significant differences in these groups, suggesting that overall body mass is not impacted by FPR loss (Figure 1.12).

## **Discussion**

*In vivo* studies are crucial for understanding the physiological relevance of pathogenicity factors. Inbred mouse lines and new technological advances in genetic engineering have enabled sophisticated studies of individual host genes for controlling responses to bacterial infections. In this chapter, we report the generation of novel FPR knockout mouse lines. To the best of our knowledge, this is the first description of  $Fpr2^{-/-}$  mice (specifically containing an active  $Fpr3$  allele) and  $Fpr1/2/3^{-/-}$  mice. The addition of these mice to the research community will enable new studies into the function of FPRs in a variety of disciplines.

In this chapter, we report that all FPR knockout lines generated in our study are indistinguishable from WT C57Bl/6J mice, as measured through immune cell counts at homeostasis with the only exception being blood cell counts for  $Fpr2^{-/-}$  mice. Blood cell counts are commonly used to detect immune disorders like neutropenia in humans, where a 50% - 80% decrease in neutrophil counts are typically diagnosed as severe

immunodeficiencies.<sup>70</sup> *Fpr2*<sup>-/-</sup> mice had >50% reduction in Ly-6G, CD45, and CD8a counts when compared to WT mice (Figure 1.11). This may indicate an inherent immunodeficiency for *Fpr2*<sup>-/-</sup> mice, yet we would also expect an *Fpr2*-dependent development deficiency to also be observed in *Fpr1/2/3*<sup>-/-</sup> mice. Such a deficiency was not observed in *Fpr1/2/3*<sup>-/-</sup> mice (Figure 1.11). Further studies with larger group cohorts may clarify these data. These measures are important because of the wide role of activities that FPRs play not only in bacterial infection control but also in host development. Various laboratories have uncovered roles for FPRs in neural stem cell differentiation, mesenchymal stem cell differentiation, and tissue repair.<sup>62,63,69</sup> Given these roles in host development processes, some researchers hypothesized that an *Fpr1/2/3*<sup>-/-</sup> mouse would be non-viable. Indeed, our results show that *Fpr1/2/3*<sup>-/-</sup> mice are viable and appear to develop normally.

Given the role of FPRs in responding to bacterial formylated peptides, one might expect loss of FPRs to alter microbiome compositions. Although this particular topic has not been extensively studied, the role of *Fpr1* in mouse diabetes models has been undertaken. Research in this field found that *Fpr1*<sup>-/-</sup> mice maintained on a normal chow diet had similar gut microbiome diversity compared to WT mice, but microbiome diversity increased in *Fpr1*<sup>-/-</sup> mice fed a high-fat diet compared to WT mice on the same diet.<sup>71</sup> Such findings suggest that FPRs at homeostasis may not have a dramatic effect on microbiome composition. While we did not measure gut microbiome diversity in our FPR knockout mouse lines, we did observe similar weight averages for *Fpr1/2/3*<sup>-/-</sup> mice compared to the weight average of C57Bl/6J mice (Figure 1.12). Since gut microbiome imbalances can dramatically impact nutrient uptake and overall animal health, we

believe these weight averages suggest that the gut microbiome in our FPR knockout mouse lines has not changed to a significant enough degree to impact nutrient uptake and health.

With these newly generated mouse lines, we will explore the role of FPRs during *Yersinia pestis* and *Staphylococcus aureus* infection. We also hope that these mouse lines will continue to enable host-pathogen interaction studies as a resource for other research laboratories.

## Chapter 2: *In vivo* bacterial pathogenesis studies

### Abstract

Genetic deletion of Formyl Peptide Receptors renders mice more susceptible to a number of bacterial infections. Previous research in our lab found that mice lacking Fpr1 possess enhanced resistance to *Yersinia pestis* infection.<sup>27</sup> To further explore this result, we used a number of *in vivo* infection assays to assess the susceptibility of mice lacking Fpr1, Fpr2, Fpr3, or combinational Fpr1/2/3, to bubonic and pneumonic plague. We found that Fpr2<sup>-/-</sup> and Fpr3<sup>-/-</sup> mice had similar enhanced resistance to infection as Fpr1<sup>-/-</sup> mice. This resistance was not due to reduced dissemination of bacteria from the site of inoculation or to reduced T3SS injection of neutrophils.

### Introduction

*Yersinia pestis* infection occurs primarily through two routes. Intradermal infection, most often the result of bacterial inoculation via flea bite, causes bubonic plague. Aerosol or intranasal infection, commonly caused by the inhalation of contaminated droplets from plague patients, causes pneumonic plague. These two disease states are similar during early timepoints: *Yersinia* is inoculated into a patient, the temperature shift from the flea body temperature of 26 °C to the human body temperature of 37 °C induces virulence factor upregulation (most famously the Type III Secretion System), neutrophils and macrophages are recruited to the site of infection, and the *Yersinia* begin targeted killing of these innate immune cells.<sup>3</sup> During bubonic plague infection, the *Yersinia* then disseminates to the draining lymph node where it forms a replication niche.<sup>13</sup> From there, the bacteria will further disseminate and cause

death via organ failure approximately 7 days post-infection.<sup>3</sup> During pneumonic plague infection, the bacteria never disseminate from the lung but instead induce dramatic inflammation as a result of the targeted innate immune cell killing.<sup>12</sup> This inflammation leads to tissue necrosis of the lung alveolae and ultimately leads to death via compromised lung function within 3-4 days post-infection. In this way, both infections undergo similar host-pathogen interactions, yet they lead to significantly different outcomes and kinetics based on the initial site of infection.

*Staphylococcus aureus* is a gram-positive bacterial species that is clinically notable due to the emergence of methicillin-resistance *Staphylococcus aureus* (MRSA) subspecies. Unlike the relatively limited potential infection routes of *Y. pestis*, *S. aureus* can establish disease in most tissues, including the skin, bloodstream, kidney, liver, eyes, bones, and heart.<sup>72</sup> It has also been reported that approximately 30% of humans are carriers of *S. aureus* in the nasal cavity.<sup>73</sup> Further, patients with invasive *S. aureus* infections often carry the infecting *S. aureus* strain in the nasal cavity. In these cases, it is thought that the invasive infection may be seeded by the *S. aureus* bacteria colonizing the nasal cavity. During invasive infection, *S. aureus* undergoes several critical host-pathogen interactions with neutrophils to subvert the overall immune response and cause disease. Several of these interactions involve bacterial agonists and antagonists of FPRs.

In this chapter, we utilize our FPR knockout mouse lines to interrogate the functions of individual FPRs during *Y. pestis* and *S. aureus* infection.

## Results

### Loss of Formyl Peptide Receptors alters survival kinetics

A previous study from our laboratory found that *Fpr1*<sup>-/-</sup> mice had a delayed time-to-death compared to wildtype (WT) mice when infected subcutaneously in a bubonic plague disease model.<sup>27</sup> To identify the contributions, if any, to survival kinetics by the related innate immune receptors Formyl Peptide Receptor 2 (*Fpr2*) and Formyl Peptide Receptor 3 (*Fpr3*), we generated a number of FPR knockout mouse lines using CRISPR-Cas9 embryo mutagenesis in a C57Bl/6J background, as discussed in Chapter 1. With this approach, we isolated mouse lines with single deletions in *Fpr2* and *Fpr3* as well as combinational deletions in *Fpr1/3* and *Fpr1/2/3*. Notably, our *Fpr2*<sup>-/-</sup> mouse line is unique from other research groups because it was generated in a C57Bl/6J background, which contains an active *Fpr3* gene. The most commonly studied *Fpr2*<sup>-/-</sup> mouse line, in contrast, was generated in 129/Sv embryonic stem cells, which contain the non-functional *Fpr3*  $\Delta 4$  allele that is not surface expressed in innate immune cells.<sup>39</sup> Because the FPR genes are genetically linked, this previously reported *Fpr2*<sup>-/-</sup> line and a previously reported *Fpr1*<sup>-/-</sup> mouse line contain the non-functional *Fpr3*  $\Delta 4$  allele despite extensive backcrossing to C57Bl/6J mice, as detected by DNA sequencing (Figure 1.4).<sup>40,74</sup>

Early pilot experiments indicated that our previous laboratory stock of *Y. pestis* CO92 (stock R6-1-3) had become ‘freezer-attenuated’, as the LD50 dose of this stock was significantly higher than the typical *Y. pestis* CO92 LD50 of <10 CFU. To regain bacterial virulence, we passaged a freezer stock of *Y. pestis* CO92 two times through mice. Briefly, we infected mice with 1000 CFU *Y. pestis* CO92, euthanized mice at 72 hours post-infection (hpi), removed spleens, and plated homogenized spleen contents for

bacterial recovery. An LD50 experiment using a decreasing dose of the new *Y. pestis* CO92 stock BS1 showed that survival was dose-dependent and that lower CFU inocula experienced higher dissemination bottlenecks (Figure 2.1A), which is seen as a delayed time-to-death for low doses and is consistent with bottleneck reports from other laboratories.<sup>75</sup> Importantly, the calculated LD50 of *Y. pestis* CO92 stock BS1 is <10 CFU, indicating that full virulence was successfully restored. This strain was stored in multiple glycerol aliquots, and expression of the virulence-associated pigmentation locus was assessed prior to every mouse infection using a Congo Red agar dye approach.<sup>76</sup>

The generated FPR knockout mouse lines were infected subcutaneously with 600 CFU of the fully virulent *Y. pestis* CO92 stock BS1. The single *Fpr3*<sup>-/-</sup> but not *Fpr2*<sup>-/-</sup> mice achieved a statistically significant delay in time-to-death when compared to WT mice (Figure 2.1B). The combinational *Fpr1/2/3*<sup>-/-</sup> mice succumbed more rapidly to disease when compared to WT mice, but a statistical difference was only observed with the survival curve observed for the *Fpr2*<sup>-/-</sup> and *Fpr3*<sup>-/-</sup> mouse lines (Figure 2.1B). When the freezer-attenuated *Y. pestis* CO92 stock R6-1-3 was used in this same experimental setup, *Fpr1*<sup>-/-</sup> and *Fpr3*<sup>-/-</sup> survival curves were similar and displayed increased survival compared to WT mice (Figure 2.1C). These experiments suggest that *Fpr2*<sup>-/-</sup> and *Fpr3*<sup>-/-</sup> mice have similar enhanced resistance to bubonic plague disease as *Fpr1*<sup>-/-</sup> mice, yet loss of all innate immune-expressed FPRs appears to render mice more susceptible to infection.

To understand the contribution of infection route in bacterial pathogenesis during FPR knockout mouse infection, we infected mice intranasally with 1000 CFU *Y. pestis* CO92 stock BS1 in a pneumonic plague disease model. We found that *Fpr1/3*<sup>-/-</sup> mice had

a statistically significant enhancement in time-to-death when compared to Fpr2<sup>-/-</sup>, Fpr3<sup>-/-</sup>, and Fpr1/2/3<sup>-/-</sup> mice (Figure 2.1D). Fpr2<sup>-/-</sup> and Fpr3<sup>-/-</sup> mice closely mirrored the survival kinetics and final survival rate of WT mice. Owing to the high mortality rates, statistical differences were not observed nonetheless Fpr1/2/3<sup>-/-</sup> trended toward an enhancement in survival rate while Fpr1/3<sup>-/-</sup> mice trended toward a reduction in survival rate. Thus, Fpr2 appears to enhance mortality during pneumonic plague infection while Fpr1 and Fpr3 may reduce mortality. Regardless, the delayed time-to-death observed in the bubonic plague infection model is not observed in the pneumonic plague infection model, suggesting that the survival kinetics observed in FPR knockout mouse infection experiments is infection route-dependent and that results from one infection model may not predict the outcome observed using a different infection model. This result also suggests that the delayed time-to-death observed in the bubonic plague model but not pneumonic plague model is due to the effects of FPRs at dissemination sites where organ failure can occur and not at the site of inoculation, as pneumonic plague causes mortality before *Y. pestis* is able to disseminate to other organs.

#### *Y. pestis* disseminates to the spleen at a faster rate in mice lacking FPRs

To test if survival kinetics were due to changes in the rate of bacterial dissemination from the site of infection, we used the same subcutaneous bubonic plague model as above, but we euthanized mice at 48 hours post-infection (hpi) or 72 hpi, dissected their spleens, and plated homogenized organs for CFU enumeration. By enumerating CFU in the spleen, we are specifically measuring advanced stages of plague disease, as plague progresses from the dermis to the draining lymph node and then to the spleen.<sup>3</sup> We found

that at 48 hpi, a larger percentage of each FPR knockout mouse line had detectable levels of *Y. pestis* in the spleen compared to WT mice (Figure 2.2A). Of these groups, only Fpr1/2/3<sup>-/-</sup> mice had a statistically significant change in the percentage of mice with detectable CFU in the spleen compared to WT mice, as assessed by the chi-squared test (data not shown). By 72 hpi, nearly all mice had detectable CFU in the spleen (Figure 2.2B) These data suggest that *Y. pestis* disseminates from the site of inoculation to the spleen at a faster rate in mice lacking all FPRs when compared to WT mice. Mice lacking single FPRs also trend towards higher CFU detection percentages when compared to WT mice. This observation is consistent with a role of the FPRs in bacterial infection control by the innate immune system.

#### FPRs are dispensable for in vivo neutrophil recruitment using an IP *Y. pestis* infection model

Innate immune responses, and in particular neutrophil chemotaxis, towards infecting bacteria are commonly studied using an intraperitoneal (IP) infection model.<sup>41,77-80</sup> Mice were infected IP with 10<sup>8</sup> CFU *Y. pestis* KIM D27 and the total number of neutrophils (Ly-6G+) and bacterial CFU in IP lavage samples were measured after 3h of infection (Figure 2.3A/B). We observed no significant difference in the recruitment of Ly-6G+ cells or in the recovered bacterial CFU across our FPR knockout mouse lines. All mouse lines tested also reduced overall CFU by 10-100 fold, indicating an ability of these mice, regardless of FPR status, to kill *Y. pestis* (Figure 2.3B). Inoculating 10<sup>6</sup> or 10<sup>5</sup> CFU of *Y. pestis* did not reveal any differences in Ly-6G+ cell recruitment when comparing WT mice and Fpr1/2/3<sup>-/-</sup> mice (Figure 2.3C). To compare our experimental setup to previous

reports, isogenic WT mice were infected IP with  $5 \times 10^8$  CFU of *Staphylococcus aureus* USA300, and Ly-6G<sup>+</sup> cells were enumerated using the same method as above (Figure 2.5A). The total number of Ly-6G<sup>+</sup> cells recruited in this experiment was nearly identical to that observed by Weiss et al. 2017 using a similar inoculum of *S. aureus* USA300,<sup>41</sup> showing that our methodology is consistent with other research groups and reproducible. Overall, these experiments suggest that other redundant chemotaxis receptors can overcome the loss of one or more FPR *in vivo*.

#### Loss of Fpr1, but not Fpr2 or Fpr3, impacts T3SS injection of neutrophils *in vivo*

Our lab has previously reported a role for FPR1/mFpr1 in permitting injection of host cells by *Y. pestis* via the type III secretion system (T3SS).<sup>27</sup> To repeat these results, we used the identical U937 cell lines and *Y. pestis* KIM D27 freezer stocks for *in vitro* T3SS injection assays as had been used for this previous study. In this assay, the pMM83 plasmid is stably introduced into *Y. pestis* KIM D27. This plasmid constitutively expresses the T3SS effector protein YopM fused to beta-lactamase. This fusion protein is injected into host cells in a T3SS-dependent manner, thus loading the cytoplasm of injected cells with beta-lactamase. The reporter dye CCF2-AM can then be used to stain host cells. This molecule is composed of a coumarin derivative and fluorescein derivative connected by a beta-lactam ring. The intact molecule can be excited and undergo Forster resonant energy transfer (FRET) to emit light in the green spectrum. The molecule can also be cleaved by beta-lactamase to abolish the FRET activity and produce only light in the blue spectrum. In this way, cells successfully injected by *Y. pestis* can be detected and quantified by flow cytometry. We did not observe a defect in T3SS injection of FPR1<sup>-/-</sup>

U937 cells in three independent experiments (Figure 2.4A). Next, we performed an *ex vivo* T3SS injection experiment using isolated splenocytes from WT or Fpr1/2/3<sup>-/-</sup> mice. We observed no significant T3SS injection differences between these two groups, if at all, loss of all three genes may have promoted T3SS injection (Figure 2.4B). In this experiment, we use total splenocytes containing a mixture of cell types, keeping in mind that the overall immune cell composition between WT and Fpr1/2/3<sup>-/-</sup> mice is the same (Figure 1.5B). Given that T3SS injection by *Y. pestis* is critical for establishing infection and to better model *in vivo* infection, we tested the ability of *Y. pestis* to perform T3SS injection on Ly-6G<sup>+</sup> cells using an *in vivo* IP infection model with *Y. pestis* KIM D27 carrying the pMM83 plasmid as published previously.<sup>24</sup> We infected isogenic WT, Fpr1<sup>-/-</sup>, and Fpr1/2/3<sup>-/-</sup> mice with *Y. pestis* KIM D27 pMM83, counted 10,000 Ly-6G<sup>+</sup> cells by flow cytometry, and quantified the percentage of Ly-6G<sup>+</sup> cells that emitted blue fluorescence and represent the pool of cells injected with YopM-beta-lactamase (Figure 2.4C). Interestingly, Fpr1<sup>-/-</sup> mice appeared to separate into a bimodal distribution, where roughly half of the mice exhibited low T3SS injection while the other half exhibited high T3SS injection. The subset of Fpr1<sup>-/-</sup> mice with reduced T3SS injection is consistent with previously published data.<sup>27</sup> Fpr1/2/3<sup>-/-</sup> mice had a similar T3SS injection rate as WT mice. This suggests that Fpr2 and Fpr3 do not additively reduce the T3SS injection of neutrophils by *Y. pestis*, which is consistent with previous findings,<sup>27</sup> but it also suggests that the presence of Fpr2 and/or Fpr3 plays a role in shaping the bimodal T3SS injection distribution observed for Fpr1<sup>-/-</sup> mice.

### Characterizing *S. aureus* interactions with FPRs *in vivo*

To further test our novel mouse lines and to compare our results with *Y. pestis* to a well-characterized bacteria-FPR interaction, we used *S. aureus* USA300, a methicillin-resistant *S. aureus* (MRSA) isolate, for multiple infection studies. *S. aureus* is well known for its ability to activate FPRs with fMIFL<sup>81</sup> and PSMs<sup>41</sup> and antagonize FPRs with CHIPS,<sup>54</sup> FLIPr,<sup>49</sup> and FLIPr-like<sup>50</sup>.

Given the secretion of FPR agonists and antagonists by *S. aureus*, we sought to test the ability of neutrophils to migrate towards *S. aureus* USA300 in an IP infection model. We limited these experiments to *Fpr2*<sup>-/-</sup> and *Fpr1/2/3*<sup>-/-</sup> mice due to extensive previous literature on the role of *Fpr1* in chemotaxis towards *S. aureus*.<sup>49,50,54,82</sup> *Fpr1/2/3*<sup>-/-</sup> mice were used as a means to partially measure the role of *Fpr3* in this model. We found that neutrophils from isogenic WT mice had a nearly identical chemotaxis rate to that observed in a previous report<sup>41</sup> and similar killing capacity as reflected by the 10 – 100 fold reduction of the bacterial inoculum (Figure 2.5A/B). Interestingly, we observed that *Fpr2*<sup>-/-</sup> and *Fpr1/2/3*<sup>-/-</sup> mice both had enhanced chemotaxis towards *S. aureus* when compared to WT mice (Figure 2.5A). This is in stark contrast to a previous report that found *Fpr2*<sup>-/-</sup> mice to be deficient in chemotaxis to *S. aureus* using an identical IP infection model.<sup>41</sup> We hypothesize that this difference can be explained by the presence of a functional *Fpr3* in our *Fpr2*<sup>-/-</sup> mouse line while the previous report used an *Fpr2*<sup>-/-</sup> mouse line that carried the non-functional *Fpr3*  $\Delta 4$  allele. For further details, see the Discussion section of this chapter.

First, we performed a bloodstream infection by injecting mice intravenously via the retroorbital vein with  $5 \times 10^6$  CFU of USA300. 5 dpi, we dissected and homogenized

kidneys, plated samples, and quantified CFUs. We did not observe any significant differences in bacterial load when comparing our FPR knockout mouse lines to isogenic WT mice (Figure 2.5C). We do note that there is a large spread in recovered bacterial CFU across samples in this experiment. This can be explained by the lower inoculum used for infection. The lower inoculum was chosen with the anticipation that loss of FPR would result in hypersensitivity to infection. This is clearly not the case. Clearly, dissecting individual contributions of FPR genes in this model would require infecting animals with a range of bacterial inocula in groups of 10. Owing to the large number of animals that would be required for such a study, the experiment was not pursued.

*S. aureus* is a prolific colonizer of the human nares. Recent research efforts have identified two *S. aureus* strains, WU1<sup>83</sup> and JSNZ,<sup>84</sup> that naturally colonize mouse nares. Interestingly, the vomeronasal organ of mice (absent in humans) has high epithelial expression of Fpr3.<sup>35</sup> To test the role of FPRs in colonization, we inoculated *S. aureus* WU1 intranasally and monitored colonization by plating nasopharyngeal swabs and homogenized feces samples on a weekly basis. We found that Fpr1/2/3<sup>-/-</sup> and isogenic WT mice had similar levels of colonization through 28 days post-inoculation (Figure 2.6A/B).

## **Discussion**

Animal infection models are powerful tools for interrogating host-pathogen interactions in the most complete environment possible. In this chapter, we sought to compare the role of Fpr2 and Fpr3 in *Y. pestis* infection to the role of Fpr1, which had been previously characterized by our laboratory.<sup>27</sup> We began with the observation that

the freezer stocks of *Y. pestis* CO92 strain R6-1-3 that had been used in the previous study had a higher LD50 than is typical for *Y. pestis* CO92 (<1 CFU for WT CO92) (Figure 2.1C). Such a decrease in virulence could be problematic for our studies because it indicates a change in genetic or epigenetic markers for this freezer strain compared to WT CO92. This is not unusual for highly virulent strains that are passaged under laboratory conditions. Given that we did not know how this change could have impacted interactions with FPRs or readouts from our experiments (e.g. dissemination kinetics), we decided to address this deficiency by passaging a freezer stock of *Y. pestis* CO92 derived directly from the Biodefense and Emerging Infections Research Resources Repository (BEI) through mice twice to ensure full strain virulence. Mice in the first round of infections showed disease symptoms within 48 hpi, indicating that this stock had maintained high virulence. This original stock from BEI had been stored in glycerol since 2006 while our R6-1-3 stock was stored in BSA/MSG for less than 3 years. The resulting isolated strain, termed BS1, had an LD50 of <1 CFU (Figure 2.1A). This strain was used for all subsequent *Y. pestis* CO92 experiments. These results imply that glycerol storage conditions are preferable to BSA/MSG for long-term *Y. pestis* storage.

Given the enhancement in the survival of *Fpr1*<sup>-/-</sup> mice to *Y. pestis* infection when compared to WT mice, we first sought to characterize the survival effects of *Fpr2* and *Fpr3* mutations, as well as FPR combinational mutations, in a bubonic infection model (Figure 2.1B/C) and a pneumonic infection model (Figure 2.1D). Surprisingly, we found that *Fpr3*<sup>-/-</sup> mice had an enhanced survival to bubonic plague infection when compared to WT mice, and *Fpr2*<sup>-/-</sup> mice trended towards a similar enhanced survival as well (Figure 2.1B/C). This result is particularly surprising because previous studies in our lab found a

role for Fpr1, but not Fpr2 or Fpr3, in mediating T3SS injection interactions between *Y. pestis* and innate immune cells.<sup>27</sup> This previous report concluded that mediation of this T3SS interaction could explain the enhanced survival of Fpr1<sup>-/-</sup> mice to plague infection, yet we find a nearly identical survival phenotype for Fpr3<sup>-/-</sup> mice using the same freezer stocks of *Y. pestis* CO92 R6-1-3 as this previous study. This suggests either that Fpr1 and Fpr3 play the same role in the infection process and that this role is T3SS-independent or that Fpr3 plays a different role in infection than Fpr1 and the similar survival phenotype is coincidental. Regardless, the enhanced survival of Fpr2<sup>-/-</sup> and Fpr3<sup>-/-</sup> mice to *Y. pestis* infection remains unique and unexpected when compared to the effect of FPR knockouts in other bacterial infection models.<sup>29,31,40</sup>

To understand if the survival effects of FPR knockout mice during *Y. pestis* were infection route-dependent, we assessed the survival of our FPR knockout mouse lines during a pneumonic plague infection model (Figure 2.1D). In this model, we observed similar time-to-death kinetics for all mouse lines except for Fpr1/3<sup>-/-</sup> mice, which had a statistically significant increase in time-to-death when compared to Fpr2<sup>-/-</sup>, Fpr3<sup>-/-</sup>, and Fpr1/2/3<sup>-/-</sup> mice. While there were minor changes in survival percentage between the mouse lines tested, we did not observe statistically significant changes when comparing Fpr2<sup>-/-</sup>, Fpr3<sup>-/-</sup>, or Fpr1/2/3<sup>-/-</sup> mice to isogenic WT mice. These results are interesting because of the importance of inflammation in driving pneumonic plague progression. Pneumonic plague is characterized by massive inflammation within 2 dpi, which leads to rapid tissue destruction and mortality.<sup>12</sup> Here, we see that FPR knockout mice have similar survival rates to WT mice, and more importantly, that the time-to-death for FPR knockout mice is the same as that for WT mice. This indicates that loss of FPRs does not

reduce innate immune cell influx to the degree necessary to prolong survival. Interestingly though, we do observe a statistically significant increase in time-to-death for Fpr1/3<sup>-/-</sup> mice. This is in stark contrast to Fpr1/2/3<sup>-/-</sup> mice that may survive at a higher rate compared to WT mice. This result implies that Fpr2 is a major driver of inflammation and that Fpr1 and/or Fpr3 are potentially playing anti-inflammatory roles during pneumonic plague infection. Such anti-inflammatory roles have been described for Fpr1 during allergy responses, so this role has been described previously in the literature.<sup>59</sup> A role for Fpr2 in promoting inflammation has been observed during allergy responses in the lung<sup>74</sup> and during neutrophil swarming in response to tissue damage.<sup>60</sup>

*Y. pestis* dissemination from the site of inoculation in the dermis to the draining lymph node and beyond remains elusive. While many researchers argue that plague bacteria form productive reproductive niches within innate immune cells which then home to the draining lymph node, other researchers argue for an extracellular bacterial diffusion mechanism to the draining lymph node, as *Y. pestis* lacks flagella.<sup>20</sup> These two models are not mutually exclusive, but the role of innate immune cells at the site of inoculation would play countering roles in these two models. In the cell-mediated dissemination mechanism, recruitment of innate immune cells would be required for dissemination of bacteria to the draining lymph node. In the extracellular bacteria diffusion model, recruitment of innate immune cells would be expected to slow bacterial dissemination by killing a portion of the inoculated bacterial population. In this study, we found that more mice in all of the FPR knockout mouse lines tested had detectable CFU of *Y. pestis* in the spleen at 48 hpi when compared to isogenic WT mice (Figure 2.2A). This finding suggests that *Y. pestis* disseminates from the site of inoculation more rapidly in Fpr2<sup>-/-</sup>, Fpr3<sup>-/-</sup>,

Fpr1/2/3<sup>-/-</sup>, and Fpr1/3<sup>-/-</sup> mice. Given the known role for FPRs as drivers of chemotaxis, this result is most compatible with a model whereby single or combinational FPR knockout mice have reduced innate immune cell recruitment to the site of bacterial inoculation which allows for more rapid extracellular bacterial dissemination by reducing the number of bacteria killed by neutrophils. Our results are therefore most consistent with the bacterial diffusion model for reaching the draining lymph node.

We tested this immune cell recruitment hypothesis by performing *in vivo* neutrophil recruitment assays with our array of FPR knockout mouse lines (Figure 2.3A-C). We chose to explore *in vivo* chemotaxis as a means for providing as many physiologically-relevant chemotaxis cues as possible, which can include complement cues and chemokine cues. We explore FPR-dependent chemotaxis using an *in vitro* assay in Chapter 3. Our *in vivo* chemotaxis results revealed no significant differences in Ly-6G<sup>+</sup> (*i.e.* neutrophil) cell recruitment towards *Y. pestis* KIM D27 across our various mouse lines. This remained true for bacterial inocula ranging from 10<sup>8</sup> CFU – 10<sup>5</sup> CFU (Figure 2.3C). Inocula of 10<sup>4</sup> CFU and below failed to recruit significant numbers of Ly-6G<sup>+</sup> cells (data not shown). These results suggest that Fpr1, Fpr2, and Fpr3 do not play a significant role during *in vivo* neutrophil recruitment to *Y. pestis*. This implies that alternative chemotaxis receptors, like complement receptors and chemokine receptors, largely drive chemotaxis in this experimental setup. One major caveat of these results, however, is that these recruitment assays were performed using an IP infection model. This model is widely used in the literature to study chemotaxis toward various bacterial species.<sup>41,77–80</sup> But, *Y. pestis* does not naturally infect the IP cavity, and the IP cavity has significantly more void space than solid tissues like the dermis. A larger void space may impact the

length of time where a chemoattractant gradient remains intact, so one might expect that a chemoattractant gradient would remain intact for longer in a solid tissue when compared to the IP cavity. Since FPR-dependent chemotaxis is driven by formyl peptide gradients, it is possible that an FPR-dependent chemotaxis phenotype in response to *Y. pestis* would be observed in a dermal infection model while being absent in an IP infection model. This experiment would be highly informative, yet dermal infection assays are technically challenging and lack data in the literature with which we can compare results.

The *in vivo* chemotaxis assay also afforded us the opportunity to simultaneously measure the killing capacity of recruited neutrophils by measuring the concentration of bacterial CFU recovered in the IP lavage samples. We found a consistent 10 – 100 fold reduction in bacterial CFU for all mouse lines tested (Figure 2.3B). We interpret this as an indication of sustained anti-bacterial activity by recruited neutrophils and other immune cells, as we would expect to recover bacterial CFU near the inoculum value if an anti-bacterial activity was not occurring in one of our FPR knockout mouse lines. A previous report has found a direct role for FPRs in inducing bacterial phagocytosis, yet our results show no reduction in bacterial clearance capacity for our mouse lines and therefore argue against this mechanism occurring during plague infection.<sup>85</sup> The reduction in bacterial CFU could also be explained by strong bacterial adhesion to surfaces within the IP cavity, as *Y. pestis* expresses the F1 pilus during infection of mammalian hosts, which is thermoregulated by the transcription factor *Caf1R* and has anti-phagocytic activity.<sup>86</sup> We believe that our experimental technique makes this possibility unlikely because we perform an extended (2 min) shaking step while washing the IP cavity to ensure that

recovered IP lavage samples are well mixed and representative of the entire contents of the cavity.

Although our *in vivo* T3SS injection results were somewhat consistent with previous data generated in our lab, a few key details of these results remain unclear. First, the bimodal distribution for Fpr1<sup>-/-</sup> mice was unexpected. The decreased T3SS injection of half of the sample population was expected based on previous data, as this is consistent with the role of Fpr1 as a mediator of T3SS injection as a receptor or through other functions. The high injection sample population, which is injected at a higher rate than WT mice, cannot be easily explained by the receptor hypothesis. Regardless, the bimodal distribution in the *in vivo* experimental setup may hint that there is an unknown dynamic in this system that leads to high or low injection of FPR1<sup>-/-</sup> cells. This could be an explanation for why we were unable to reproduce the *in vitro* results previously published by our lab, as a minor change in culture reagents or technique could trigger this dynamic element to bias in one way or the other. Second, we cannot explain why Fpr1/2/3<sup>-/-</sup> neutrophils are injected at rates comparable to WT mice while Fpr1<sup>-/-</sup> mice exhibit a bimodal distribution. As discussed previously, the Fpr1<sup>-/-</sup> mouse line being used carries a non-functional Fpr3 allele, which makes this mouse line Fpr1/3<sup>-/-</sup>. This shift in injection percentage of Fpr1/2/3<sup>-/-</sup> neutrophils towards a WT phenotype may therefore be linked to the loss of Fpr2. Activation of Fpr2 by the host pro-resolution protein Annexin A1 has been shown to reduce inflammation during *S. pneumoniae* infection primarily by upregulating macrophage phagocytosis and reducing neutrophil infiltration into the lungs.<sup>87</sup> A super-resolution imaging study has previously shown that *Y. pestis* T3SS is upregulated during phagocytosis, which is mainly driven by the formation of extra T3SS

injectisomes along the walls of the phagocytic cup in the early stages of phagocytosis.<sup>88</sup> These two activities could be synergistic: activation of Fpr2 by Annexin A1 could upregulate phagocytosis and therefore increase T3SS into innate immune cells. Fpr2 activation can also reduce T3SS through the downregulation of neutrophil recruitment as a response to Annexin A1 activation. These competing activities might be one possibility to explain the bimodal distribution for T3SS injection of Fpr1<sup>-/-</sup> mouse neutrophils that is absent in Fpr1/2/3<sup>-/-</sup> mouse neutrophils. This may also help explain our difficulty in reproducing *in vitro* T3SS results, as human serum contains detectable levels of Annexin A1.<sup>89</sup> It may also be possible that different lots of fetal bovine serum used in U937 cell propagation could also contain Annexin A1 and that this concentration may vary from lot to lot. Further studies will be necessary to uncover the exact mechanism behind the T3SS phenotypes identified *in vivo* and *in vitro*.

*S. aureus* interacts with FPRs with both agonists and antagonists, which makes it a particularly interesting case in the study of bacteria-FPR interactions. Despite this abundance of FPR-modulating interactions, we did not observe a difference in bacterial colonization (Figure 2.6 A/B) or pathogenesis (Figure 2.5C), as measured by CFU burden in the kidney. We did, however, observe a heightened recruitment of neutrophils to *S. aureus* with an *in vivo* chemotaxis model in Fpr2<sup>-/-</sup> and Fpr1/2/3<sup>-/-</sup> mice when compared to isogenic WT mice (Figure 2.5A). Previous reports indicated a reduction in neutrophil recruitment to *S. aureus* in Fpr2<sup>-/-</sup> mice, which was attributed to the release of formylated PSMs.<sup>41</sup> We hypothesize that this result is due to differential activity of Fpr3, as our Fpr2<sup>-/-</sup> mouse line carries an intact Fpr3 allele while the previous report utilized the Fpr2<sup>-/-</sup> mouse line generated by the laboratory of Dr. Philip Murphy that carries the non-functional

Fpr3  $\Delta$ 4 allele (see introduction for more detail). The *S. aureus* USA300 strain used by us and this previous report secretes an FPR1 agonist (fMIFL<sup>81</sup>), FPR2 agonists (formylated PSMs<sup>41</sup>), an FPR1 antagonist (CHIPS<sup>54</sup>) and an FPR2 antagonist (FLIPr<sup>49,50</sup>). It should be noted that formylated PSMs have also been claimed by other groups to activate FPR2 through a binding site that biases signaling away from chemotaxis<sup>90</sup> and so chemotaxis driven by FPR2 may not be PSM-dependent. We propose that in an *in vivo* context, the activity of the FPR antagonists CHIPS and FLIPr (or FLIPr-like in some *S. aureus* strains<sup>50</sup>) play a dominant role to FPR agonists. In this way, by knocking out Fpr2 in our mouse line, we abolished an inhibitory chemotaxis interaction. This, therefore, results in increased chemotaxis. We propose that the previous study observed a reduction in chemotaxis because the mouse line lacked both Fpr2 and Fpr3 leaving only Fpr1, which is potently antagonized by CHIPS. We hypothesize that in our Fpr2<sup>-/-</sup> mouse line, we retain chemotaxis activity through activation of Fpr3 by bacterial factors and/or host factors.

## Chapter 3: Characterizing FPR activation by *Yersinia pestis*

### Abstract

Activation of Formyl Peptide Receptors by bacterial ligands is widely recognized as an important host-pathogen interaction, yet, to the best of our knowledge, *Y. pestis* has not been studied in this context. Here, we used a number of biochemical and reporter assays to characterize FPR agonists produced by *Y. pestis*. We found that *Y. pestis* produces multiple formylated peptides that can activate Fpr1 but not Fpr2 or Fpr3. Taken together with Chapter 2, these results imply a role for Fpr2 and Fpr3 in responding to host-derived cues while activation of Fpr1 by bacterial products may promote disease progression by modulating cytokine production and guiding immune cells towards bacterial T3SS killing traps.

### Introduction

Interactions between bacteria and innate immune cells via the formyl peptide receptors represent an ongoing host-pathogen interaction with active evolutionary pressures to adapt on both sides. In the previous chapter, we found that loss of Fpr1, Fpr2, or Fpr3 impacts host survival during bubonic plague infection, yet *in vivo* chemotaxis assays revealed no difference in neutrophil recruitment to *Y. pestis*. In this chapter, we use a combination of *in vitro* chemotaxis assays, PRESTO-Tango reporter assays, and biochemical assays to characterize the ability of *Y. pestis* to activate Fpr1, Fpr2, and Fpr3 derived from both mice and humans. We also utilize *S. aureus* as a well-characterized control for our PRESTO-Tango reporter assays.

## Results

### Fpr1, but not Fpr2 or Fpr3, is directly activated by *Y. pestis* molecules

We used PRESTO-Tango technology<sup>58</sup> to interrogate activation of the human and mouse innate immune FPRs by cloning mFpr1, mFpr2, mFpr3, and mFpr3  $\Delta$ 4 into the PRESTO-Tango plasmid backbone. This assay allows for the individual interrogation of GPCR activation by transfecting HTLA cells (derivatives of HEK293-T cells; kind gift of Dr. Gilad Barnea) with a plasmid that can express a GPCR with a modified C-terminal tail. Activation of the expressed GPCR can be quantified via luminescence detection with a plate reader.<sup>58</sup> Using this assay, mFpr1 was robustly activated by *Y. pestis* supernatant as well as the Fpr1 activator fMLF, but no activity was observed for mFpr2, mFpr3, or mFpr3  $\Delta$ 4 (Figure 3.1A-D). Activation by fMLF was notably dose-dependent, indicating that this assay is capable of detecting ligand concentration differences. Human FPR1 was also activated by *Y. pestis* supernatant but not human FPR2 or FPR3 (Figure 3.1E-G). To reduce the effect of cell lysis on the composition of supernatant samples, we used refreshed overnight cultures grown for 1.5h at 26C and 3h at 37C to reach the exponential bacterial growth phase and induce expression of temperature-regulated virulence genes. Refreshed overnight cultures at t = 0h were capable of activating Fpr1 as expected (Figure 3.1H). Supernatant samples at the end of the growth phase (t = 4.5h) reached significantly higher activation levels than the t = 0h samples, indicating that the majority of the Fpr1 activating molecules are being produced during the growth phase and are not simply being carried over from the overnight culture (Figure 3.1H).

To further confirm the specificity of the PRESTO-Tango system and to test the activation of FPR2 and FPR3 broadly, we used supernatant derived from overnight

*Staphylococcus aureus* USA300 cultures in the same experimental setup as described above. *S. aureus* supernatant activated hFPR1 and hFPR2 but not hFPR3 (Figure 3.2A-C). This is consistent with the known FPR agonists produced by *S. aureus*: fMIFL activates hFPR1<sup>81</sup> and formylated phenol soluble modulins (PSMs) activate hFPR2.<sup>41</sup> There is no known hFPR3 agonist produced by *S. aureus*.

#### Neutrophils and neutrophil-like cells chemotax towards *Y. pestis*

A transwell chemotaxis assay was used to quantify the migration of human neutrophil-like HL-60 cells to various chemoattractants. These cells migrated to the FPR1 agonist fMLF and to live *Y. pestis* KIM D27 (Figure 3.3A). The response to KIM D27 was dose-dependent, as migration decreased with decreasing dose (Figure 3.3A). HL-60 cells also migrated robustly to multiple dilutions of cell-free *Y. pestis* KIM D27 culture supernatant, indicating that the chemoattractant produced by *Y. pestis* is secreted (Figure 3.3B).

To test the role of FPR1 in chemotaxis towards *Y. pestis*, we compared the migration of WT HL-60 cells and FPR1<sup>-/-</sup> HL-60 cells. WT HL-60 cells migrated towards the FPR1 activator fMLF, the BLT1 activator Leukotriene B4 (LTB4), and cell-free supernatant from *Y. pestis* KIM D27 (Figure 3.3C). Fpr1<sup>-/-</sup> HL-60 cells did not significantly respond to fMLF or *Y. pestis* supernatant, indicating that the majority of the chemotactic response towards *Y. pestis* supernatant is driven by Fpr1 (Figure 3.3D).

Using an *ex vivo* transwell chemotaxis assay, we assessed the chemotactic response of thioglycolate-elicited granulocytes derived from isogenic WT mice and from Fpr1/2/3<sup>-/-</sup> mice. We found that WT granulocytes were capable of robust migration

towards LTB<sub>4</sub> and *Y. pestis* supernatant (Figure 3.3E) while Fpr1/2/3<sup>-/-</sup> granulocytes had stunted migration toward bacterial supernatant when compared to migration toward LTB<sub>4</sub> (Figure 3.3F). These results confirm that FPRs play an active role in the chemotaxis of mouse granulocytes toward *Y. pestis*-derived ligands, yet FPR-deficient granulocytes do retain a moderate level of migratory activity thus implicating other chemotactic receptors in chemotaxis responses to bacterial-derived ligands.

#### LcrV is not an Fpr1 agonist

A previous report has shown that the *Y. pestis* T3SS needle tip protein LcrV can block neutrophil chemotaxis both *in vivo* and *in vitro*.<sup>91</sup> Using our differentiated HL-60 *in vitro* chemotaxis assay, we found that LcrV is not capable of inducing chemotaxis above background levels of mock-treated samples (Figure 3.4A). Cells that were exposed to fMLF and LcrV simultaneously did not show reduced chemotaxis, as would be expected if LcrV was antagonizing FPR1 (Figure 3.4B). We therefore conclude that LcrV alone does not induce HL-60 chemotaxis and that, at tested concentrations, LcrV does not act as an antagonist of FPR1. We should note that we used recombinant LcrV for these experiments. LcrV secreted by *Y. pestis* during infection may adopt a conformation that is not captured in the recombinant protein.

#### The primary Fpr1 agonist(s) is a small N-terminally formylated protein

Fpr1 is well known to respond robustly to formylated peptides. We attempted to create a *Y. pestis* strain with a genomic deletion for the formyl methionyltransferase (*fmt*) gene, which formylates tRNA-Methionine to produce the pool of formyl-methionine-

charged tRNAs used in bacterial translation initiation.<sup>92</sup> This gene deletion was unsuccessful, suggesting that *fmt* may be an essential gene in *Y. pestis* (data not shown). In an alternative approach, we expressed and purified *Y. pestis* peptide deformylase (PDF) in *E. coli* BL21 (DE3). This enzyme catalyzes the derformylation of formylated proteins and is broadly conserved across prokaryotes.<sup>93</sup> A fluorescamine assay indicated that *Y. pestis* PDF was able to convert formyl-methionine into NH<sub>2</sub>-methionine via the increase in fluorescence intensity of fMLF incubated with PDF, as fluorescamine only becomes fluorescent when it covalently binds to primary amines<sup>94</sup> (Figure 3.5A). Deformylation was further confirmed through a functional PRESTO-Tango assay, where PDF-treated fMLF lost the ability to activate hFPR1 (Figure 3.5B).

*Y. pestis* cell-free supernatants incubated overnight with PDF showed a reduced, but not fully ablated, ability to activate mFpr1 via PRESTO-Tango (Figure 3.5C). HL-60 chemotaxis assays using WT or FPR1<sup>-/-</sup> HL-60 cells both showed a reduction in cell chemotaxis towards PDF-treated *Y. pestis* supernatant samples (Figure 3.6A/B). Taken together, these data indicate that one or more formylated proteins activate neutrophils primarily through Fpr1, although we do note that a PDF-resistant agonist may also be present in culture supernatants.

To better characterize the secretion characteristics of the mFpr1 agonist, we tested the mFpr1 activating potential of *Y. pestis* KIM D27 and CO92 BS1 grown at 26C (flea body temperature), 37C (human body temperature; activates T3SS expression<sup>26</sup>), and in the presence or absence of calcium (37C without calcium induces T3SS secretion<sup>26</sup>). Each of these growth conditions activated mFpr1 to similar levels in *Y. pestis* KIM D27 and *Y. pestis* CO92 BS1 strains (Figure 3.7A/B). Likewise, when *Y. pestis* CO92 ΔpCD1

strains with transposon insertions in specialized secretion machineries were tested, each mutant retained the ability to activate mFpr1 (Figure 3.7C). Taken together, these data suggest that the mFpr1 agonist is constitutively released by *Y. pestis* through either general secretion pathways or through passive mechanisms.

Additional treatments were used on *Y. pestis* supernatants to better characterize the mFpr1 activating molecule(s) with PRESTO-Tango. Treatment with Proteinase K abolished mFpr1 activation, thus confirming that the primary mFpr1 agonist(s) in *Y. pestis* supernatant is proteinaceous (Figure 3.7D). Boiling the supernatant at 95C did not impact mFpr1 activation, suggesting that mFpr1 activation is not dependent on a folded protein (Figure 3.7E). Molecular weight cut-off (MWCO) filtration experiments showed that the mFpr1 agonist can be found on both sides of a 3kDa MWCO filter but flows through a 10kDa MWCO filter, indicating a size range of less than 10kDa (Figure 3.7F).

#### C18 HPLC reveals multiple formylated peptide agonists in *Y. pestis* supernatant

Further biochemical characterization of the Fpr1 agonist(s) produced by *Y. pestis* was performed using High Performance Liquid Chromatography (HPLC) and matrix-assisted laser desorption/ionization-time of flight (MALDI-ToF) mass spectrometry. For HPLC, 100  $\mu$ l *Y. pestis* supernatant was injected onto a C18 column and fractions were collected in 500  $\mu$ l volumes. Fractions were combined into 4 pools, concentrated by solvent evaporation with a SpeedVac, and used for Fpr1 activation experiments via PRESTO-Tango. We found that only Pool 4 activated Fpr1 (Figure 3.8A). When PDF-treated supernatant was used for the same experiment, Pool 4 had a reduction in Fpr1 activation (Figure 3.8B). We next took the fractions that composed Pool 4 and pooled

adjacent fractions so that all even fractions had been combined with the preceding odd fraction in an attempt to identify specific fractions with agonist activity for Fpr1. We found that a subset of fractions was capable of Fpr1 activation when derived from WT supernatant but not from PDF-treated supernatant, indicating that the Fpr1 agonist can be separated by C18 HPLC and that there are likely multiple unique formylated peptide agonists released by *Y. pestis* that have similar yet distinct hydrophobicity properties (Figure 3.8C). These fractions include 73, 75, 77, 79, 85, 89, and 93. A subset of these activating fractions were further concentrated and subjected to MALDI-TOF, yet the peptide concentration remained too low to acquire quality data using this method.

## Discussion

Few bacterial peptides with agonistic properties against formyl peptide receptors have been characterized to date. While it is well known that formylated peptides are the primary ligands for FPRs, it remains difficult to predict FPR agonists due to a lack of protein sequence knowledge. This level of protein identification is challenging to achieve, but, in the absence of protein sequence knowledge, it remains important to biochemically characterize bacterial interactions with FPRs due to their presumed importance in early innate immune responses to bacterial infections. In this study, we sought to robustly characterize *Y. pestis* interactions with FPRs to uncover any additional roles for FPRs during plague infection outside of the previously described role in mediating T3SS interactions with innate immune cells.<sup>27</sup> Although we were not successful in identifying exact peptide agonists of FPRs produced by *Y. pestis*, we did

succeed in biochemically narrowing down the agonist to most likely multiple peptides that maintain N-terminal formyl modifications.

Our study revealed interesting insights into interactions that may play important roles during the infection process. We found that only Fpr1 in both mice and humans is activated by non-sedimentable *Y. pestis* culture products while Fpr2 and Fpr3 are not activated (Figure 3.1A-G). This has a number of important implications. First, activation of Fpr1 implies its role as a chemoreceptor for innate immune cells to recruit to sites of *Y. pestis* infection. While we have shown that loss of Fpr1 impacts *in vitro* chemotaxis (Figure 3.3C-F), we failed to observe an impact on neutrophil recruitment to *Y. pestis* IP infections *in vivo* in Chapter 2 (Figure 2.3A). This leaves two possibilities: Fpr1 plays a subtle role in neutrophil recruitment that cannot be discerned in the IP infection model, or Fpr1 is dispensable for *in vivo* neutrophil recruitment entirely. Our data is more compatible with the first scenario given our *in vitro* chemotaxis assay results, but the second scenario cannot be ruled out entirely.

Second, the lack of activation of Fpr2 and Fpr3 implies that their role in enhancing survival in experiments performed in Chapter 2 is independent of bacterial agonists. This could mean that Fpr2 and Fpr3 are responding to host-derived peptides, possibly as a participant in the neutrophil swarming response,<sup>60</sup> or they are driving a bacterial interaction (such as cell adhesion) that does not require receptor activation. A final possibility is that *Y. pestis* products do activate Fpr2 and/or Fpr3 but that the resulting signaling pathway biases away from the beta-arrestin recruitment pathway. This is a possibility because our PRESTO-Tango assay for measuring GPCR activation relies on beta-arrestin recruitment to trigger a signaling cascade that results in

luciferase production, so an agonist that avoids beta-arrestin recruitment would not be detected as a GPCR agonist in this assay. Such biased agonists have been described in previous reports, one of which was recently generated through intentional screening efforts to prevent receptor desensitization and enhance the therapeutic effect of a GPCR agonist.<sup>95</sup> Although this possibility cannot be ruled out, we argue that it is unlikely given that all FPR knockout mice retained the ability to clear *Y. pestis* (Figure 2.3B), and we would expect an FPR agonist that does not induce cell chemotaxis to preferentially induce bactericidal effects through binding to a low-affinity site like that observed for fMLF with FPR1.<sup>34</sup>

Third, activation of Fpr1 may be responsible for altering the production of immune system modulators like cytokines and chemokines, as suggested by previous studies.<sup>59</sup> This is in agreement with observations suggesting that *Y. pestis* infections lack robust production of inflammation mediators during the early stages of infection in the lymph node<sup>10</sup> and lung.<sup>12</sup>

LcrV has been a target of significant research interest due to its proposed activity as an antagonist of chemotaxis,<sup>91</sup> activator of TLR2<sup>96</sup> (which has since been debunked as physiologically irrelevant<sup>97</sup>), and driver of T3SS. We were surprised to find a lack of activity for LcrV in our chemotaxis assay, as we had expected to observe an antagonism role similar to previous studies.<sup>91</sup> Although this result appears contradictory to previous studies, we believe that it may be explained by minor differences in experimental procedure. These previous *in vitro* chemotaxis studies pre-incubated neutrophils with LcrV before exposing the cells to a gradient of fMLF.<sup>91</sup> Our experiments looked at the effect of simultaneous LcrV and fMLF gradients on neutrophil-like HL-60

chemotaxis. One explanation for the contrasting results from these two experimental assays could be that LcrV is capable of binding to FPR1 but that this binding is low affinity and therefore requires extended pre-incubation to induce an antagonistic effect. Binding to FPR1 has been observed in our laboratory previously using co-immunoprecipitation methods,<sup>27</sup> but these experiments do not imply a strong or weak binding affinity. Although our *in vitro* results and our *in vivo* chemotaxis results from Chapter 2 show no role for LcrV in FPR1-dependent chemotaxis and activation of FPR1/mFpr1 occurs in the absence of the T3SS (Figure 3.7A/B/C), further in-depth studies would be needed to confidently determine the physiological relevance of any LcrV-FPR1 interactions.

Despite being unable to determine the exact peptides driving FPR1 activation in *Y. pestis* supernatants, we did find that no single secretion pathway, tested using transposon mutants, is responsible for the secretion of all, or even most, of the FPR1-activating molecules in *Y. pestis* supernatant (Figure 3.7C). Given that the FPR1 agonists in *Y. pestis* supernatant retain their N-terminal formylation and are small in size (<10 kDa), these products may be secreted in three ways: through a secretion system that does not remove N-terminal signal sequences during translocation, passive diffusion through porins, or through the release of signal sequence cleavage products.

Bacterial peptide formylation is of interest clinically due to the typical requirement of peptide deformylase activity for bacterial growth. In this way, inhibitors of peptide deformylase have been developed as antibiotics.<sup>98-100</sup> The *def* gene of *Y. pestis* is highly conserved with that of other Gram-negative bacterial species. To the best of our knowledge, this study is the first to purify and demonstrate catalytic activity of *Y. pestis*

peptide deformylase. Given the activity of purified *def* for catalyzing peptide deformylation and the seeming essentiality of the formyl methionine transferase (*fmt*) gene, peptide deformylase inhibitors appear to be attractive candidates for last-line therapies to treat yersiniosis and plague infections.

## CONCLUSIONS

Early immune defenses to bacterial pathogens are thought to be critical for mounting timely immune responses and protecting hosts from severe disease. Formyl peptide receptors have been shown in many different infection models to drive a piece of this response. It therefore comes as little surprise that loss of FPRs typically renders hosts more susceptible to bacterial infection. Here, we report that loss of Fpr1, Fpr2 or Fpr3 enhances survival of mice to bubonic plague infection. While we observed FPR-dependent chemotaxis using *in vitro* neutrophil migration assays in response to *Y. pestis* culture products, we did not observe chemotaxis defects *in vivo*. Additionally, *Y. pestis* culture products were found to only activate Fpr1, and these products were identified as multiple short formylated peptides. Given the lack of Fpr2 or Fpr3 activation by *Y. pestis* products, we propose that these receptors respond to host-derived signals to enhance migration responses and/or alter inflammatory cytokine production. Future studies will be required to test this hypothesis and to survey more bacterial infection models to identify additional cases that behave like *Y. pestis*.

## REFERENCES

1. Zietz, B. P. & Dunkelberg, H. The history of the plague and the research on the causative agent *Yersinia pestis*. *International Journal of Hygiene and Environmental Health* **207**, 165–178 (2004).
2. Plague. <https://www.who.int/news-room/fact-sheets/detail/plague>.
3. Gonzalez, R. J. & Miller, V. L. A Deadly Path: Bacterial Spread During Bubonic Plague. *Trends Microbiol* **24**, 239–241 (2016).
4. Butler, T. Plague Gives Surprises in the First Decade of the 21st Century in the United States and Worldwide. *The American Journal of Tropical Medicine and Hygiene* **89**, 788–793 (2013).
5. Bosio, C. F., Jarrett, C. O., Gardner, D. & Hinnebusch, B. J. Kinetics of Innate Immune Response to *Yersinia pestis* after Intradermal Infection in a Mouse Model. *Infection and Immunity* **80**, 12 (2012).
6. Pechous, R. D., Sivaraman, V., Price, P. A., Stasulli, N. M. & Goldman, W. E. Early Host Cell Targets of *Yersinia pestis* during Primary Pneumonic Plague. *PLOS Pathogens* **9**, e1003679 (2013).
7. Hinnebusch, B. J., Jarrett, C. O. & Bland, D. M. “Fleaing” the Plague: Adaptations of *Yersinia pestis* to Its Insect Vector That Lead to Transmission. *Annu. Rev. Microbiol.* **71**, 215–232 (2017).
8. Shannon, J. G. *et al.* *Yersinia pestis* Subverts the Dermal Neutrophil Response in a Mouse Model of Bubonic Plague. *mBio* **4**, e00170-13 (2013).
9. Petri, B. & Sanz, M.-J. Neutrophil chemotaxis. *Cell Tissue Res* **371**, 425–436 (2018).

10. Comer, J. E. *et al.* Transcriptomic and Innate Immune Responses to *Yersinia pestis* in the Lymph Node during Bubonic Plague. *IAI* **78**, 5086–5098 (2010).
11. Spinner, J. L. *et al.* *Yersinia pestis* survival and replication within human neutrophil phagosomes and uptake of infected neutrophils by macrophages. *Journal of Leukocyte Biology* **95**, 389–398 (2014).
12. Pechous, R. D. Pneumonic Plague: The Darker Side of *Yersinia pestis*. 8.
13. Sebbane, F., Gardner, D., Long, D., Gowen, B. B. & Hinnebusch, B. J. Kinetics of Disease Progression and Host Response in a Rat Model of Bubonic Plague. *The American Journal of Pathology* **166**, 1427–1439 (2005).
14. Flexner, S. THE PATHOLOGY OF BUBONIC PLAGUE.1: (From the Pathological Laboratory of the University of Pennsylvania.) The Post-mortem Examinations.2. *The American Journal of the Medical Sciences (1827-1924)* **122**, 396 (1901).
15. Titball, R. W., Hill, J., Lawton, D. G. & Brown, K. A. *Yersinia pestis* and plague. *Biochemical Society Transactions* **31**, 104–107 (2003).
16. Survival and growth of *Yersinia pestis* within macrophages and an effect of the loss of the 47-megadalton plasmid on growth in macrophages | Infection and Immunity. [https://journals-asm-org.proxy.uchicago.edu/doi/10.1128/iai.47.1.234-241.1985?url\\_ver=Z39.88-2003&rfr\\_id=ori:rid:crossref.org&rfr\\_dat=cr\\_pub%20%20pubmed](https://journals-asm-org.proxy.uchicago.edu/doi/10.1128/iai.47.1.234-241.1985?url_ver=Z39.88-2003&rfr_id=ori:rid:crossref.org&rfr_dat=cr_pub%20%20pubmed).
17. Spinner, J. L. *et al.* *Yersinia pestis* survival and replication within human neutrophil phagosomes and uptake of infected neutrophils by macrophages. *Journal of Leukocyte Biology* **95**, 389–398 (2014).

18. Quinn, J. D., Weening, E. H., Miner, T. A. & Miller, V. L. Temperature Control of *psaA* Expression by PsaE and PsaF in *Yersinia pestis*. *Journal of Bacteriology* **201**, (2019).
19. Hampton, H. R. & Chtanova, T. Lymphatic Migration of Immune Cells. *Frontiers in Immunology* **10**, (2019).
20. Gonzalez, R. J., Lane, M. C., Wagner, N. J., Weening, E. H. & Miller, V. L. Dissemination of a Highly Virulent Pathogen: Tracking The Early Events That Define Infection. *PLOS Pathogens* **11**, e1004587 (2015).
21. Tacconelli, E. & Magrini, N. GLOBAL PRIORITY LIST OF ANTIBIOTIC-RESISTANT BACTERIA TO GUIDE RESEARCH, DISCOVERY, AND DEVELOPMENT OF NEW ANTIBIOTICS. *World Health Organization* **7** (2017).
22. Galán, J. E., Lara-Tejero, M., Marlovits, T. C. & Wagner, S. Bacterial type III secretion systems: specialized nanomachines for protein delivery into target cells. *Annu. Rev. Microbiol.* **68**, 415–438 (2014).
23. Cornelis, G. R. *Yersinia* type III secretion: send in the effectors. *J. Cell Biol.* **158**, 401–408 (2002).
24. Marketon, M. M., DePaolo, R. W., DeBord, K. L., Jabri, B. & Schneewind, O. Plague Bacteria Target Immune Cells During Infection. *Science* **309**, 1739–1741 (2005).
25. Montagner, C., Arquint, C. & Cornelis, G. R. Translocators YopB and YopD from *Yersinia enterocolitica* Form a Multimeric Integral Membrane Complex in Eukaryotic Cell Membranes. *Journal of Bacteriology* **193**, 6923–6928 (2011).

26. Plano, G. V. & Schesser, K. The *Yersinia pestis* type III secretion system: expression, assembly and role in the evasion of host defenses. *Immunol. Res.* **57**, 237–245 (2013).
27. Osei-Owusu, P., Charlton, T. M., Kim, H. K., Missiakas, D. & Schneewind, O. FPR1 is the plague receptor on host immune cells. *Nature* (2019) doi:10.1038/s41586-019-1570-z.
28. Quenee, L. E., Cornelius, C. A., Ciletti, N. A., Elli, D. & Schneewind, O. *Yersinia pestis* caf1 Variants and the Limits of Plague Vaccine Protection. *Infection and Immunity* **76**, 2025–2036 (2008).
29. Oldekamp, S. *et al.* Lack of formyl peptide receptor 1 and 2 leads to more severe inflammation and higher mortality in mice with of pneumococcal meningitis. *Immunology* **143**, 447–461 (2014).
30. Gao, J.-L., Lee, E. J. & Murphy, P. M. Impaired Antibacterial Host Defense in Mice Lacking the N-formylpeptide Receptor. *J Exp Med* **189**, 657–662 (1999).
31. Zhang, M. *et al.* A Critical Role of Formyl Peptide Receptors in Host Defense against *Escherichia coli*. *The Journal of Immunology* **204**, 2464–2473 (2020).
32. Dorward, D. A. *et al.* The role of formylated peptides and formyl peptide receptor 1 in governing neutrophil function during acute inflammation. *Am. J. Pathol.* **185**, 1172–1184 (2015).
33. He, H.-Q. & Ye, R. D. The Formyl Peptide Receptors: Diversity of Ligands and Mechanism for Recognition. *Molecules* **22**, (2017).

34. Wang, J. & Ye, R. D. Agonist concentration–dependent changes in FPR1 conformation lead to biased signaling for selective activation of phagocyte functions. *Proceedings of the National Academy of Sciences* **119**, e2201249119 (2022).
35. Dietschi, Q. *et al.* Evolution of immune chemoreceptors into sensors of the outside world. *PNAS* (2017) doi:10.1073/pnas.1704009114.
36. Migeotte, I., Communi, D. & Parmentier, M. Formyl peptide receptors: A promiscuous subfamily of G protein-coupled receptors controlling immune responses. *Cytokine & Growth Factor Reviews* **17**, 501–519 (2006).
37. Winther, M., Dahlgren, C. & Forsman, H. Formyl Peptide Receptors in Mice and Men: Similarities and Differences in Recognition of Conventional Ligands and Modulating Lipopeptides. *Basic & Clinical Pharmacology & Toxicology* **122**, 191–198 (2018).
38. Bufe, B. *et al.* Bacterial MgrB peptide activates chemoreceptor Fpr3 in mouse accessory olfactory system and drives avoidance behaviour. *Nature Communications* **10**, 1–16 (2019).
39. Stempel, H. *et al.* Strain-specific Loss of Formyl Peptide Receptor 3 in the Murine Vomeronasal and Immune Systems. *J. Biol. Chem.* **291**, 9762–9775 (2016).
40. Gao, J.-L., Lee, E. J. & Murphy, P. M. Impaired Antibacterial Host Defense in Mice Lacking the N-formylpeptide Receptor. *J Exp Med* **189**, 657–662 (1999).
41. Weiss, E. *et al.* Formyl-peptide receptor 2 governs leukocyte influx in local *Staphylococcus aureus* infections. *The FASEB Journal* **32**, 26–36 (2017).
42. Sharba, S. *et al.* Formyl peptide receptor 2 orchestrates mucosal protection against *Citrobacter rodentium* infection. *Virulence* **10**, 610–624 (2019).

43. Rüger, M. *et al.* *Formyl peptide receptor agonist Ac2-26 alleviates neuroinflammation in a mouse model of pneumococcal meningitis.*  
<https://www.researchsquare.com/article/rs-28938/v1> (2020) doi:10.21203/rs.3.rs-28938/v1.
44. Liu, M. *et al.* Formylpeptide receptors are critical for rapid neutrophil mobilization in host defense against *Listeria monocytogenes*. *Scientific Reports* **2**, 786 (2012).
45. Silver, L. *Mouse Genetics: Concepts and Applications*. (Oxford University Press, 1995).
46. Turner, J. K., McAllister, M. M., Xu, J. L. & Tapping, R. I. The Resistance of BALB/cJ Mice to *Yersinia pestis* Maps to the Major Histocompatibility Complex of Chromosome 17. *Infection and Immunity* **76**, 4092–4099 (2008).
47. Tencati, M. & Tapping, R. I. Resistance of Mice of the 129 Background to *Yersinia pestis* Maps to Multiple Loci on Chromosome 1. *Infection and Immunity* **84**, 2904–2913 (2016).
48. Turner, J. K., Xu, J. L. & Tapping, R. I. Substrains of 129 Mice Are Resistant to *Yersinia pestis* KIM5: Implications for Interleukin-10-Deficient Mice. *Infection and Immunity* **77**, 367–373 (2009).
49. Prat, C., Bestebroer, J., de Haas, C. J. C., van Strijp, J. A. G. & van Kessel, K. P. M. A New Staphylococcal Anti-Inflammatory Protein That Antagonizes the Formyl Peptide Receptor-Like 1. *The Journal of Immunology* **177**, 8017–8026 (2006).
50. Prat, C. *et al.* A Homolog of Formyl Peptide Receptor-Like 1 (FPRL1) Inhibitor from *Staphylococcus aureus* (FPRL1 Inhibitory Protein) That Inhibits FPRL1 and FPR. *The Journal of Immunology* **183**, 6569–6578 (2009).

51. Postma, B. *et al.* Chemotaxis Inhibitory Protein of *Staphylococcus aureus* Binds Specifically to the C5a and Formylated Peptide Receptor. *The Journal of Immunology* **172**, 6994–7001 (2004).
52. Rautenberg, M., Joo, H.-S., Otto, M. & Peschel, A. Neutrophil responses to staphylococcal pathogens and commensals via the formyl peptide receptor 2 relates to phenol-soluble modulins release and virulence. *FASEB J* **25**, 1254–1263 (2011).
53. Stemerding, A. M. *et al.* *Staphylococcus aureus* Formyl Peptide Receptor-like 1 Inhibitor (FLIPr) and Its Homologue FLIPr-like Are Potent FcγR Antagonists That Inhibit IgG-Mediated Effector Functions. *The Journal of Immunology* **191**, 353–362 (2013).
54. de Haas, C. J. C. *et al.* Chemotaxis Inhibitory Protein of *Staphylococcus aureus*, a Bacterial Antiinflammatory Agent. *J Exp Med* **199**, 687–695 (2004).
55. Kim, H. K., Thammavongsa, V., Schneewind, O. & Missiakas, D. Recurrent infections and immune evasion strategies of *Staphylococcus aureus*. *Curr Opin Microbiol* **15**, 92–99 (2012).
56. von Köckritz-Blickwede, M. *et al.* Immunological Mechanisms Underlying the Genetic Predisposition to Severe *Staphylococcus aureus* Infection in the Mouse Model. *The American Journal of Pathology* **173**, 1657–1668 (2008).
57. Johnson, N. V. *et al.* Haplotype Association Mapping Identifies a Candidate Gene Region in Mice Infected With *Staphylococcus aureus*. *G3: Genes, Genomes, Genetics* **2**, 693–700 (2012).
58. Kroeze, W. K. *et al.* PRESTO-Tango as an open-source resource for interrogation of the druggable human GPCRome. *Nat Struct Mol Biol* **22**, 362–369 (2015).

59. Tae, Y.-M. *et al.* Airway Activation of Formyl Peptide Receptors Inhibits Th1 and Th17 Cell Responses via Inhibition of Mediator Release from Immune and Inflammatory Cells and Maturation of Dendritic Cells. *J.I.* **188**, 1799–1808 (2012).
60. Lämmermann, T. *et al.* Neutrophil swarms require LTB4 and integrins at sites of cell death in vivo. *Nature* **498**, 371–375 (2013).
61. Lämmermann, T. In the eye of the neutrophil swarm—navigation signals that bring neutrophils together in inflamed and infected tissues. *Journal of Leukocyte Biology* **100**, 55–63 (2016).
62. Expression and functional role of formyl peptide receptor in human bone marrow-derived mesenchymal stem cells - Kim - 2007 - FEBS Letters - Wiley Online Library. <https://febs-onlinelibrary-wiley-com.proxy.uchicago.edu/doi/full/10.1016/j.febslet.2007.03.078>.
63. N-Formyl-Methionyl-Leucyl-Phenylalanine (fMLP) Promotes Osteoblast Differentiation via the N-Formyl Peptide Receptor 1-mediated Signaling Pathway in Human Mesenchymal Stem Cells from Bone Marrow - PMC. <https://www.ncbi.nlm-nih-gov.proxy.uchicago.edu/pmc/articles/PMC3089557/>.
64. Zhang, L. *et al.* Formyl peptide receptors promotes neural differentiation in mouse neural stem cells by ROS generation and regulation of PI3K-AKT signaling. *Sci Rep* **7**, 206 (2017).
65. Paterson, N. M. *et al.* *Dynamic evolution of bacterial ligand recognition by formyl peptide receptors*. <http://biorxiv.org/lookup/doi/10.1101/2021.08.02.454796> (2021) doi:10.1101/2021.08.02.454796.

66. Sztupinski, Z. *et al.* A major genetic accelerator of cancer diagnosis: rs867228 in FPR1. *OncotImmunology* **10**, 1859064 (2021).
67. Snapkov, I. *et al.* The role of formyl peptide receptor 1 (FPR1) in neuroblastoma tumorigenesis. *BMC Cancer* **16**, 490 (2016).
68. Li, S.-Q. *et al.* The Role of Formyl Peptide Receptor 1 Gene Polymorphisms in Human Colorectal Cancer. *J. Cancer* **11**, 3580–3587 (2020).
69. Zhang, L. *et al.* Formyl peptide receptors promotes neural differentiation in mouse neural stem cells by ROS generation and regulation of PI3K-AKT signaling. *Scientific Reports* **7**, 1–16 (2017).
70. James Ancliff, P. Congenital neutropenia. *Blood Reviews* **17**, 209–216 (2003).
71. Wollam, J. *et al.* Microbiota-Produced N-Formyl Peptide fMLF Promotes Obesity-Induced Glucose Intolerance. *Diabetes* **68**, 1415–1426 (2019).
72. Thammavongsa, V., Kim, H. K., Missiakas, D. & Schneewind, O. Staphylococcal manipulation of host immune responses. *Nat Rev Microbiol* **13**, 529–543 (2015).
73. Iii, P. L. G., Lin, S. X. & Larson, E. L. A U.S. Population-Based Survey of Staphylococcus aureus Colonization. **9**.
74. Chen, K. *et al.* Cutting Edge: A Critical Role for the G Protein-Coupled Receptor mFPR2 in Airway Inflammation and Immune Responses. *The Journal of Immunology* **184**, 3331–3335 (2010).
75. Gonzalez, R. J., Weening, E. H., Lane, M. C. & Miller, V. L. Comparison of Models for Bubonic Plague Reveals Unique Pathogen Adaptations to the Dermis. *Infection and Immunity* **83**, 2855–2861 (2015).

76. Surgalla, M. J. & Beesley, E. D. Congo Red-Agar Plating Medium for Detecting Pigmentation in *Pasteurella pestis*. *Appl Microbiol* **18**, 834–837 (1969).
77. Hirche, T. O., Atkinson, J. J., Bahr, S. & Belaaouaj, A. Deficiency in Neutrophil Elastase Does Not Impair Neutrophil Recruitment to Inflamed Sites. *Am J Respir Cell Mol Biol* **30**, 576–584 (2004).
78. Dürr, M. C. *et al.* Neutrophil chemotaxis by pathogen-associated molecular patterns – formylated peptides are crucial but not the sole neutrophil attractants produced by *Staphylococcus aureus*. *Cellular Microbiology* **8**, 207–217 (2006).
79. Harris, G., Holbein, B. E., Zhou, H., Xu, H. H. & Chen, W. Potential Mechanisms of Mucin-Enhanced *Acinetobacter baumannii* Virulence in the Mouse Model of Intraperitoneal Infection. *Infection and Immunity* **87**, e00591-19.
80. Gonçalves, A.-S. & Appelberg, R. The Involvement of the Chemokine Receptor CXCR2 in Neutrophil Recruitment in LPS-Induced Inflammation and in *Mycobacterium avium* Infection. *Scandinavian Journal of Immunology* **55**, 585–591 (2002).
81. Southgate, E. L. *et al.* Identification of formyl peptides from *Listeria monocytogenes* and *Staphylococcus aureus* as potent chemoattractants for mouse neutrophils. *J. Immunol.* **181**, 1429–1437 (2008).
82. Weiß, E., Schlatterer, K., Beck, C., Peschel, A. & Kretschmer, D. Formyl-Peptide Receptor Activation Enhances Phagocytosis of Community-Acquired Methicillin-Resistant *Staphylococcus aureus*. *J Infect Dis* **221**, 668–678 (2020).

83. Staphylococcal Protein A Contributes to Persistent Colonization of Mice with Staphylococcus aureus | Journal of Bacteriology. <https://journals-asm-org.proxy.uchicago.edu/doi/full/10.1128/JB.00735-17>.
84. Holtfreter, S. *et al.* Characterization of a Mouse-Adapted Staphylococcus aureus Strain. *PLOS ONE* **8**, e71142 (2013).
85. Wen, X. *et al.* G-protein–coupled formyl peptide receptors play a dual role in neutrophil chemotaxis and bacterial phagocytosis. *MBoC* **30**, 346–356 (2018).
86. Al-Jawdah, A. D. *et al.* Induction of the immunoprotective coat of Yersinia pestis at body temperature is mediated by the Caf1R transcription factor. *BMC Microbiology* **19**, 68 (2019).
87. Machado, M. G. *et al.* The Annexin A1/FPR2 pathway controls the inflammatory response and bacterial dissemination in experimental pneumococcal pneumonia. *The FASEB Journal* **34**, 2749–2764 (2020).
88. Nauth, T. *et al.* Visualization of translocons in Yersinia type III protein secretion machines during host cell infection. *PLoS Pathog* **14**, e1007527 (2018).
89. Bruschi, M. *et al.* Annexin A1 and Autoimmunity: From Basic Science to Clinical Applications. *Int J Mol Sci* **19**, 1348 (2018).
90. Sundqvist, M. *et al.* Staphylococcus aureus–Derived PSM $\alpha$  Peptides Activate Neutrophil FPR2 but Lack the Ability to Mediate  $\beta$ -Arrestin Recruitment and Chemotaxis. *The Journal of Immunology* **203**, 3349–3360 (2019).
91. Welkos, S., Friedlander, A., McDowell, D., Weeks, J. & Tobery, S. V antigen of Yersinia pestis inhibits neutrophil chemotaxis. *Microbial Pathogenesis* **24**, 185–196 (1998).

92. RajBhandary, U. L. Initiator transfer RNAs. *J Bacteriol* **176**, 547–552 (1994).
93. Giglione, C., Boularot, A. & Meinnel, T. Protein N-terminal methionine excision. *CMLS, Cell. Mol. Life Sci.* **61**, 1455–1474 (2004).
94. De Bernardo, S. *et al.* Studies on the reaction of fluorecamine with primary amines. *Archives of Biochemistry and Biophysics* **163**, 390–399 (1974).
95. Kim, D. *et al.* Identification and characterization of an atypical Gas-biased  $\beta$ 2AR agonist that fails to evoke airway smooth muscle cell tachyphylaxis. *Proceedings of the National Academy of Sciences* **118**, e2026668118 (2021).
96. Sing, A., Roggenkamp, A., Geiger, A. M. & Heesemann, J. *Yersinia enterocolitica* Evasion of the Host Innate Immune Response by V Antigen-Induced IL-10 Production of Macrophages Is Abrogated in IL-10-Deficient Mice. *The Journal of Immunology* **168**, 1315–1321 (2002).
97. Reithmeier-Rost, D. *et al.* The weak interaction of LcrV and TLR2 does not contribute to the virulence of *Yersinia pestis*. *Microbes and Infection* **9**, 997–1002 (2007).
98. Apfel, C. M. *et al.* Peptide Deformylase as an Antibacterial Drug Target: Target Validation and Resistance Development. *Antimicrob Agents Chemother* **45**, 1058–1064 (2001).
99. Fieulaine, S. *et al.* A unique peptide deformylase platform to rationally design and challenge novel active compounds. *Sci Rep* **6**, 35429 (2016).
100. Clements, J. M. *et al.* Antibiotic Activity and Characterization of BB-3497, a Novel Peptide Deformylase Inhibitor. *Antimicrobial Agents and Chemotherapy* **45**, 563–570 (2001).

## TABLES

Position	rsIDs	Reference	Alternate	Protein Consequence	VEP Annotation	Allele Count	Allele Frequency	Homozygote Count
52250216	rs5030878	A	G	p.Ile11Thr	missense variant	226991	0.80513248	91689
52249211	rs867228	T	G	p.Glu346Ala	missense variant	226461	0.80226799	91066
52249947	rs2070745	C	G	p.Val101Leu	missense variant	112241	0.3971502	23857
52249702	rs2070746	G	T	p.Pro182Pro	synonymous variant	94495	0.33436301	16970
52249672	rs1042229	A	C	p.Asn192Lys	missense variant	91185	0.32267368	15371
52249680	rs5030880	T	A	p.Arg190Trp	missense variant	37604	0.13304934	2797
52249672	rs1042229	A	G	p.Asn192Asn	synonymous variant	37308	0.13202072	2742
52249942	rs28930680	A	G	p.Phe102Phe	synonymous variant	11376	0.04023171	346
52249900	rs5030879	G	A	p.Ile116Ile	synonymous variant	9934	0.03514619	1205
52249255	rs17849971	G	A	p.Thr331Thr	synonymous variant	6014	0.02127916	106
52250071	rs61736491	G	A	p.Val59Val	synonymous variant	2413	0.00853066	45
52249959	rs78488639	G	T	p.Leu97Met	missense variant	2376	0.00840247	69
52249760	rs111768566	C	T	p.Arg163His	missense variant	1196	0.00423057	7
52250131	rs149382837	G	A	p.Leu39Leu	synonymous variant	797	0.00281817	14
52249442	rs142210016	C	T	p.Arg269His	missense variant	369	0.00130786	2
52250222	rs148095693	G	A	p.Thr9Met	missense variant	289	0.00102585	2
52249603	rs35264765	G	A	p.Ser215Ser	synonymous variant	243	0.00085959	1
52249641	rs150239733	T	C	p.Ile203Val	missense variant	233	0.00082414	2
52249151	rs199734809	C	A		3 prime UTR variant	186	0.00069732	1
52249426	rs547725110	G	A	p.Gly274Gly	synonymous variant	166	0.00058813	3
52249880	rs149931707	C	T	p.Arg123His	missense variant	164	0.00058024	0
52249695	rs145973159	T	C	p.Asn185Asp	missense variant	114	0.00040319	2
52250231	rs757666229	G	A	p.Ser6Phe	missense variant	92	0.00032726	0
52249808	rs142367736	A	G	p.Ile147Thr	missense variant	79	0.00027947	0
52249390	rs371692364	T	C	p.Thr286Thr	synonymous variant	71	0.00025131	0

**Table 1.1: The top 25 FPR1 allele variants from the gnomAD v2.1.1 database.** A table showing the results of the top 25 FPR1 allele variants in the human exome database gnomAD.

<b>Name</b>	<b>Description</b>	<b>Sequence</b>
BS019	Forward primer for Fpr1 genotyping	ccattttacattgccagcat
BS021	Reverse primer for Fpr1 KO genotyping - binds to NeoR insert	atgcagaacacaaatacagc
BS022	Reverse primer for Fpr1 genotyping - binds WT Fpr1 in NeoR-replaced segment	TGCCGAATATCATGGTGGAA
BS006	Forward primer for Fpr2 genotyping	TTTCCTCTCTGTTCCACCTCA
BS007	Reverse primer for Fpr2 genotyping	CGGAATCCAGCTACCCAAAT
BS011	Forward primer for Fpr3 genotyping	GCAACATCTGAGAAATTGTTATTG
BS013	Reverse primer for Fpr3 genotyping	CGAGAAGACAGGGAATGAATC
BS023	Clal F Fpr1 - For cloning into PRESTO-Tango plasmid backbone	AAAAATCGATatggacaccaacatgtctct
BS024	Clal R Fpr1 - For cloning into PRESTO-Tango plasmid backbone	AAAAATCGATcattgcattaaagtgtttcagaa
BS025	Clal F Fpr2 - For cloning into PRESTO-Tango plasmid backbone	AAAAATCGATatggaatccaactactccatc
BS026	Clal R Fpr2 - For cloning into PRESTO-Tango plasmid backbone	AAAAATCGATtggggcctttaactcaatgt
BS027	Clal F Fpr3 - For cloning into PRESTO-Tango plasmid backbone	AAAAATCGATATGGAAACCAACTACTCTATCCCTT
BS028	Clal R Fpr3 - For cloning into PRESTO-Tango plasmid backbone	AAAAATCGATTATTGCCTTTATTTCAATGTCTTCAGGA
BS029	Seq F PRESTO-Tango	CATCTTCTGCCTGGTATTTCGC
BS030	Seq R PRESTO-Tango	GGTGCAGGACTCATCTTGG

**Table 1.2: Primer names, descriptions, and sequences used in this dissertation.**

<b>Name</b>	<b>Target</b>	<b>Sequence</b>	<b>On/Off target scores</b>
Guide A	Fpr2 promoter region	TGTATACCACCTGCTACTACAGG	73/77
Guide B	Fpr2 exon	TGTTAACCCAACAAGCTCATTGG	62/58
Guide C	Fpr3 exon	TGGGAAATGGACTAGTGATCTGG	58/56
Guide D	Fpr3 exon	GGTTAACCAACCGGAAAATCCGT	69/62

**Table 1.3: CRISPR gRNA sequences.** On/Off target scores are calculated by IDT.

## FIGURES

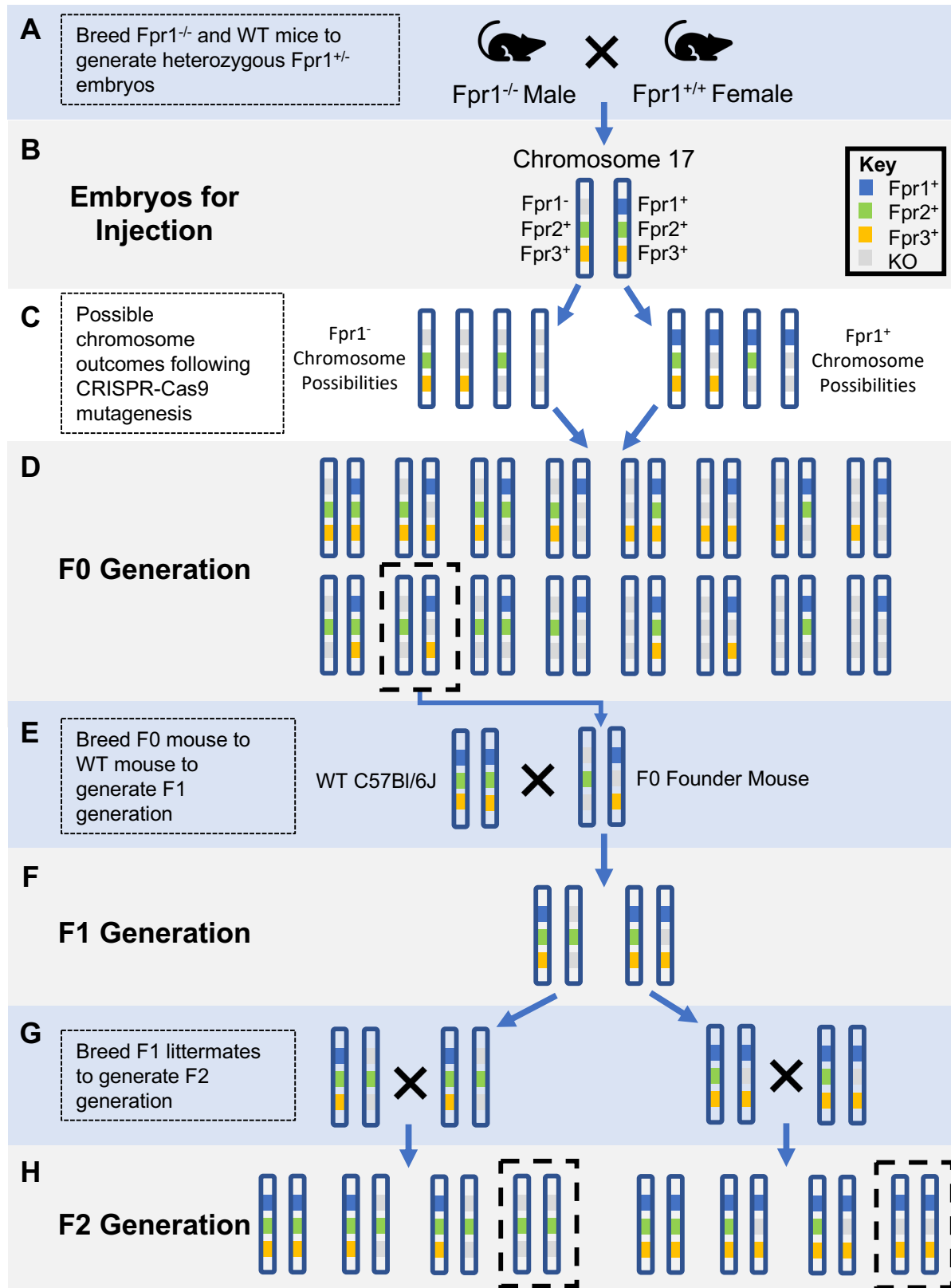
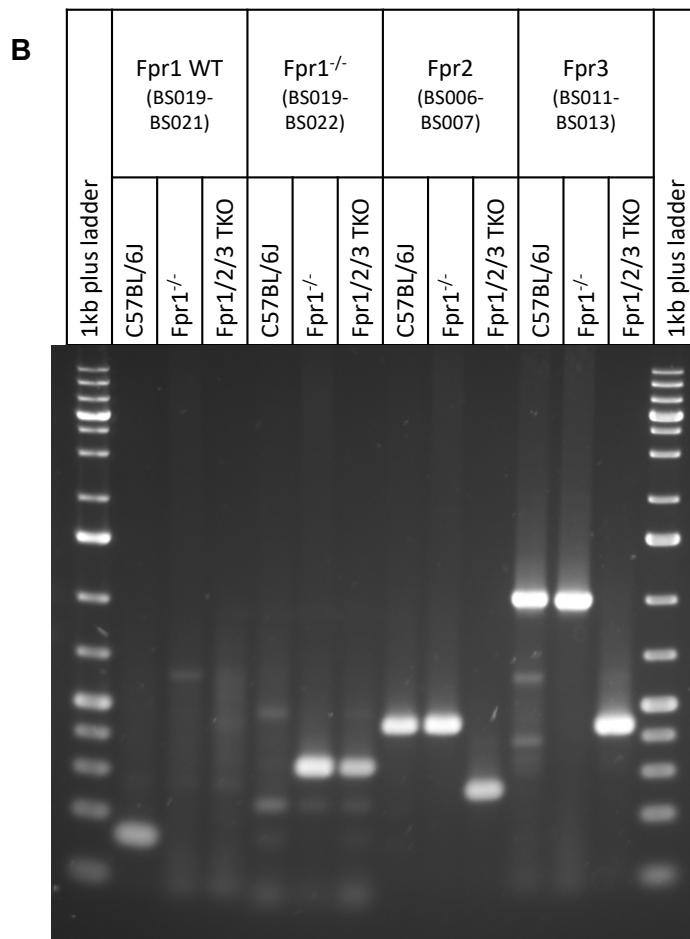
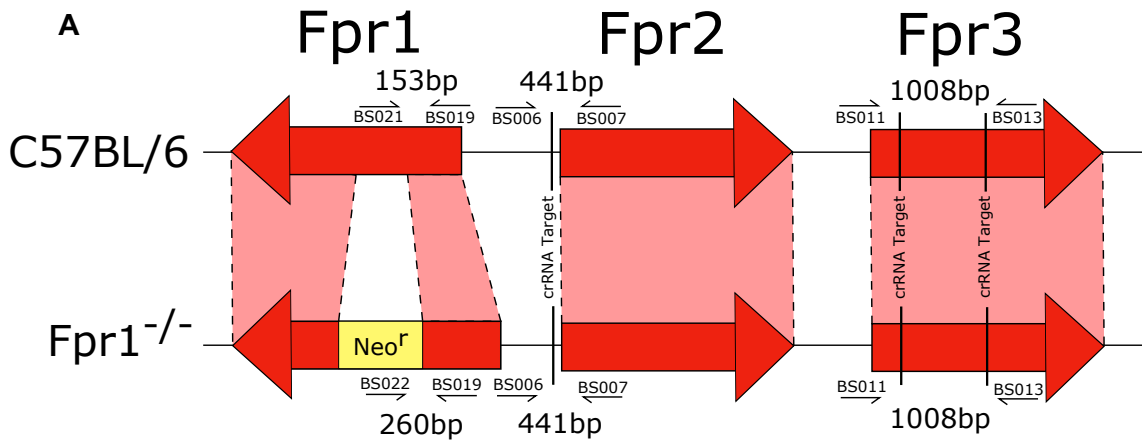


Figure 1.1: Breeding approach for generating FPR knockout mice.

**Figure 1.1 (Continued): Breeding approach for generating FPR knockout mice.**

Diagram of the complete breeding approach from embryo mutagenesis to homozygous mutant isolation. A.  $Fpr1^{-/-}$  males are bred with  $Fpr1^{+/+}$  female C57Bl/6J mice to generate heterozygous  $Fpr1^{+/-}$  embryos. B. Heterozygous embryos inherit an  $Fpr1^{-}$  Chromosome 17 from the  $Fpr1^{-/-}$  father and an  $Fpr1^{+}$  Chromosome 17 from the  $Fpr1^{+/+}$  mother. C. CRISPR-Cas9 mutagenesis targeting  $Fpr2$  and  $Fpr3$  has 4 possible outcomes per chromosome based on target cleavage efficiency. D. All possible chromosome combinations for mice in the F0 generation following CRISPR-Cas9 mutagenesis. E. Mice from the F0 generation are bred with WT C57Bl/6 mice to generate the F1 generation. A genotype from the F0 generation is selected as an example. F. The breeding cross from E generates Chromosome 17 heterozygous mice. This is the F1 generation. G. Littermates from the F1 generation are bred to enable isolation of Chromosome 17 homozygous mice. H. All possible genotypes for the F2 generation from the indicated breeding crosses. 25% of the F2 generation is expected to be homozygous at the FPR locus derived from CRISPR-Cas9-mutagenized F0 mice.



**Figure 1.2: Genotyping of knockout mouse lines.** A. Primer map showing CRISPR crRNA target regions and expected primer amplification lengths. Fpr1<sup>-/-</sup> mice carry a Neo<sup>r</sup> gene that replaces a portion of the Fpr1 gene. B. PCR results using primer sets specific for the Fpr1 WT locus, Fpr1<sup>-/-</sup> Neo<sup>r</sup> cassette, or spanning the Fpr2 and Fpr3 crRNA target sites. DNA extracted from C57BL/6J, Fpr1<sup>-/-</sup>, and Fpr1/2/3<sup>-/-</sup> mice are shown.

```

FPR2_C57B1/6      tttcctctctgttcaccctcagttcagtatcactggtgagacatgagggcttattatTTT
FPR2_SKO_323      -----ttgagacatgagggcttattatTTT
                      *****

FPR2_C57B1/6      ttgtaattagtttaaagcaggaatagttttaagaatatgagaaatgtggagagctatgc
FPR2_SKO_323      ttgtaattagtttaaagcaggaatagttttaagaatatgagaaatgtggagagctatgc
                      *****

FPR2_C57B1/6      taccocagaaaggtatgcagtaaagtgctagttttgaaatgttactgtgaaaatgctctc
FPR2_SKO_323      taccocagaaaggtatgcagtaaagtgctagttttgaaatgttactgtgaaaatgctcct
                      *****..

FPR2_C57B1/6      ctgtagtagcaggtggtatacattctaaatgagtgcatgtcagaaggagccaaatatct
FPR2_SKO_323      -----

FPR2_C57B1/6      gagaaatggttgtttttgaaaactttcaggtgcagacaaaattggaatccaactactccat
FPR2_SKO_323      -----

FPR2_C57B1/6      ccatctgaatggatcagaagtggtggttatgattctaccatctccagagtctctgtggat
FPR2_SKO_323      -----

FPR2_C57B1/6      cctctcaatggtggttctccatcactttcttctccttggtgtgctgggcaatggactagt
FPR2_SKO_323      -----

FPR2_C57B1/6      gatttgggtagctggattccggatgccacacactgtcaccactatctggtatctgaaatc
FPR2_SKO_323      -----

FPR2_C57B1/6      agcattggctgacttttctttcacagcaactctaccattccttctgttgaaatggctat
FPR2_SKO_323      -----

FPR2_C57B1/6      gaaagaaaaatggccttttggctggttctctgtgtaaatagttcacattgtggtagatgt
FPR2_SKO_323      -----

FPR2_C57B1/6      aaacctggttgaaagtgtcttcttgattgctctcattgccttggaccgctgcatttgtgt
FPR2_SKO_323      -----

FPR2_C57B1/6      tctgcatccagctctgggctcagaaccaccgcaactgtgagcctggctaggaagtggttgt
FPR2_SKO_323      -----

FPR2_C57B1/6      tgggcctggatttttctctgattctcactttgccatttttattttcttgactactgt
FPR2_SKO_323      -----

FPR2_C57B1/6      tagaattcctggaggagatgtgtattgtacattcaactttggatcctgggctcaaactga
FPR2_SKO_323      -----

FPR2_C57B1/6      tgaagaaaagttgaacacagctatcacttttgaacaactagagggatcatcaggttctct
FPR2_SKO_323      -----

FPR2_C57B1/6      tattggttccagcatgccatgtcaattgtgtgtgttctatggactcattgtctgcaaa
FPR2_SKO_323      -----

FPR2_C57B1/6      gatcaacagaagaaacctgttaattccagccgtcctttacgagtccttacagcagttgt
FPR2_SKO_323      -----

```

**Figure 1.3: Fpr2<sup>-/-</sup> sequencing alignment for Fpr2<sup>-/-</sup> mouse line derived from founder 323.** Alignment of the Fpr2 gene region between the C57Bl/6 reference genome and the consensus sequence from forward and reverse DNA sequencing reactions of the Fpr2 gene region in the Fpr2<sup>-/-</sup> mouse line derived from founder mouse 323. The C57Bl/6 sequence spans positions 18,112,726 – 18,113,977 in the whole genome reference sequence deposited on ensembl.org. The translation start codon is noted in bold. Alignments were generated using MAFFT. Asterisks represent positions of identity. Alignment is continued on the next page.

```

FPR2_C57B1/6      ggcttccttctttatctgctggtttcccttcagcttgtggccctttgggcacagtctg
FPR2_SKO_323      -----

FPR2_C57B1/6      gtttaaagagacattgcttagtggttagttataaaattcttgacatgtttgtaacccaac
FPR2_SKO_323      -----

FPR2_C57B1/6      aagctcat-----
FPR2_SKO_323      -ggcccatgaaaacatagagaattggattgaggcagctattgaaaaaggccaatgaactg
                      .**.***

FPR2_C57B1/6      -----
FPR2_SKO_323      gttggattaaccaacctgccaataatttataactaccactaaactgcatctctttgagc

FPR2_C57B1/6      -----tggcttacttcaatagttgtctcaatccgatgctctatgttttc
FPR2_SKO_323      cagactgtgcctaaaagggttacttcaatagttgtctcaatccgatgctctatgttttc
                      *****

FPR2_C57B1/6      atgggccaggactttcgtgagagattattcattccctgccttatagtcttgagagagcc
FPR2_SKO_323      atgggccagga-----
                      *****

```

**Figure 1.3 (Continued): Fpr2<sup>-/-</sup> sequencing alignment for Fpr2<sup>-/-</sup> mouse line derived from founder 323.** Alignment of the Fpr2 gene region between the C57Bl/6 reference genome and the consensus sequence from forward and reverse DNA sequencing reactions of the Fpr2 gene region in the Fpr2<sup>-/-</sup> mouse line derived from founder mouse 323. The C57Bl/6 sequence spans positions 18,112,726 – 18,113,977 in the whole genome reference sequence deposited on ensembl.org. The translation start codon is noted in bold. Alignments were generated using MAFFT. Asterisks represent positions of identity.

```

1. FPR3_SKO_327 atggaaccaactactctatccctttgaatggatcagatgtgggtgatctatgattctacc
2. FPR3_C57BL6 atggaaccaactactctatccctttgaatggatcagatgtgggtgatctatgattctacc
*****

1. FPR3_SKO_327 atctccagggttctgtggatcctctcaatgggtgtgtctccatcactttctctcttggt
2. FPR3_C57BL6 atctccagggttctgtggatcctctcaatgggtgtgtctccatcactttctctcttggt
*****

1. FPR3_SKO_327 gtgctgggaaatggactagt-----
2. FPR3_C57BL6 gtgctgggaaatggactagtctggtagctggattccggatgccacacactgtcacc
*****

1. FPR3_SKO_327 -----
2. FPR3_C57BL6 actatctggatctgaatctagcattggctgacttctctttcacagcaactctaccattc
*****

1. FPR3_SKO_327 -----
2. FPR3_C57BL6 cttcttgtgaaatggctatgaaagaaaatggccttttggctggttctctgtgaaatta

1. FPR3_SKO_327 -----
2. FPR3_C57BL6 gttcacattgcagtagatgtaaacctatttggaaagtgtcttcttgattgctgtcattgac

1. FPR3_SKO_327 -----
2. FPR3_C57BL6 ttggaccgctgtatttgtgtcctgcacccagctctgggctcagaaccaccgcaactgtgagc

1. FPR3_SKO_327 -----
2. FPR3_C57BL6 ctggctagaaatgtggttgttgggtcctggatttttgcctctcattctcactttgcccctt

1. FPR3_SKO_327 -----
2. FPR3_C57BL6 ttctcttcttctgactacagttagagatgctagagggatgtgcactgtagattgagcttt

1. FPR3_SKO_327 -----
2. FPR3_C57BL6 gtatcctggggcaactctgttgaggaaagttgaacacagctatcacgtttgtaacaact

1. FPR3_SKO_327 -----
2. FPR3_C57BL6 agagggatcatcaggttcattgttagcttcagcttgccatgtcctttgttgccatctgc

1. FPR3_SKO_327 -----
2. FPR3_C57BL6 tatggactcatcactacaagattcacaanaagccttggtaattccagcgccttttc

1. FPR3_SKO_327 -----
2. FPR3_C57BL6 cgagttcttacaggagtgtgggtcctctttatctgttggtttctttccaattgggt

1. FPR3_SKO_327 -----ggcacagctctggctcaaagagatgcagtttagtggtagttataaaattatt
2. FPR3_C57BL6 gcccttttaggcacagctctggctcaaagagatgcagtttagtggtagttataaaattatt
*****

1. FPR3_SKO_327 ggcaggttggttaatccaaccagttcattggcctttttcaatagctgcctcaatccaatt
2. FPR3_C57BL6 ggcaggttggttaatccaaccagttcattggcctttttcaatagctgcctcaatccaatt
*****

1. FPR3_SKO_327 ctctatgttttcatgggocaggactttcaagaagactgattcattccctgtcttctcgt
2. FPR3_C57BL6 ctctatgttttcatgggocaggactttcaagaagactgattcattccctgtcttctcgt
*****

1. FPR3_SKO_327 ctgcagagagccctgagtgaggactctggctcatatcagtgatacaagaaccaatttggt
2. FPR3_C57BL6 ctgcagagagccctgagtgaggactctggctcatatcagtgatacaagaaccaatttggt
*****

1. FPR3_SKO_327 tcacttctgaagacattgaaataaaggcaatatga
2. FPR3_C57BL6 tcacttctgaagacattgaaataaaggcaatatga
*****

```

**Figure 1.4: Fpr3<sup>-/-</sup> sequencing alignment for Fpr3<sup>-/-</sup> mouse line derived from founder 327.** Alignment of the Fpr3 coding sequence between the C57Bl/6 reference genome and the consensus sequence from forward and reverse DNA sequencing reactions of the Fpr3 gene region in the Fpr3<sup>-/-</sup> mouse line derived from founder mouse 327. The C57Bl/6 sequence spans positions 18,190,720 – 18,191,939 in the whole genome reference sequence deposited on ensembl.org. Alignments were generated using MAFFT. Asterisks represent positions of identity.

```

1. FPR3_SKO_328 atggaaccaactactctatcccttgaatggatcagatgtggtgatctatgattctacc
2. FPR3_C57BL6 atggaaccaactactctatcccttgaatggatcagatgtggtgatctatgattctacc
*****

1. FPR3_SKO_328 atctccagggttctgtggatcctctcaatgggtgtctccatcactttctccttgg
2. FPR3_C57BL6 atctccagggttctgtggatcctctcaatgggtgtctccatcactttctccttgg
*****

1. FPR3_SKO_328 gtgctgggaatgg-----
2. FPR3_C57BL6 gtgctgggaatggactagtgatctggtagctggattccggatgccacacactgtcacc
*****

1. FPR3_SKO_328 -----
2. FPR3_C57BL6 actatctggtatctgaatctagcattggctgacttctctttcacagcaactctaccattc

1. FPR3_SKO_328 -----
2. FPR3_C57BL6 ctctctgttgaaatggctatgaaagaaaaatggccttttggctggttctctgtgtaaatga

1. FPR3_SKO_328 -----
2. FPR3_C57BL6 gttcacattgcagtagatgtaaacctatttgaagtgtctctctgattgctgtcattggc

1. FPR3_SKO_328 -----
2. FPR3_C57BL6 ttggaccgctgtatttgtgtcctgcatccagctctgggctcagaaccaccgactgtgagc

1. FPR3_SKO_328 -----
2. FPR3_C57BL6 ctggctagaatgtggttgttgggtcctggatttttgcctcattctcactttgcccctt

1. FPR3_SKO_328 -----
2. FPR3_C57BL6 ttctctctctgactacagttagatgctagagggatgtgcactgtagattgagcctt

1. FPR3_SKO_328 -----
2. FPR3_C57BL6 gtatcctggggcaactctgttgaggaaaggttgaacacagctatcacggttgaacaact

1. FPR3_SKO_328 -----
2. FPR3_C57BL6 agagggatcatcaggttcattgttagcttcagcttgccatgtccttgttgccatctgc

1. FPR3_SKO_328 -----
2. FPR3_C57BL6 tatggactcatcactacaaagattcacaanaagcctttgttaattccagccgtcctttc

1. FPR3_SKO_328 -----actagtg
2. FPR3_C57BL6 cgagttcttacagagattgtggtctcctctttatctgttggtttccctttccaattgggtg
* * ***

1. FPR3_SKO_328 gcccttttaggcacagctctggctcaagagatgcagtttagtggttagttataaaattatt
2. FPR3_C57BL6 gcccttttaggcacagctctggctcaagagatgcagtttagtggttagttataaaattatt
*****

1. FPR3_SKO_328 ggcaggttggttaatccaaccagttcattggcctttttcaatagctgcctcaatccaatt
2. FPR3_C57BL6 ggcaggttggttaatccaaccagttcattggcctttttcaatagctgcctcaatccaatt
*****

1. FPR3_SKO_328 ctctatgttttcatggccaggactttcaagaagactgattcattccctgtcttctcgt
2. FPR3_C57BL6 ctctatgttttcatggccaggactttcaagaagactgattcattccctgtcttctcgt
*****

1. FPR3_SKO_328 ctgcagagagccctgagtgaggactctggtcatatcagtgatacaagaaccaatttggct
2. FPR3_C57BL6 ctgcagagagccctgagtgaggactctggtcatatcagtgatacaagaaccaatttggct
*****

1. FPR3_SKO_328 tcaacttctgaagacattgaaataaaggcaatatga
2. FPR3_C57BL6 tcaacttctgaagacattgaaataaaggcaatatga
*****

```

**Figure 1.5: Fpr3<sup>-/-</sup> sequencing alignment for Fpr3<sup>-/-</sup> mouse line derived from founder 328.** Alignment of the Fpr3 coding sequence between the C57Bl/6 reference genome and the consensus sequence from forward and reverse DNA sequencing reactions of the Fpr3 gene region in the Fpr3<sup>-/-</sup> mouse line derived from founder mouse 328. The C57Bl/6 sequence spans positions 18,190,720 – 18,191,939 in the whole genome reference sequence deposited on ensembl.org. Alignments were generated using MAFFT. Asterisks represent positions of identity.

```

1. FPR123_TKO_3 tgagacatgagggcttattatTTTTTgtaattagtttaaagcaggaatagtttaagaa
2. FPR2_C57B16 tgagacatgagggcttattatTTTTTgtaattagtttaaagcaggaatagtttaagaa
*****

1. FPR123_TKO_3 tatgagaaatgtggagagctatgctaccccagaaaggtatgcagtaaagtgcagttttg
2. FPR2_C57B16 tatgagaaatgtggagagctatgctaccccagaaaggtatgcagtaaagtgcagttttg
*****

1. FPR123_TKO_3 aaatgttactgtgaaaatgctc-----
2. FPR2_C57B16 aaatgttactgtgaaaatgctcctcctgtagtagcaggtggtatacattcctaaatgagtgt
*****

1. FPR123_TKO_3 -----
2. FPR2_C57B16 catgtcagaaggagccaaatatctgagaaatggttgttttgaaaactttcaggtgcaga

1. FPR123_TKO_3 -----
2. FPR2_C57B16 caaaaatgaatccaactactccatccatctgaatggatcagaagtgggttatgattc

1. FPR123_TKO_3 -----tcctctcaatgggtggtgtctccatcactttcttctcct
2. FPR2_C57B16 taccatctccagagttctgtggatcctctcaatgggtggtgtctccatcactttctcct
*****

1. FPR123_TKO_3 tgggtgctgggcaatggactagtgatttgggtagctggattccggatgccacacactgt
2. FPR2_C57B16 tgggtgctgggcaatggactagtgatttgggtagctggattccggatgccacacactgt
*****

1. FPR123_TKO_3 caccactatctggatctgaaatctagcattggctgacttttctttcacagcaactctacc
2. FPR2_C57B16 caccactatctggatctgaaatctagcattggctgacttttctttcacagcaactctacc
*****

1. FPR123_TKO_3 attccttctgttgaatggctatgaaagaaaaatggccttttgctgggtcctgtgtaa
2. FPR2_C57B16 attccttctgttgaatggctatgaaagaaaaatggccttttgctgggtcctgtgtaa
*****

1. FPR123_TKO_3 attagttcacattgtggtagatgtaaaccctgttggaaagtgtcttcttgattgctctcat
2. FPR2_C57B16 attagttcacattgtggtagatgtaaaccctgttggaaagtgtcttcttgattgctctcat
*****

1. FPR123_TKO_3 tgccttggaccgctgcatttgttctgcatccagtctgggctcagaaccaccgcactgt
2. FPR2_C57B16 tgccttggaccgctgcatttgttctgcatccagtctgggctcagaaccaccgcactgt
*****

1. FPR123_TKO_3 gagcctggctaggaaggtggttgttggccctggatttttgcctctgattctcactttgccc
2. FPR2_C57B16 gagcctggctaggaaggtggttgttggccctggatttttgcctctgattctcactttgccc
*****

1. FPR123_TKO_3 cttttttatttcttgactactggttagaattcctggaggagatgtgattgtacattcaa
2. FPR2_C57B16 cttttttatttcttgactactggttagaattcctggaggagatgtgattgtacattcaa
*****

1. FPR123_TKO_3 ctttggatcctgggctcaaaactgatgaagaaaagtgaacacagctatcacttttgaac
2. FPR2_C57B16 ctttggatcctgggctcaaaactgatgaagaaaagtgaacacagctatcacttttgaac
*****

1. FPR123_TKO_3 aactagagggatcatcaggttccttattggtttcagcatgccatgtcaattgttgctgt
2. FPR2_C57B16 aactagagggatcatcaggttccttattggtttcagcatgccatgtcaattgttgctgt
*****

1. FPR123_TKO_3 ttgctatggactcattgctgtcaagatcaacagaagaaccttgttaattccagccgtcc
2. FPR2_C57B16 ttgctatggactcattgctgtcaagatcaacagaagaaccttgttaattccagccgtcc
*****

1. FPR123_TKO_3 tttacgagtccttacagcagttgtggcttccttctttatctgctgggttccctttcagct
2. FPR2_C57B16 tttacgagtccttacagcagttgtggcttccttctttatctgctgggttccctttcagct
*****

```

**Figure 1.6: Fpr2<sup>-/-</sup> sequencing alignment for Fpr1/2/3<sup>-/-</sup> mouse line derived from founder 327.** Alignment of the Fpr2 gene region between the C57Bl/6 reference genome and the consensus sequence from forward and reverse DNA sequencing reactions of the Fpr2 gene region in the Fpr1/2/3<sup>-/-</sup> mouse line derived from founder mouse 327. The C57Bl/6 sequence spans positions 18,112,762 – 18,113,781 in the whole genome reference sequence deposited on ensembl.org. The translation start codon is noted in bold. Alignments were generated using MAFFT. Asterisks represent positions of identity.

```

1. FPR123_TKO_3 atggaatccaactactccatccatctgaatggatcagaagtgggtggtttatgattctacc
2. FPR3_C57BL6 atggaaccaactactctatcccttgaatggatcagatgtgggatctatgattctacc
*****

1. FPR123_TKO_3 atctccagagttctgtggatcctctcaatgggtggtgtctccatcactttctccttggt
2. FPR3_C57BL6 atctccagggttctgtggatcctctcaatgggtggtgtctccatcactttctccttggt
*****

1. FPR123_TKO_3 gtgctgggcaatggactagtgatttgggtagctggattccggatgccacacactgtcacc
2. FPR3_C57BL6 gtgctgggaaatggactagtgatctgggtagctggattccggatgccacacactgtcacc
*****

1. FPR123_TKO_3 actatctgggatctgaatctagcat-----
2. FPR3_C57BL6 actatctgggatctgaatctagcattggctgacttctctttcacagcaactctaccattc
*****

1. FPR123_TKO_3 -----
2. FPR3_C57BL6 cttctgttgaaatggctatgaaagaaaaatggccttttggctggttcctgtgtaaatta

1. FPR123_TKO_3 -----
2. FPR3_C57BL6 gttcacattgcagtagatgtaaacctatttggaaagtgtctcttgattgctgtcattgac

1. FPR123_TKO_3 -----
2. FPR3_C57BL6 ttggaccgctgtatttgtgctctgcacccagttctgggctcagaaccaccgactgtgagc

1. FPR123_TKO_3 -----
2. FPR3_C57BL6 ctggctagaaaatgtggtggtggctcctggatttttgcctctcattctcactttgcccctt

1. FPR123_TKO_3 -----
2. FPR3_C57BL6 ttctctctcttgactacagttagagatgctagaggggatgtgcactgtagattgagcttt

1. FPR123_TKO_3 -----
2. FPR3_C57BL6 gtatcctggggcaactctgttgaggaaaggtgaaacacagctatcacgtttgtaacaact

1. FPR123_TKO_3 -----
2. FPR3_C57BL6 agagggatcatcaggttcatgttagcttcagcttgccatgtcctttgttgcacatctgc

1. FPR123_TKO_3 -----
2. FPR3_C57BL6 tatggactcatcactacaaagattcacaaaaagcctttgttaattccagccgtcctttc

1. FPR123_TKO_3 -----tg
2. FPR3_C57BL6 cgagttcttacaggagttgtggctcctctctttatctgtggttccctttcaattgggtg
**

1. FPR123_TKO_3 gcccttttaggcacagttctggctcaaagagatgcagtttagtggtagtataaaattatt
2. FPR3_C57BL6 gcccttttaggcacagttctggctcaaagagatgcagtttagtggtagtataaaattatt
*****

1. FPR123_TKO_3 ggcaggttggttaatccaaccagttcattggcctttttcaatagctgcctcaatccaatt
2. FPR3_C57BL6 ggcaggttggttaatccaaccagttcattggcctttttcaatagctgcctcaatccaatt
*****

1. FPR123_TKO_3 ctctatgttttcatgggcccaggactttcaagaaagactgattcattccctgtcttctcgt
2. FPR3_C57BL6 ctctatgttttcatgggcccaggactttcaagaaagactgattcattccctgtcttctcgt
*****

1. FPR123_TKO_3 ctgcagagagccctgagtgaggactctggctcatatcagtgatacaagaaccaatttggt
2. FPR3_C57BL6 ctgcagagagccctgagtgaggactctggctcatatcagtgatacaagaaccaatttggt
*****

1. FPR123_TKO_3 tcacttctgaagacattgaaataaaggcaatatga
2. FPR3_C57BL6 tcacttctgaagacattgaaataaaggcaatatga
*****

```

**Figure 1.7: Fpr3<sup>-/-</sup> sequencing alignment for Fpr1/2/3<sup>-/-</sup> mouse line derived from founder 327.** Alignment of the Fpr3 coding sequence between the C57Bl/6 reference genome and the consensus sequence from forward and reverse DNA sequencing reactions of the Fpr3 gene region in the Fpr1/2/3<sup>-/-</sup> mouse line derived from founder mouse 327. The C57Bl/6 sequence spans positions 18,190,720 – 18,191,939 in the whole genome reference sequence deposited on ensembl.org. Alignments were generated using MAFFT. Asterisks represent positions of identity.

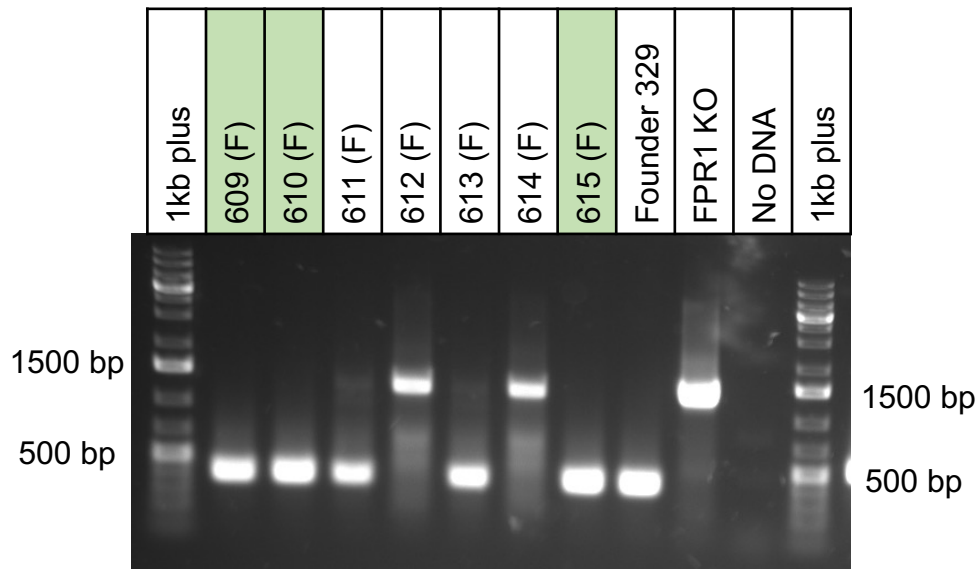


**Figure 1.8: PCR genotyping for the  $Fpr2^{-/-}$  mouse line derived from founder 329.** Detection of PCR product amplification length by agarose gel electrophoresis with primers that amplify the  $Fpr2$  gene (BS006/BS007). 1kb plus DNA ladder (Thermo Fisher) is used as a size marker. Two marker band lengths are annotated beside the 1kb plus DNA ladder on either side of the agarose gel image. Samples include DNA extracted and amplified from mice from the F2 generation derived from founder mouse 329 (samples 609 – 615), founder mouse 329, an  $Fpr1^{-/-}$  mouse, and a negative control PCR reaction containing no DNA. The  $Fpr1^{-/-}$  sample serves as a positive control for the full-length  $Fpr2$  PCR product. F2 mouse samples highlighted in green indicate homozygous  $Fpr2^{-/-}$  mice.

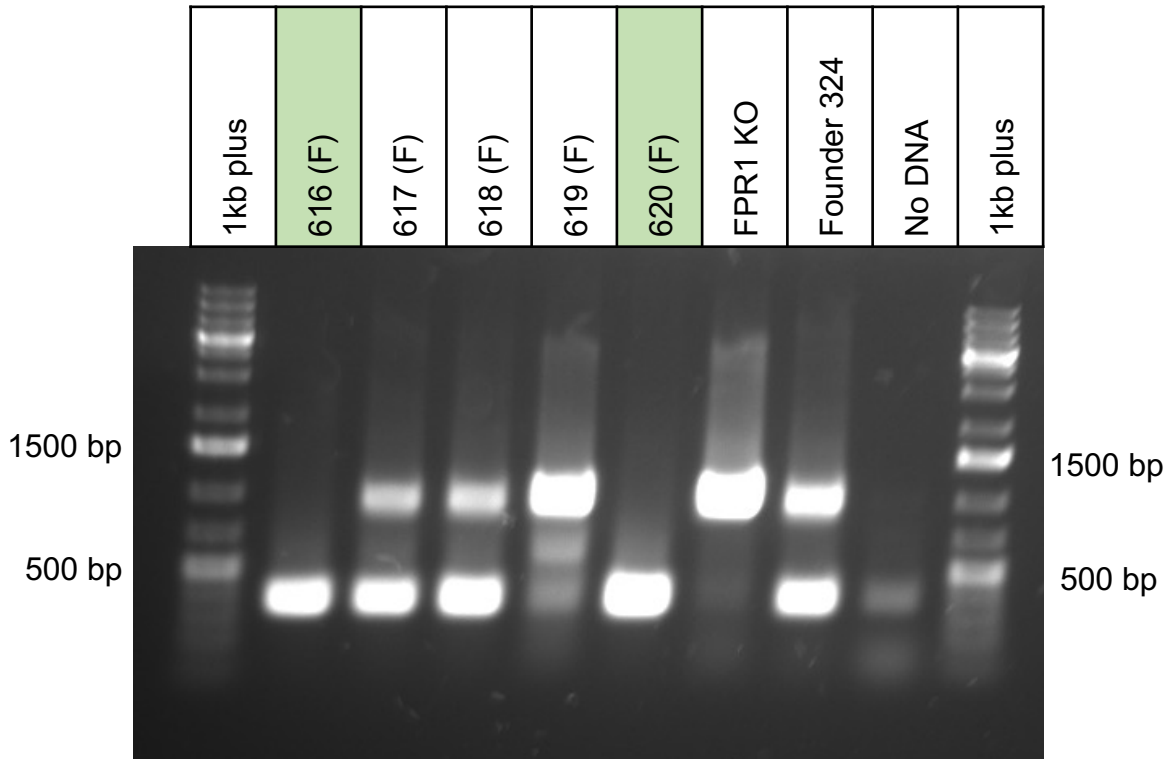


**Figure 1.9: PCR genotyping for the *Fpr1/3<sup>-/-</sup>* mouse line derived from founder 324.** Detection of PCR product amplification length by agarose gel electrophoresis with primers that amplify the *Fpr3* gene (BS011/BS013). 1kb plus DNA ladder (Thermo Fisher) is used as a size marker. Two marker band lengths are annotated beside the 1kb plus DNA ladder on either side of the agarose gel image. Samples include DNA extracted and amplified from mice from the F2 generation derived from founder mouse 324 (samples 616 – 620), an *Fpr1<sup>-/-</sup>* mouse, founder mouse 324, and a negative control PCR reaction containing no DNA. The *Fpr1<sup>-/-</sup>* sample serves as a positive control for the full-length *Fpr3* PCR product. F2 mouse samples highlighted in green indicate homozygous *Fpr1/3<sup>-/-</sup>* mice.

```

1. 3_1F      atgatgacgccagcatcgatatggaaccaactactctatccctttgaatggatcagatg
2. 3_1R      -----actactctatccc-ttgaatggatcagatg
3. Fpr3_C57B16 -----atggaaccaactactctatccctttgaatggatcagatg
                *****

1. 3_1F      tggtgatctatgattctaccatctccagggttctgtggatcctctcaatggtggtgtct
2. 3_1R      tggtgatctatgattctaccatctccagggttctgtggatcctctcaatggtggtgtct
3. Fpr3_C57B16 tggtgatctatgattctaccatctccagggttctgtggatcctctcaatggtggtgtct
                *****

1. 3_1F      ccatacactttctccttggngctgggaaatggactagtganctgggtagctggattcc
2. 3_1R      ccatacactttctccttggngctgggaaatggactagtganctgggtagctggattcc
3. Fpr3_C57B16 ccatacactttctccttggngctgggaaatggactagtganctgggtagctggattcc
                *****

1. 3_1F      ggatgccacacactgtcaccactatctggatctgaatctagcattggctgacttctctt
2. 3_1R      ggatgccacacactgtcaccactatctggatctgaatctagcattggctgacttctctt
3. Fpr3_C57B16 ggatgccacacactgtcaccactatctggatctgaatctagcattggctgacttctctt
                *****

1. 3_1F      tcacagcaactctaccattccttctgttgaatggctatgaaagaaaaatggccttttg
2. 3_1R      tcacagcaactctaccattccttctgttgaatggctatgaaagaaaaatggccttttg
3. Fpr3_C57B16 tcacagcaactctaccattccttctgttgaatggctatgaaagaaaaatggccttttg
                *****

1. 3_1F      gctgggtcctgtgtaaatagttcacattgcagtagatgtaaacctatttgaagtgtct
2. 3_1R      gctgggtcctgtgtaaatagttcacattgcagtagatgtaaacctatttgaagtgtct
3. Fpr3_C57B16 gctgggtcctgtgtaaatagttcacattgcagtagatgtaaacctatttgaagtgtct
                *****

1. 3_1F      tcttgattgctgtcattgccttggaccgctgtatttgtgctcctgcacccagtctgggctc
2. 3_1R      tcttgattgctgtcattgccttggaccgctgtatttgtgctcctgcacccagtctgggctc
3. Fpr3_C57B16 tcttgattgctgtcattgccttggaccgctgtatttgtgctcctgcacccagtctgggctc
                *****

1. 3_1F      agaaccaccgcaactgtgagcc-----tgggtgttgggtcctggatttttgctc
2. 3_1R      agaaccaccgcaactgtgagcc-----tgggtgttgggtcctggatttttgctc
3. Fpr3_C57B16 agaaccaccgcaactgtgagccctggctagaaatgtgggtgttgggtcctggatttttgctc
                *****

1. 3_1F      tcattctcactttgcccttttctccttcttctgactacagttagagatgctagaggggatg
2. 3_1R      tcattctcactttgcccttttctccttcttctgactacagttagagatgctagaggggatg
3. Fpr3_C57B16 tcattctcactttgcccttttctccttcttctgactacagttagagatgctagaggggatg
                *****

1. 3_1F      tgcactgtagattgagctttgtatcctggggcaactctgttgaggaaagggtgaacacag
2. 3_1R      tgcactgtagattgagctttgtatcctggggcaactctgttgaggaaagggtgaacacag
3. Fpr3_C57B16 tgcactgtagattgagctttgtatcctggggcaactctgttgaggaaagggtgaacacag
                *****

1. 3_1F      ctatcacgtttgtaaacactagaggatcatcaggttcattgtagcttcagcttgccca
2. 3_1R      ctatcacgtttgtaaacactagaggatcatcaggttcattgtagcttcagcttgccca
3. Fpr3_C57B16 ctatcacgtttgtaaacactagaggatcatcaggttcattgtagcttcagcttgccca
                *****

1. 3_1F      tgtcctttgttgccatctgctatggactcatcactacaaagattcacaaaaagcctttg
2. 3_1R      tgtcctttgttgccatctgctatggactcatcactacaaagattcacaaaaagcctttg
3. Fpr3_C57B16 tgtcctttgttgccatctgctatggactcatcactacaaagattcacaaaaagcctttg
                *****

1. 3_1F      ttaattccagccgctcctttccgagttcttacaggagttgtggcttctctttatctgtt
2. 3_1R      ttaattccagccgctcctttccgagttcttacaggagttgtggcttctctttatctgtt
3. Fpr3_C57B16 ttaattccagccgctcctttccgagttcttacaggagttgtggcttctctttatctgtt
                *****

```

**Figure 1.10: Sequencing alignment for the Fpr3 gene in Fpr1<sup>-/-</sup> mice.** Alignment of the Fpr3 coding sequence between the C57Bl/6 reference genome and the forward and reverse DNA sequencing reactions of the Fpr3 gene region in the Fpr1<sup>-/-</sup> mouse line generated by Dr. Philip Murphy's laboratory. The C57Bl/6 sequence spans positions 18,190,720 – 18,191,939 in the whole genome reference sequence deposited on ensembl.org. Alignments were generated using MAFFT. Asterisks represent positions of identity. Alignment continued on the next page.

```

1. 3_1F      ggtttcctttccaattgggtggcccttttaggcacagtctggctcaaagagatgcagttta
2. 3_1R      ggtttcctttccaattgggtggcccttttaggcacagtctggctcaaagagatgcagttta
3. Fpr3_C57B16 ggtttcctttccaattgggtggcccttttaggcacagtctggctcaaagagatgcagttta
*****

1. 3_1F      gtggtagttataaaaattattggcaggttggttaatccaaccagttcattggcctttttca
2. 3_1R      gtggtagttataaaaattattggcaggttggttaatccaaccagttcattggcctttttca
3. Fpr3_C57B16 gtggtagttataaaaattattggcaggttggttaatccaaccagttcattggcctttttca
*****

1. 3_1F      atagctgcctcaatccaattctctatgttttcatgggccaggactttca--gaagactga
2. 3_1R      atagctgcctcaatccaattctctatgttttcatgggccaggactttcaagaaagactga
3. Fpr3_C57B16 atagctgcctcaatccaattctctatgttttcatgggccaggactttcaagaaagactga
*****

1. 3_1F      ttcattccctgtcttctcgtctacagagag-cctgagtgaggactctggtcatatcagtg
2. 3_1R      ttcattccctgtcttctcgtctacagagagccctgagtgaggactctggtcatatcagtg
3. Fpr3_C57B16 ttcattccctgtcttctcgtctcagagagccctgagtgaggactctggtcatatcagtg
*****

1. 3_1F      atacaga-----
2. 3_1R      atacaagaaccaatttggcttcacttctcctgaagacattgaaataaaggcaataatc
3. Fpr3_C57B16 atacaagaaccaatttggcttcacttctcctgaagacattgaaataaaggcaatatga
****

```

**Figure 1.10 (Continued): Sequencing alignment for the Fpr3 gene in Fpr1<sup>-/-</sup> mice.** Alignment of the Fpr3 coding sequence between the C57Bl/6 reference genome and the forward and reverse DNA sequencing reactions of the Fpr3 gene region in the Fpr1<sup>-/-</sup> mouse line. The C57Bl/6 sequence spans positions 18,190,720 – 18,191,939 in the whole genome reference sequence deposited on ensembl.org. Alignments were generated using MAFFT. Asterisks represent positions of identity.

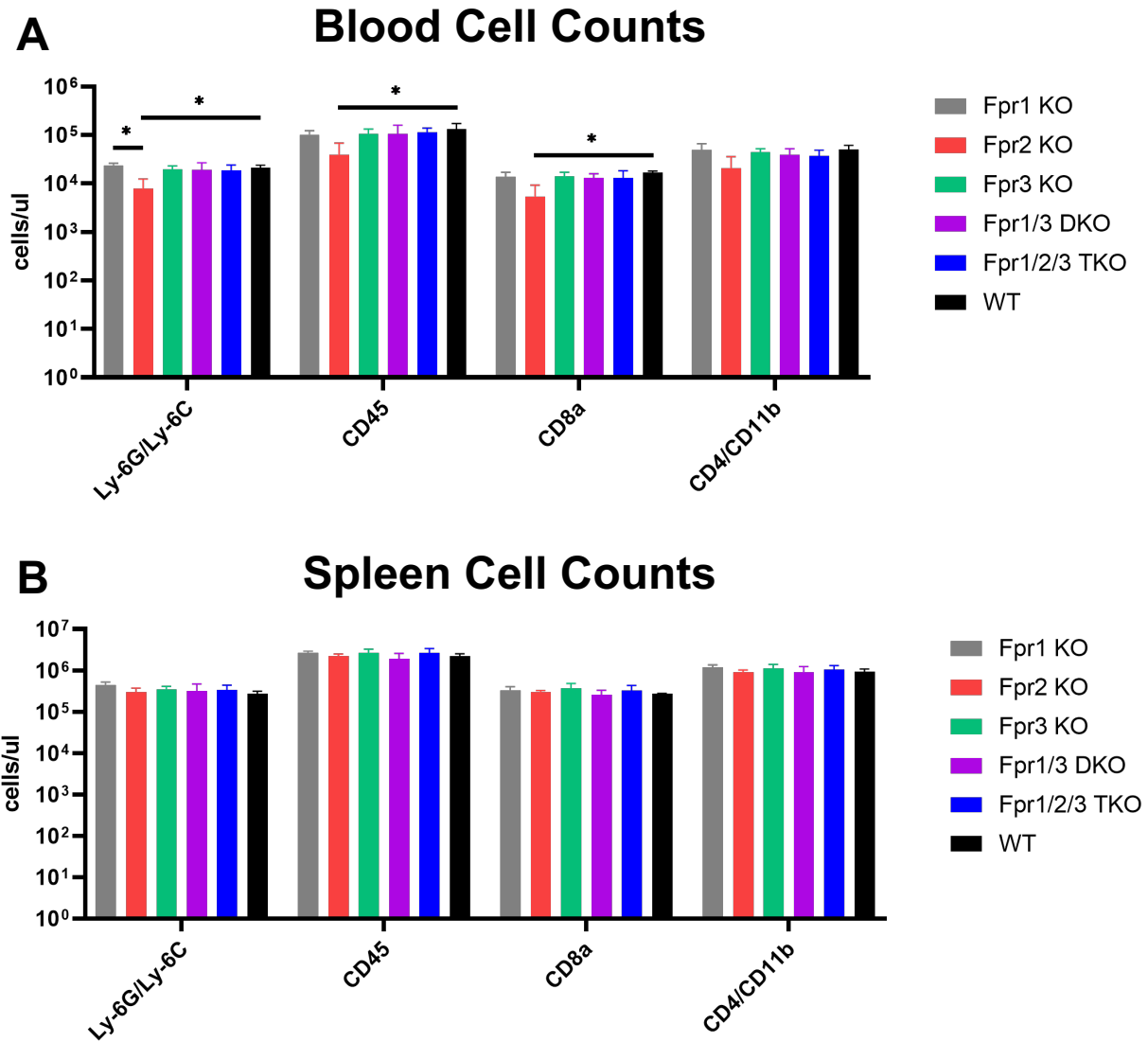


**Figure 1.11: Immune cell counts at homeostasis.** A,B: Age-matched mice from the indicated backgrounds were euthanized. Cardiac blood draws (A) or spleen dissections (B) were collected and analyzed by flow cytometry with antibodies targeting the indicated markers. Bars represent the mean  $\pm$  SD for 3 animals per group. Statistical significance was determined using the one-way ANOVA test with Tukey's multiple comparisons post-test using GraphPad Prism software. \*  $p < 0.05$

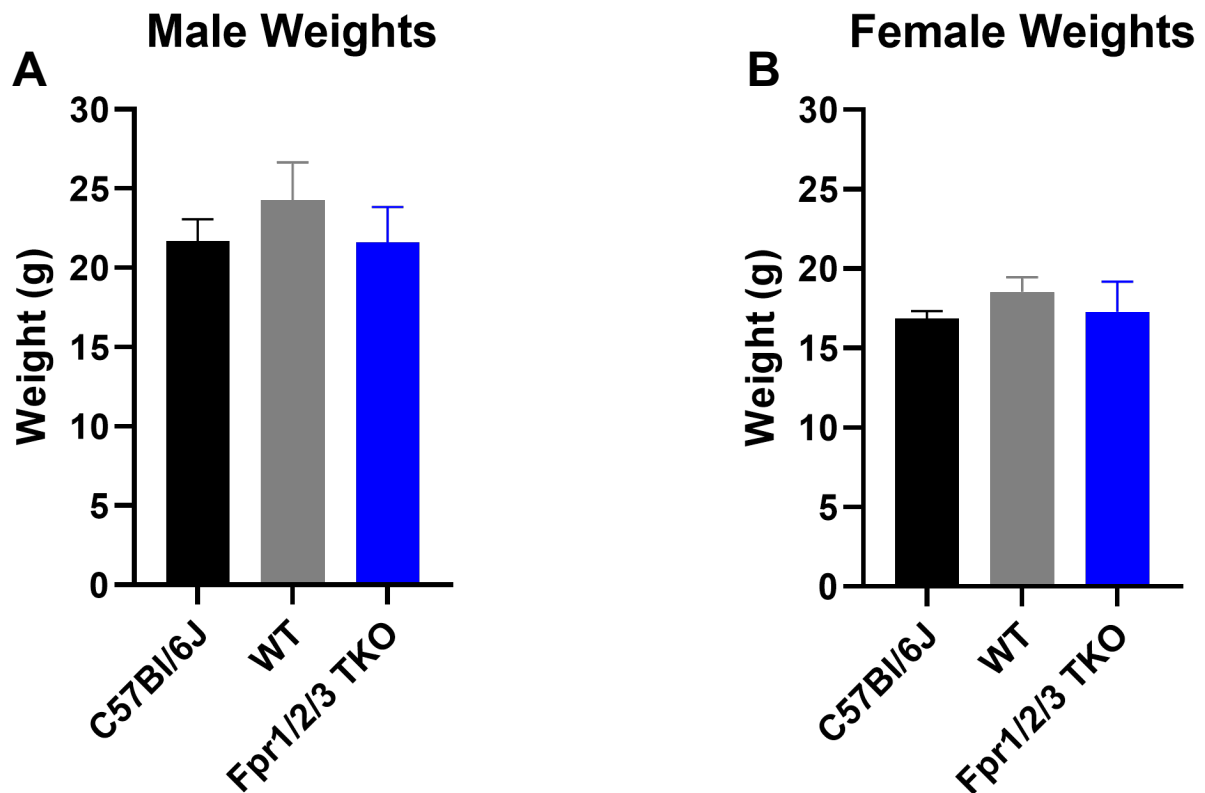


**Figure 1.12: Mouse weight comparison.** Weights of *Fpr1/2/3*<sup>-/-</sup>, isogenic WT, and purchased C57Bl/6J male (A) and female (B) mice. Bars represent the average  $\pm$  SD of at least 7 mice per group. Differences were assessed with one-way ANOVA and Tukey's multiple comparison post-test using GraphPad Prism software.

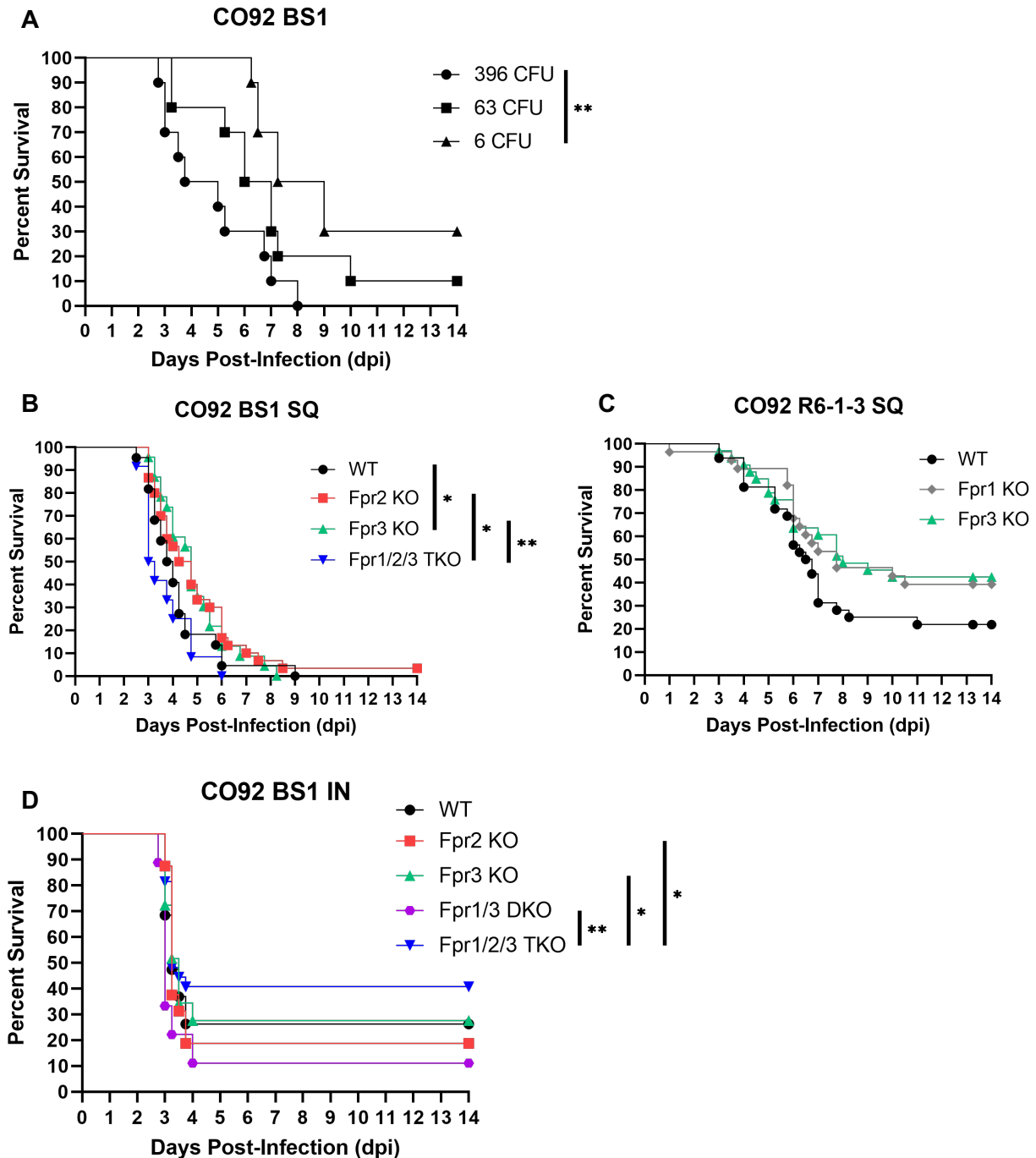


**Figure 2.1: Loss of FPRs alters survival kinetics during *Y. pestis* infection.** A. 10 mice per group were infected subcutaneously in the right inguinal fold with the indicated inocula of *Y. pestis* CO92 BS1, B. Mice were infected subcutaneously in the right inguinal fold with 400-600 CFU *Y. pestis* CO92 BS1 and monitored for 14 days, C. Mice were infected subcutaneously in the right inguinal fold with 400-600 CFU *Y. pestis* CO92 R6-1-3 and monitored for 14 days, D. Mice were infected intranasally with 1000 CFU *Y. pestis* CO92 BS1. Survival statistics were calculated using the Gehan-Breslow-Wilcoxon test with GraphPad Prism software. \*  $p < 0.05$  \*\*  $p < 0.005$

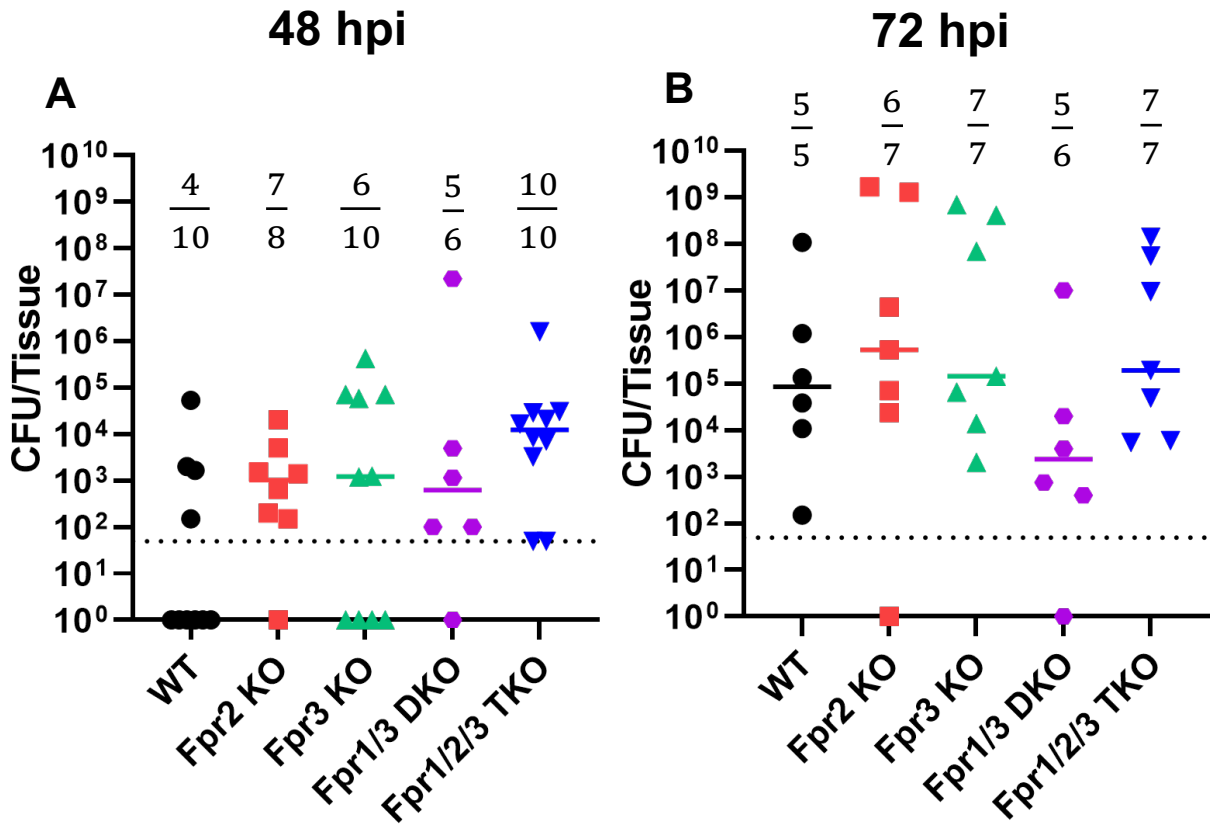


**Figure 2.2: Loss of FPRs alters bubonic plague dissemination rate.** A,B. Mice were euthanized 48 hpi (A) or 72 hpi (B) following subcutaneous infection with 400-600 CFU *Y. pestis* CO92 stock BS1. Spleens were dissected, homogenized, and plated on HIA containing Congo Red and galactose for CFU enumeration. Dotted line represents the limit of detection. Fractions indicate the number of mice with detectable CFU per the total number of mice per group. Differences between groups were assessed with one-way ANOVA and Tukey's multiple comparison post-test using GraphPad Prism software.

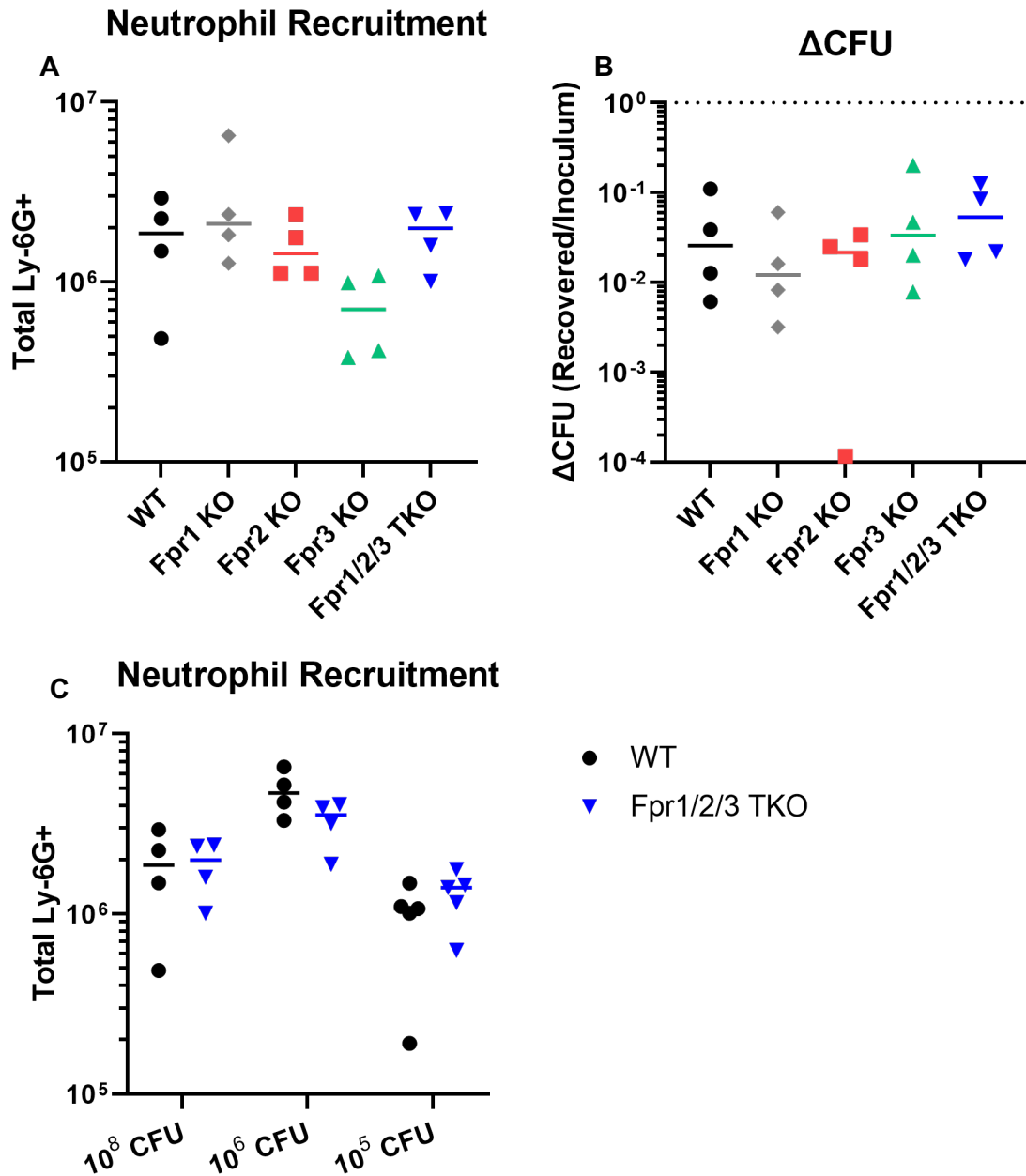


**Figure 2.3: FPR KO mice retain robust neutrophil migratory capabilities *in vivo*.** A,B. Mice were infected IP with  $10^8$  CFU *Y. pestis* KIM D27. After 3h, mice were euthanized and their IP cavities were lavaged. Ly-6G<sup>+</sup> cells were enumerated by flow cytometry (A) or surviving bacteria were detected by growth on agar plates (B). The  $\Delta$ CFU ratio is calculated by dividing the number of recovered CFU by the initial inoculum. The dotted line represent a ratio of 1:1 (i.e. no change in CFU). Ly-6G<sup>+</sup> cell recruitment in response to lower inocula ( $10^6$  and  $10^5$ ) was also tested (C). Bars represent the mean value. Differences between groups were assessed with one-way ANOVA and Tukey's multiple comparison post-test using GraphPad Prism software.

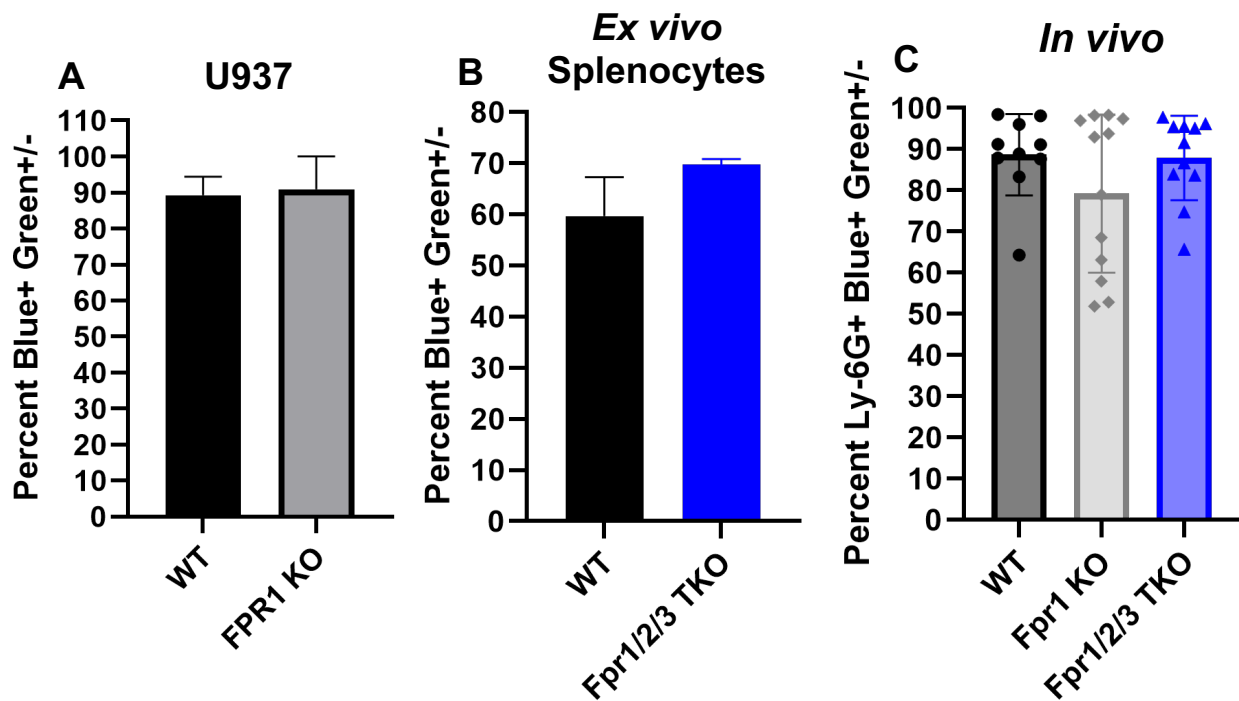


**Figure 2.4: *In vitro*, *ex vivo*, and *in vivo* T3SS injection of host cells.** A. WT and FPR1<sup>-/-</sup> U937 cells were infected with the T3SS reporter strain *Y. pestis* KIM D27 pMM83, and T3SS effector translocation was quantified by flow cytometry. B. Splenocytes were isolated from isogenic WT and Fpr1/2/3<sup>-/-</sup> mice and infected with *Y. pestis* KIM D27 pMM83. C. Isogenic WT, Fpr1<sup>-/-</sup>, and Fpr1/2/3<sup>-/-</sup> mice were infected IP with *Y. pestis* KIM D27 pMM83. IP lavage samples were collected and stained with CCF2-AM and anti-Ly-6G antibody. Injection was quantified in all experiments as the percentage of CCF2-AM-stained cells emitting blue fluorescence per the total number of stained cells. Bars represent the average of technical triplicate samples +/- SD (A,B,C) and points represent individual samples from infected mice (C). Differences between groups were assessed with student's t-test (A,B) or one-way ANOVA and Tukey's multiple comparison post-test (C) using GraphPad Prism software.

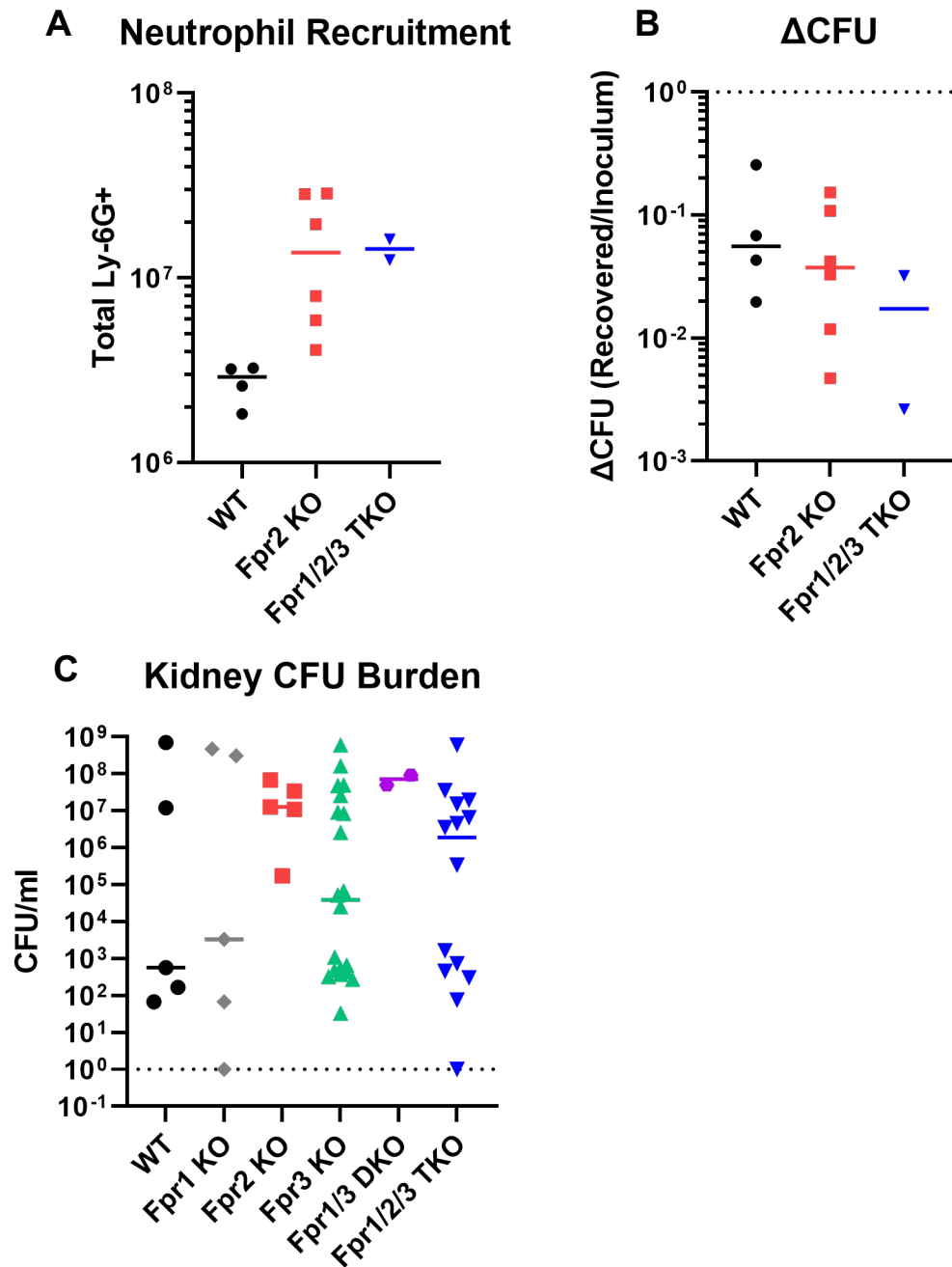


**Figure 2.5: FPRs respond to *S. aureus* but do not impact organ infiltration.** A,B. Mice were infected IP with 10<sup>8</sup> CFU *S. aureus* USA300. After 3h, mice were euthanized and their IP cavities were lavaged. Ly-6G<sup>+</sup> cells were enumerated by flow cytometry (A) or surviving bacteria were detected by growth on agar plates (B). The ΔCFU ratio is calculated by dividing the number of recovered CFU by the initial inoculum. The dotted line represent a ratio of 1:1 (i.e. no change in CFU). C. Mice were infected with 5×10<sup>7</sup> CFU *S. aureus* USA300. 5 dpi, kidneys were dissected, homogenized, and plated for CFU enumeration. Bars represent the mean (A,B) or median (C) value. Differences between groups were assessed with one-way ANOVA and Tukey's multiple comparison post-test using GraphPad Prism software.

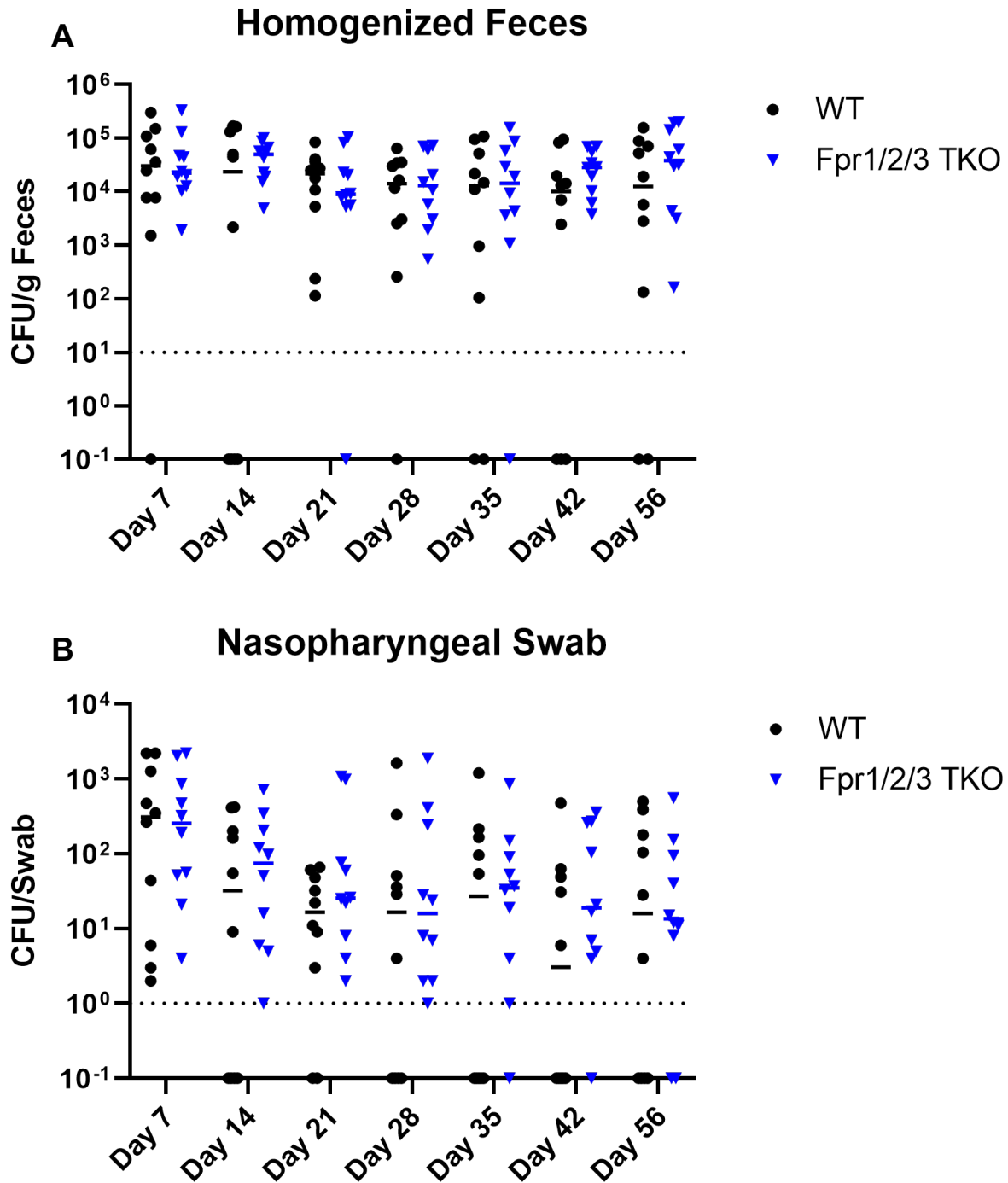


**Figure 2.6: *S. aureus* WU1 stably colonizes *Fpr1/2/3*<sup>-/-</sup> mice.** A,B: Mice were infected intranasally with 10<sup>8</sup> CFU *S. aureus* WU1. CFU were enumerated on a weekly basis from homogenized fecal samples (A) or nasopharyngeal swabs (B). Each point represents a single mouse. The dotted line represents the limit of detection. Bars represent the mean value. Differences between groups were assessed with two-way ANOVA using GraphPad Prism software.

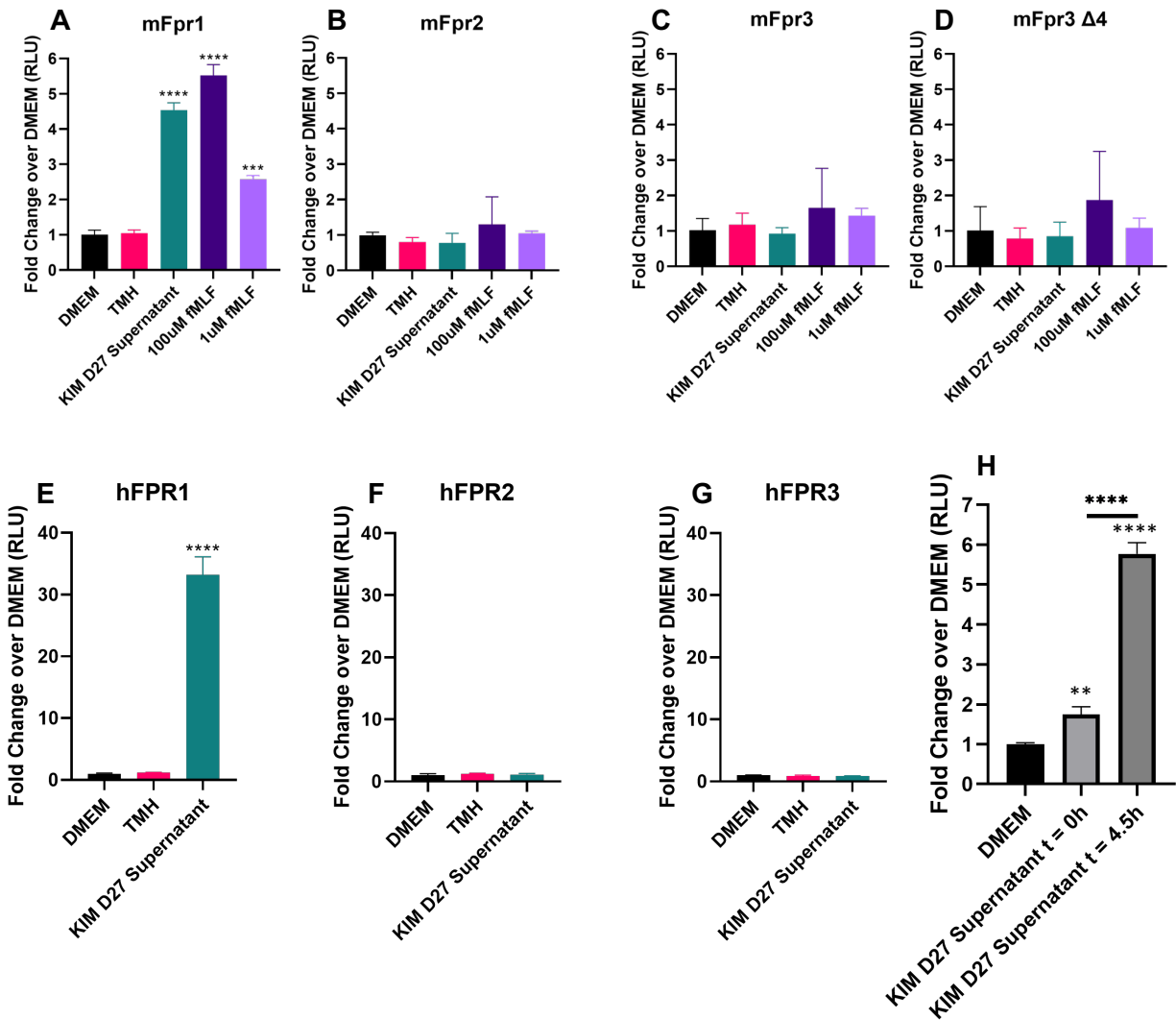


**Figure 3.1: *Y. pestis* supernatant activates Fpr1 in FPR reporter assays.** A, B, C, D, E, F, G. HTLA cells were transfected with mFpr1 (A), mFpr2 (B), mFpr3 (C), mFpr3 Δ4 (D), hFPR1 (E), hFPR2 (F) or hFPR3 (G) PRESTO-Tango plasmids. Activation after incubation with various stimuli was measured as a fold change in luminescence of stimulated cells in comparison to the average signal from medium control wells. H. Activation of mFpr1 with *Y. pestis* KIM D27 supernatant at t = 0h and t = 4.5h growth after culture refresh. Figures shown are representative of 3 independent experiments. Bars indicate the average from technical triplicates +/- SD. Statistical significance was determined using the one-way ANOVA test with Tukey's multiple comparisons post-test using GraphPad Prism software and is indicated in comparison to DMEM control samples (see floating asterisks) or between samples (see bars). \*\* p < 0.005 \*\*\* p < 0.0005, \*\*\*\* p < 0.00005

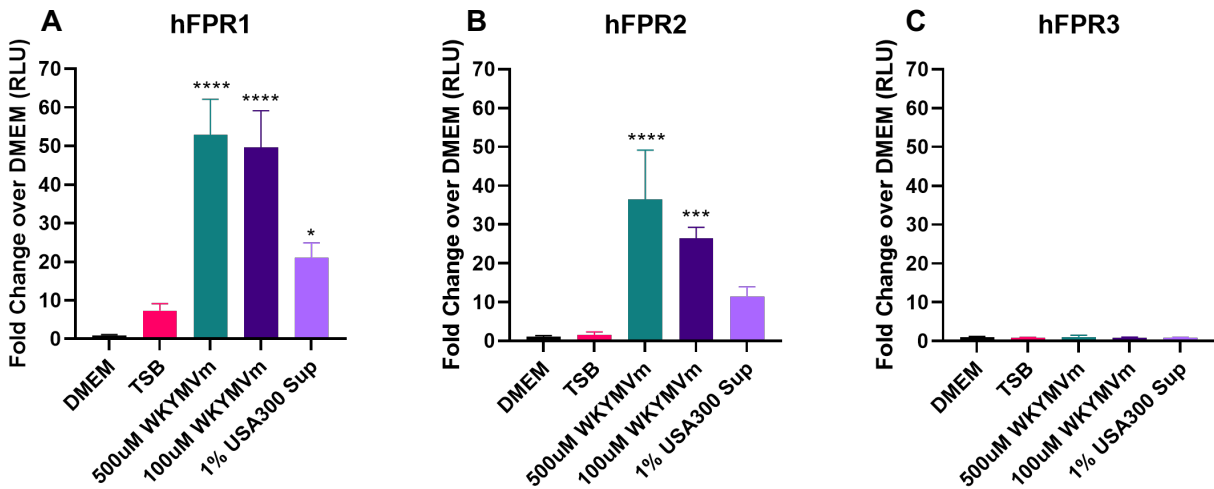


**Figure 3.2: *S. aureus* supernatant activates hFPR1 and hFPR2.** A, B, C. HTLA cells were transfected with hFPR1 (A), hFPR2 (B) or hFPR3 (C) PRESTO-Tango plasmids. Activation after incubation with various stimuli was measured as a fold change in luminescence of stimulated cells in comparison to the average signal from medium control wells. Figures shown are representative of 3 independent experiments. Bars indicate the average from technical triplicates +/- SD. Statistical significance was determined using the one-way ANOVA test with Tukey's multiple comparisons post-test using GraphPad Prism software and is indicated in comparison to DMEM control samples. \*\*\* p < 0.0005, \*\*\*\* p < 0.00005

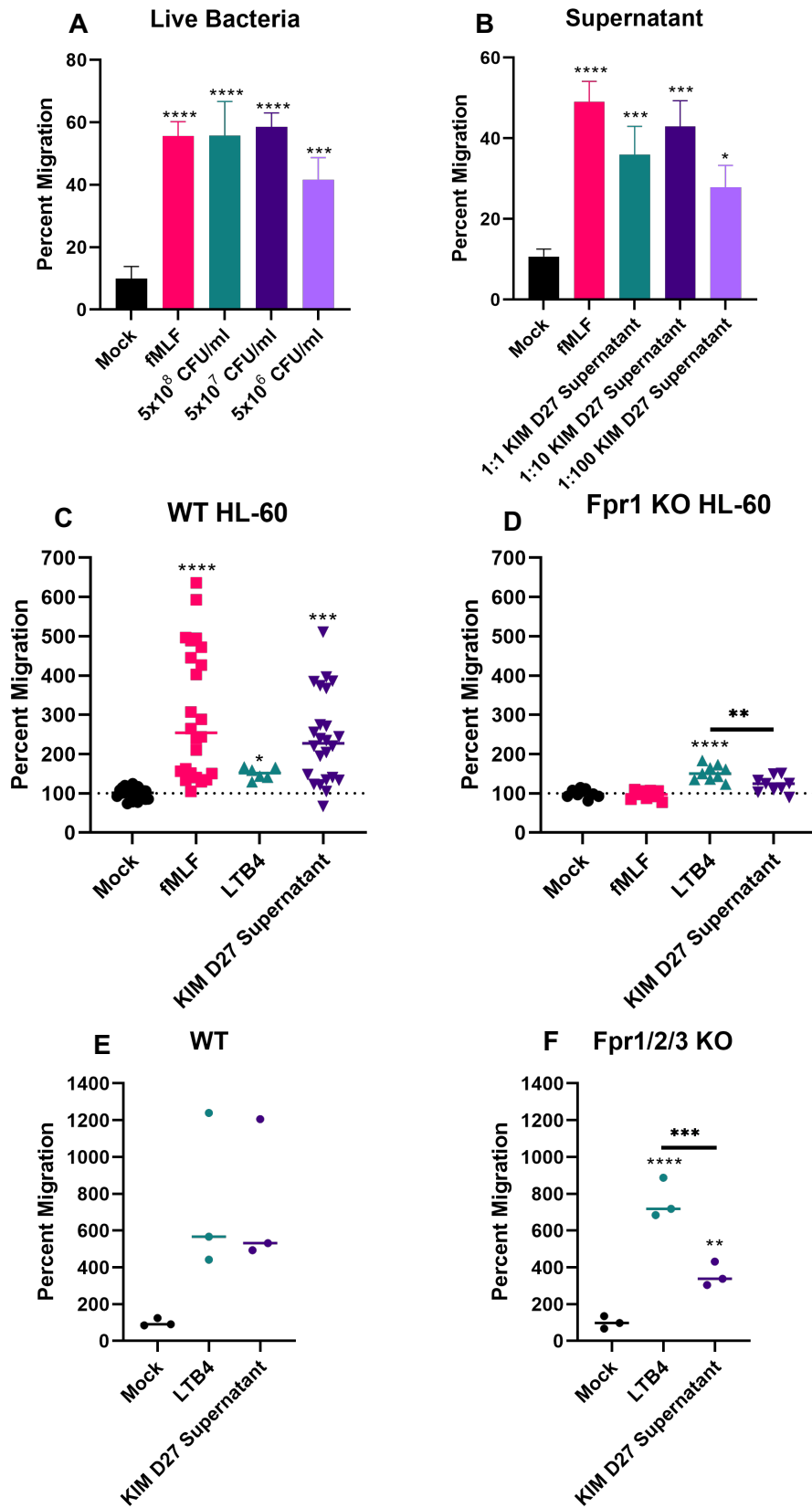
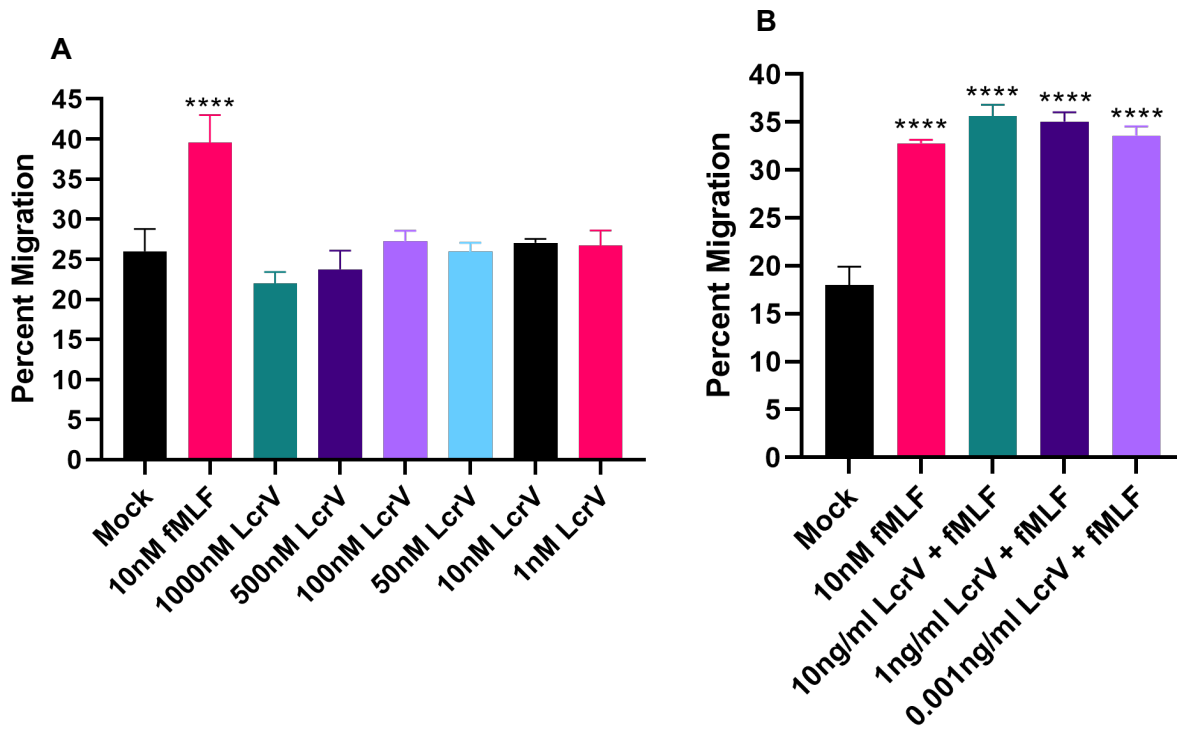
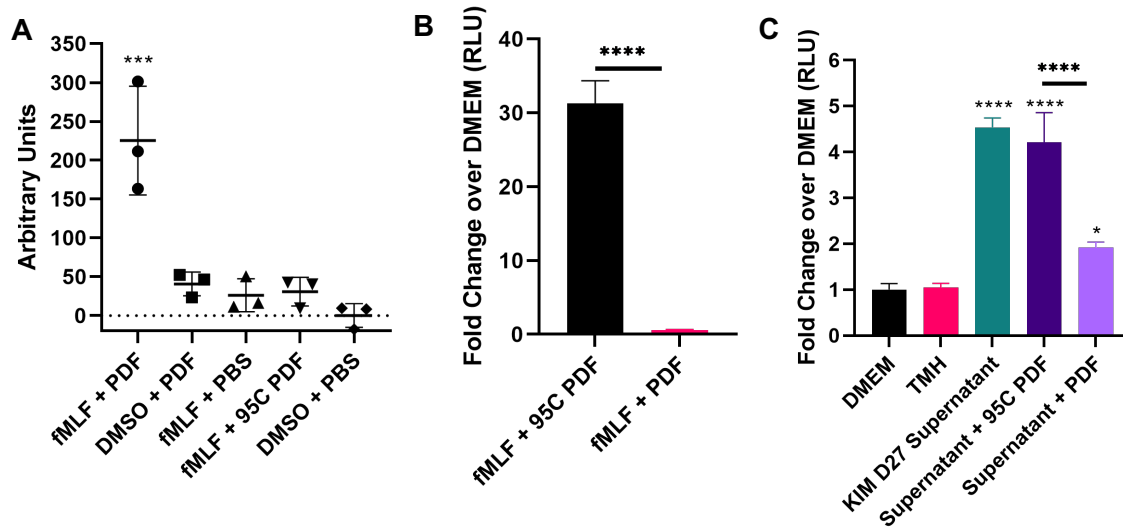


Figure 3.3: *Y. pestis* supernatant activates FPR1 in neutrophils.

**Figure 3.3 (Continued):** A,B. Dilution series of live *Y. pestis* KIM D27 (A) or cell-free supernatant (B) were used as stimuli for transwell chemotaxis assays with WT HL-60 cells. C,D. WT or FPR1 KO HL-60 cells were differentiated into neutrophil-like cells and tested for migration towards different stimuli using a transwell chemotaxis assay protocol. Figures show the combined results of at least 3 independent experiments per treatment tested. E,F. Thioglycollate-stimulated neutrophils were collected from WT (E) or *Fpr1/2/3<sup>-/-</sup>* mice (F) and quantified for migration activity to various stimuli using a transwell chemotaxis assay protocol. Figures are representative of two independent experiments. Bars (A,B) indicate the average from technical triplicates +/- SD. Points (C,D,E,F) are individual samples and bars (C,D,E,F) represent the median value. Statistical significance was determined using the one-way ANOVA test with Tukey's multiple comparisons post-test using GraphPad Prism software and is indicated in comparison to mock samples (see floating asterisks) or between samples (see bars). \*\*  $p < 0.005$  \*\*\*  $p < 0.0005$ , \*\*\*\*  $p < 0.00005$



**Figure 3.4: LcrV does not impact HL-60 chemotaxis.** A,B. Differentiated HL-60 cells were stimulated with different concentrations of LcrV alone (A) or LcrV in combination with fMLF (B). Bars indicate the average from technical triplicates +/- SD. Statistical significance was determined using the one-way ANOVA test with Tukey's multiple comparisons post-test using GraphPad Prism software and is indicated in comparison to mock samples. . \*\*\*\* p < 0.00005



**Figure 3.5: FPR1 agonists in *Y. pestis* supernatant are N-terminally formylated.**

A. Fluorescamine detection of primary amines in samples treated with PDF, heat-inactivated PDF (95C PDF), or DMSO/PBS controls. B. PRESTO-Tango detection of hFPR1 activation by fMLF pretreated with PDF or heat-inactivated PDF (95C PDF). C. PRESTO-Tango assay performed on HTLA cells transiently expressing mFpr1 and subjected to various stimuli. Bars represent the mean of technical triplicate samples +/- SD. Statistical significance was determined using the one-way ANOVA test with Tukey's multiple comparisons post-test using GraphPad Prism software and is indicated in comparison to mock samples (see floating asterisks) or between samples (see bars). Results are representative of at least 2 independent experiments. \*  $p < 0.05$ , \*\*\*  $p < 0.0005$ , \*\*\*\*  $p < 0.00005$

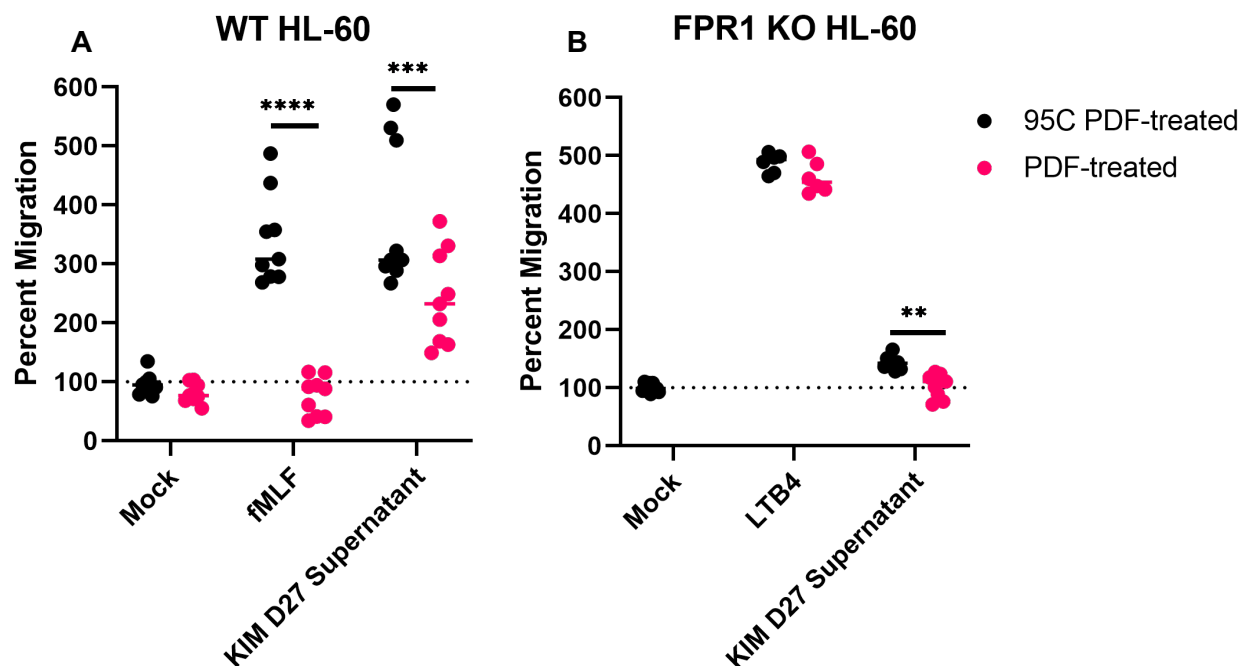


**Figure 3.6: Deformation of *Y. pestis* supernatant reduces neutrophil chemotaxis.** A, B. WT or FPR1 KO HL-60 cells were differentiated into neutrophil-like cells and tested for migration towards different stimuli using a transwell chemotaxis assay protocol. Stimuli were pretreated with catalytically-active PDF (PDF-treated) or heat-inactivated PDF (95C PDF-treated). Figures show the combined results of at least 3 independent experiments per treatment tested. Bars represent the median sample value. Statistical significance was determined using the one-way ANOVA test with Tukey's multiple comparisons post-test using GraphPad Prism software and is indicated in comparison to mock samples (see floating asterisks) or between samples (see bars). \*\*  $p < 0.005$  \*\*\*  $p < 0.0005$ , \*\*\*\*  $p < 0.00005$

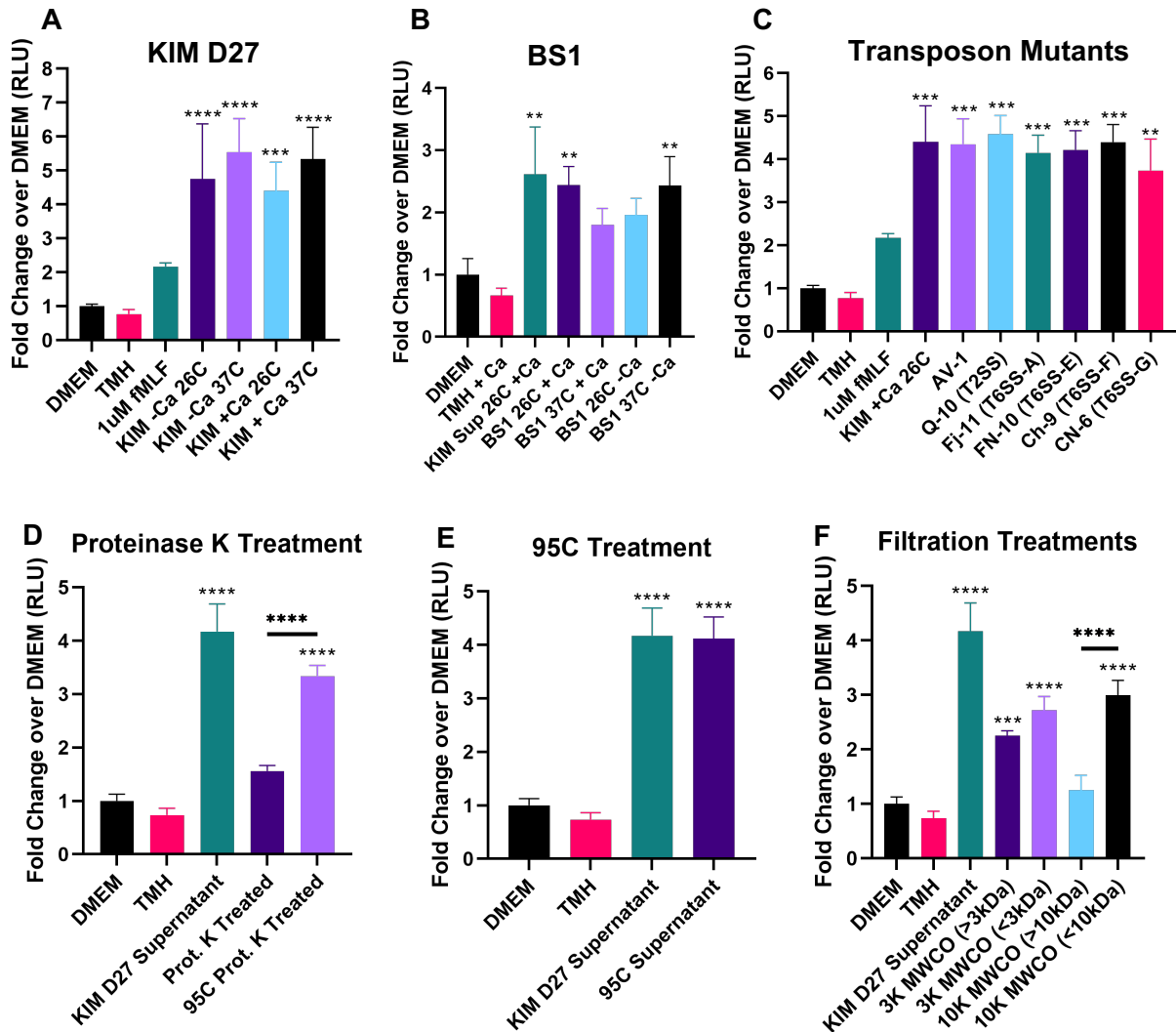


**Figure 3.7: Bacterial growth conditions and transposon insertions in specialized secretion systems do not impact secretion of the Fpr1 agonists in *Y. pestis* supernatant.** A, B, C, D, E, F. PRESTO-Tango detection of mFpr1 by various stimuli. A,B. *Y. pestis* supernatants from KIM D27 or CO92 BS1 strains prepared by growing KIM D27 in TMH +/- calcium (Ca) and either shifting the temperature to 37 °C (T3SS-inducing conditions) or continuing growth at 26 °C. C. *Y. pestis* supernatants derived from CO92  $\Delta$ pCD1 transposon mutants in the indicated specialized secretion systems. D,E,F. Supernatants from *Y. pestis* KIM D27 were subjected to Proteinase K treatment (D), heat treatment (E), or filtration through 3K or 10K MWCO filters (F). Bars represent the average sample value from technical triplicates +/- SD. Statistical significance was determined using the one-way ANOVA test with Tukey's multiple comparisons post-test using GraphPad Prism software and is indicated in comparison to mock samples (see floating asterisks) or between samples (see bars). \*\* p < 0.005 \*\*\* p < 0.0005, \*\*\*\* p < 0.00005

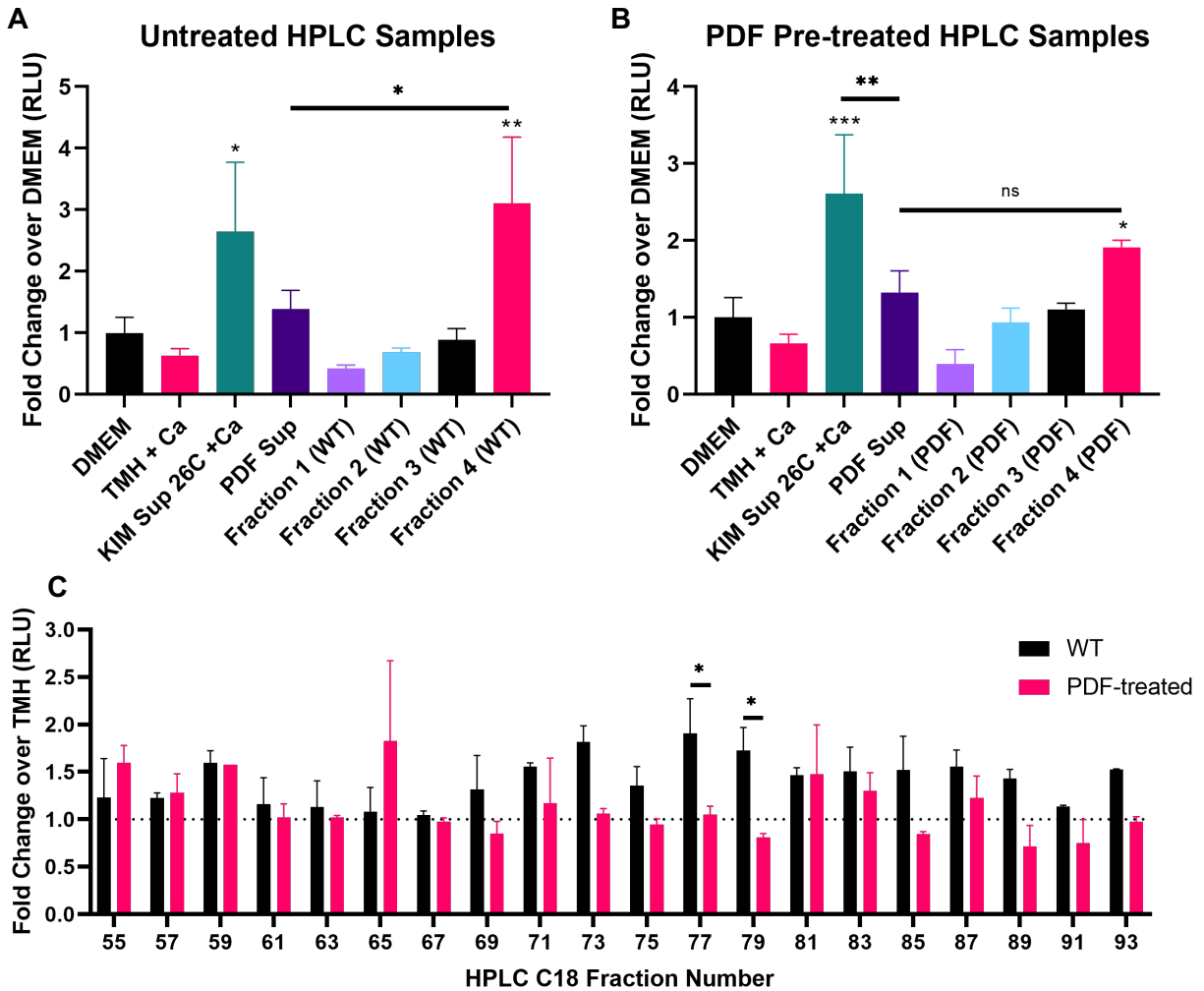


**Figure 3.8: Multiple HPLC C18 fractions have Fpr1 agonist activity.** A,B. *Y. pestis* KIM D27 supernatants either untreated (A) or treated with PDF (B) were subjected to C18 HPLC. Individual fractions were pooled into 4 large fractions and concentrated by SpeedVac prior to PRESTO-Tango quantification of mFpr1 activation. C. Individual fractions from WT or PDF-treated KIM D27 supernatants were analyzed for mFpr1 agonist activity by PRESTO-Tango. The dotted line represents the average value of mock samples. Bars represent the average sample value from technical triplicates +/- SD. Statistical significance was determined using the one-way ANOVA test with Tukey's multiple comparisons post-test (A,B) or two-way ANOVA (C) using GraphPad Prism software and is indicated in comparison to mock samples (see floating asterisks) or between samples (see bars). \* p < 0.05, \*\* p < 0.005, \*\*\* p < 0.0005, ns = not significant